

Università degli Studi di Milano  
Faculty of Physics  
Physics Department

Giuseppe Luca Celardo

FISICA, ASTROFISICA E FISICA APPLICATA, CICLO XVII

Ph.D. Dissertation

**LONG RANGE INTERACTING  
SYSTEMS:  
THE NON-ERGODICITY THRESHOLD**

Advisor: Prof. R. Bonifacio

Co-advisor: Prof. F. Borgonovi

Milano, 2004



## Abstract

A one dimensional Classical Heisenberg Model, with asymmetric coupling and two different inter-spin interactions, nearest neighbors and all-to-all, has been considered. Depending on the interaction range, dynamical properties, as ergodicity and chaoticity are strongly different. Indeed, even in presence of chaoticity, the model displays a lack of ergodicity only in the case of all-to-all interaction and below an energy threshold, that persists in the thermodynamical (infinite size) limit. This energy threshold, which we called the non-ergodicity threshold, can be found analytically and results can be generalized for a generic Classical Heisenberg Model with asymmetric coupling. Also the case in which the interaction potential decays as  $R^{-\alpha}$  is discussed. We prove that for  $\alpha > 1$  (short-range case) the non-ergodicity threshold does not exist. For  $\alpha < 1$ , except the infinite range case ( $\alpha = 0$ ), the question of the existence of the non-ergodicity threshold is still open. We conjectured that it exists for the long-range case.

The issue of the relevance of the non-ergodicity threshold with respect to phase transitions has also been addressed. Below the non-ergodicity threshold, the energy surface is disconnected in two components with positive and negative magnetizations respectively. Because the dynamics is continuous this implies that magnetization cannot change sign in time below the non-ergodicity threshold. Above the threshold, in a fully chaotic regime, magnetization changes sign in a stochastic way and its behavior can be fully characterized by an average magnetization reversal time. Statistical mechanics predicts a phase-transition at an energy higher than the ergodicity threshold. We assess the dynamical relevance of the latter for finite size systems through numerical simulations and analytical calculations. In particular, we derive an explicit expression of the time scale for magnetic reversal. As for standard phase transitions, this time-scale, as a function of the energy, diverges as a power at the non-ergodicity threshold. Moreover it increases exponentially with  $N$ . We also analyze the behavior of the system when the dynamics is not fully chaotic, for suitable values of the interaction strength. In this quasi-integrable regime reversal times are strongly dependent on the initial conditions.

The same system has also been studied from a quantum mechanical point of view. We address the problem of finding a quantum signature of the classical non-ergodicity threshold. Analysing the spectral properties of the system we define a quantum non-ergodicity threshold, in close correspondence with the classical one. We analyze the dynamical relevance of this threshold with respect to magnetic reversal times. We also show that, due to the existence of the non-ergodicity threshold, the interesting phenomena of Macroscopic Quantum Tunneling and Macroscopic Quantum Coherence can be found in the quantum case.



## Acknowledgement

I would like to thank my advisor Prof. Fausto Borgonovi, for his support, for his advices, and for his patience. He was always ready to listen to my (many) doubts, to answer my (many) questions, and guided me in the right direction with his insights. I'm also very grateful to him for the scientific freedom I could have in these exciting years of research with him.

I'm extremely grateful to Prof. Rodolfo Bonifacio, who supported my Ph.D. adventure and listened to my ideas during many train journeys.

I thank Prof. Felix Izrailev, who, from the early years of my thesis degree, has always been ready to give me his advises. He has been a guide in my scientific growth. A special thanks goes also to Prof. Stefano Ruffo, for his support and his advices. It has been a pleasure to work with him in these years.

I am indebted with many other people, with whom I discussed over the most different topics, I would like to remember Prof. G. Berman, Prof. Tomaž Prosen and Prof. Thomas H. Seligman. Surely I cannot forget Roberto Trasarti-Battistoni, he has been a very careful reader of the final manuscript. Moreover in these years, long discussions with him helped me to clarify my ideas. A special thanks goes also to Enrico Locatelli, who helped me with his numerical skill.

I also would like to thank all the people of the Department of Mathematics and Physics of The Catholic University of Brescia, where my Ph.D. adventure took place.

Finally I thank my Family for so many things that I cannot enumerate here. A special thanks goes also to all my friends.



# Contents

<b>1</b>	<b>Introduction</b>	<b>1</b>
1.1	Appendix A : Definition of Ergodicity . . . . .	6
<b>2</b>	<b>Broken Ergodicity</b>	<b>9</b>
2.1	Introduction . . . . .	9
2.2	The Model : chaoticity <i>vs</i> interaction range . . . . .	10
2.3	Ergodicity : numerical results . . . . .	12
2.4	Non-Ergodicity Threshold: analytical results . . . . .	15
2.4.1	Minimal energy . . . . .	15
2.4.2	Non-ergodicity threshold . . . . .	16
2.5	Generalization . . . . .	17
2.5.1	Generic Anisotropy . . . . .	17
2.5.2	$1/R^\alpha$ Interaction . . . . .	19
2.6	Conclusions . . . . .	20
<b>3</b>	<b>Time Scale for Chaotic Driven Magnetic Reversal</b>	<b>25</b>
3.1	Introduction . . . . .	25
3.2	The two Thresholds . . . . .	26
3.2.1	The non-ergodicity Threshold . . . . .	27
3.2.2	The statistical Threshold . . . . .	27
3.3	Time Scale for Magnetic Reversal . . . . .	30
3.4	Chaotic Driven Phase Transition . . . . .	34
3.5	Quasi-integrable Regime . . . . .	35
3.6	Conclusions . . . . .	38
3.7	Appendix A : Non-ergodicity threshold . . . . .	40
3.8	Appendix B : Minimum energy . . . . .	41
3.9	Appendix C : Critical exponents . . . . .	41
<b>4</b>	<b>Quantum Signatures of the Non-Ergodicity Threshold</b>	<b>45</b>
4.1	Introduction . . . . .	45
4.2	Quantum considerations: generals . . . . .	46
4.3	Quantum signature of classical broken ergodicity . . . . .	48
4.3.1	The Semiclassical Regime . . . . .	48
4.3.2	The Hard Quantum Regime . . . . .	51
4.4	High Order Perturbative Approach . . . . .	53
4.4.1	Comparison with Numerical Results . . . . .	57
4.5	Time Scale for Quantum Magnetic Reversal . . . . .	61
4.5.1	Macroscopic Quantum Tunneling . . . . .	61
4.5.2	Quantum Reversal Times: Above $\epsilon_{ne}$ . . . . .	64

4.5.3	Quantum Reversal Times: Below $\epsilon_{ne}$ . . . . .	64
4.5.4	Towards Macroscopic Quantum Coherence . . . . .	65
4.6	Conclusions . . . . .	68
4.7	Appendix A: Computing the Hamiltonian Matrix . . . . .	69
<b>5</b>	<b>The non-ergodicity threshold: Conclusions and Perspectives</b>	<b>73</b>
<b>6</b>	<b>Quantum Computation</b>	<b>79</b>
6.1	Introduction . . . . .	79
6.2	Dynamical fidelity of a solid-state quantum computation . . . . .	81
6.2.1	Introduction . . . . .	81
6.2.2	Spin model of a quantum computer . . . . .	82
6.2.3	Absence of quantum chaos in the selective excitation regime . . . . .	84
6.2.4	Fidelity of a quantum protocol . . . . .	85
6.2.5	Selective excitation regime and perturbation theory . . . . .	86
6.2.6	Quantum protocol . . . . .	88
6.2.7	Dynamical fidelity: theory and numerical data . . . . .	89
6.2.8	Fidelity: dependence on the number of qubits . . . . .	91
6.2.9	Optimal algorithm . . . . .	93
6.2.10	Conclusions . . . . .	95
6.3	Stability of the quantum Fourier transformation on the Ising quantum computer	95
6.3.1	Introduction . . . . .	95
6.3.2	The Ising quantum computer . . . . .	96
6.3.3	Linear Response theory . . . . .	98
6.3.4	Errors in the quantum Fourier transformation . . . . .	100
6.3.5	Intrinsic Errors . . . . .	100
6.3.6	External Errors . . . . .	104
6.3.7	Intrinsic and External Errors combined . . . . .	107
6.3.8	Conclusions . . . . .	108
6.3.9	Appendix A: QFT and IQFT implementation on the Ising Quantum Computer . . . . .	110
	<b>Appendices</b>	<b>115</b>

# Chapter 1

## Introduction

La sottise, l'erreur, le péché, la lésine,  
Occupent nos esprits et travaillent nos corps,  
Et nous alimentons nos aimables remords,  
Comme les mendiants nourrissent leur vermine.

—*Les Fleurs du Mal, Au Lecteur, Charles Baudelaire*

The aim of this introduction is to present the general point of view and some particular concepts that will be useful throughout the present dissertation. We will briefly explain the connection of long-range interacting systems with the ergodic problem. This will allow us to specify both the terminology and the scientific background in which our research can be located.

Ordinary examples in Statistical Mechanics involve systems of non-interacting particles in which equilibrium is assumed. Non-interacting systems are considered for the simple reason that they can be treated exactly, moreover in some physical situations (e.d. dilute gas) they are a good approximation. Interaction cannot be forgotten in all the cases, for instance phase transitions would be hard to be explained without interaction. Qualitatively we can say that during a phase transition the properties of the system change abruptly at a sharply defined critical parameter value. Such an abrupt change can be explained only through a cooperative behavior of all the particles that could not take place without interaction (1).

Many-body interacting systems are a fundamental model for physical phenomena. Such systems are very difficult to be treated analytically from the point of view of Statistical Mechanics. Thus simplified models (toy models) are usually considered. An example is the Ising Model, which, in two dimension, is the only non trivial example of a phase transition that can be worked out with mathematical rigor. On the other side often these simplified models have been successful in describing the main features of real systems, for instance the magnetization curve ( $M$  vs  $T$ ) computed from the Ising Model well reproduces the one of nickel (4). Because of the complexity of interacting systems it is also difficult to give an analytical treatment of their dynamical properties, thus the study of the latter is often based on numerical experiments. Indeed in most of the cases many-body interacting systems are not integrable and display chaotic motion, even if few particles are considered. The possibility to integrate numerically the equations of motion, allows to compare the equilibrium values predicted by Statistical Mechanics with the experimental results of numerical simulation of the dynamics of the system. This allow to address the problem of a dynamical foundation of the methods of Statistical Mechanics.

In Statistical Mechanics equilibrium values of observables are computed averaging over the accessible states, weighted by a given Probability distribution (2). For an isolated system, the equal a priori probability postulate implies a uniform Probability distribution over the phase space in a narrow energy interval (if the energy is the only known constant of motion). This methodology is poorly justified, and is essentially based on the agreement with empirical findings. The dream of a dynamical foundation of the methods of Statistical Mechanics has deep roots (3). Historically the argument was the following: Since the time needed for the measurement (observational time), of an observable, is never zero, then measured values can be regarded as time averages of a phase space function corresponding to the observable. Thus Boltzmann supposed that during its motion the system visits all the available states so that space averages will be equal to time averages; this explanation is unsatisfactory for different reasons, see Ref.(5), and it is better to regard the possibility to replace time-averages with space-averages as an hypothesis, namely the *Ergodic Hypothesis*, (from the greek words “ergos”, energy and “odos”, path). A more rigorous definition of ergodicity is given in Appendix (A). A fundamental contribution to the problem of proving the Ergodic Hypothesis came from Birkhoff (1931)(5; 1). He proved that if a dynamical system is metrically indecomposable (or metrically transitive) on a given subspace than it is ergodic on that subspace. A given subspace is said to be metrically indecomposable if it cannot be decomposed into two invariant subspaces of positive measure. Note that metrical transitivity is a sufficient and necessary condition for ergodicity. Much effort has been done to prove ergodicity but with only few successes, (6). Mostly, the ergodicity property is analyzed by numerical experiments.

We would like to stress here that, from the point of view of the Ergodic Hypothesis, in order to have a dynamical justification of the methods of Statistical Mechanics two conditions must be satisfied, which should remain distinct:

- (I) Ergodicity on an infinite time scale: Infinite time averages are equal to space averages, computed according to the prescription of Statistical Mechanics. In this case we can say that the system behaves ergodically on an infinite time scale.
- (II) Ergodicity on a finite time scale: Finite time averages must be a good approximation of infinite time averages (with finite time average we mean a time average over the observational time scale,  $\tau_{obs}$ ). In this case we can say that the system behaves ergodically also on a finite time scale.

Even if, from the Mathematical point of view, ergodicity is defined on an infinite time scale only, thus (I) is the only definition of ergodicity, from a physical point of view is important to distinguish the two cases: indeed if either (I) or (II) are not true we expect the the usual methods of Statistical Mechanics fails to give an exact description of equilibrium properties of the system.

Palmer in his seminal paper (7) focuses on the second point. He stresses that broken ergodicity is a usual phenomenon in physics because even if, on an infinite time interval, the system may be considered ergodic, on a finite time scale the system may be effectively confined in a subspace of the accessible phase space (component), thus (II) is not valid anymore. Palmer defines the components with two properties:

- 1) Confinement: the cumulative escape probability up to time  $\tau_{obs}$  is small.
- 2) Internal Ergodicity: time averages over the time interval  $\tau_{obs}$  are a good approximation of space averages inside the component. While the time scale to reach equilibrium on the whole energy surface is much longer. This means that there are two distinct time scales: the system quickly explores the component, but the time needed to explore the whole energy surface is much longer.

He also distinguishes two different cases:

- a) Frozenness: if the escape probability is zero, than the component is said to be frozen or absolutely confined.
- b) Metastability: For non-zero escape probability the component is said to be metastable.

This general point of view on the broken ergodicity problem in dynamical systems is very close to the one used in this dissertation.

In recent years the connection of the ergodic properties of a dynamical system with respect to the range of the interaction have been investigated (15). The dynamical and statistical properties of a system of interacting particles crucially depends on the long or short range nature of the interaction.

What do we mean with long range interacting systems?

Typical interaction potentials decrease with the distance, so that the slower they decrease, the longer is the range of the interaction.

If the range of the interaction is determined by a real parameter  $\alpha$  (for instance for a potential which decays as  $R^{-\alpha}$ ), usually system properties change in a sharp way in correspondence of a critical parameter value. In this case we are legitimate to consider the critical parameter value as the the value that divides between the short and the long range case.

In order to define the long and the short range of the interaction let us consider a uniform distribution of particles and an interaction potential  $V(\mathbf{x})$ . We can write the interaction energy of each particles with the other particles, whose distance is longer than  $\epsilon$ , as  $E \sim \int_{\epsilon}^{\infty} V(\mathbf{x})d\mathbf{x}$ . This energy represent the interaction energy of one particles with the distant ones. If this energy diverges the interaction is said to have a long range, otherwise a short range. If we consider a potential which decays as  $R^{-\alpha}$  we have:

$$E \sim \int_{\epsilon}^{R_1} \frac{R^{d-1}}{R^{\alpha}} dR = \frac{R_1^{d-\alpha}}{d-\alpha} - \frac{\epsilon^{d-\alpha}}{d-\alpha} \text{ for } \alpha \neq d$$

$$E \sim \ln\left(\frac{R_1}{\epsilon}\right) \text{ for } \alpha = d$$

where  $d$  is the immersion dimension of the system. As one can see if  $\alpha > d$  the interaction has a short range while if  $\alpha \leq d$  the interaction has a long range. With this definition, in three dimension, gravitation and coulomb forces are long range,  $V \sim R^{-1}$ . Also dipole interactions are long range since  $V \sim R^{-3}$ .

Note that this definition of long and short range is not universally accepted. For instance for critical phenomena, short range is associated with  $\alpha > d + 2 - \eta$ , where  $\eta$  is a small parameter system-dependent (10).

Statistical and dynamical properties can therefore be very different depending on the range of the interaction. An important property of long range interacting systems is non-additivity (18). A system is said to be non-additive if the total energy cannot be obtained from the sum of the energies of its macroscopic parts, spatially distinct. Suppose to divide the system into two halves of energy  $E_1$  and  $E_2$ . Non-additivity implies that  $E \neq E_1 + E_2$ . Now, because we can always write  $E = E_1 + E_2 + V$ , if the interaction energy,  $V$ , can be neglected (in the thermodynamic limit), the system is additive. The interaction energy can be usually neglected for short range interaction, indeed they usually give a surface contribution that is negligible with respect to volume contribution of the total energy. Non-additivity has important consequences from a Statistical point of view, for instance microcanonical and canonical prediction can differ if a system is non-additive(9). Indeed in the derivation of the canonical ensemble from the microcanonical one, additivity is assumed.

We will consider now in more detail how the ergodic properties of a system depend on the range of the interaction. For short range interacting systems chaos is usually assumed to give a sufficient condition for ergodicity. A typical situation for short-range nonlinear interacting systems, is that the maximal Lyapunov exponent remains finite in the thermodynamical limit, thus leading to an ergodic behavior. On the other side, long range interacting systems have been often found to violate ergodicity. Two ways in which this can occur are well known in literature:

- 1) Chaos Suppression(11): This phenomenon has been found in many long range systems. It can be described as follow: as the number of particles increases, at fixed interaction energy, the chaoticity of the system decreases, namely the maximal Lyapunov exponent decreases as  $N^{-k}$ , where  $k$  is of order 1. Thus, in the thermodynamical limit, the system becomes quasi-integrable. Note that for any finite number of particles the phenomenon of chaos suppression does not exclude the possibility of ergodicity on an infinite time scale.
- 2) Slow Relaxation of Metastable states(12): There are examples of metastable states whose relaxation time diverge as  $N \rightarrow \infty$ . In this case a metastable state becomes frozen ( or stable) in the thermodynamical limit, and ergodicity is definitively broken. As before the slow relaxation of metastable states does not exclude the possibility that the system is ergodic on an infinite time scale if a finite number of particles is taken into account.

Note that both the mentioned ways in which long range interaction effectively breaks ergodicity are more related to condition (II) than to condition (I), because they do not exclude the possibility that the system is actually ergodic on an infinite time scale. In the present dissertation we will address both this two aspects of long range broken ergodicity, nevertheless our main aim is to analyze a third way in which ergodicity is broken in long range interacting systems (17). We will prove the existence of frozen components for all  $N$  and their relation with the long range of the interaction. This third way is directly related to condition (I).

Specifically we have analyzed a Classical Heisenberg Model with an infinite range of the interaction. We have chosen an infinite interaction range because the analytical treatment is easier in this case, and exact results can be obtained. Indeed, for infinite range interacting systems, Mean-Field models, which usually can be treated analytically, constitutes a very good approximation. Throughout the dissertation the comparison with them will be fundamental to elucidate both the statistical and the dynamical properties under investigation. Moreover, there are several indications that behaviors found in the infinite range case extend to cases where two-body potentials decays at large distance with a power smaller than space dimensionality (13). We showed that if the interaction is anisotropic than an energy threshold exists, below which the phase space is disconnected into two frozen components. Since below this threshold the phase-space is disconnected (thus metrically decomposable), it cannot be ergodic on the whole energy surface. We thus called this threshold the *non ergodicity threshold*. It is interesting to note that such threshold exists for all  $N$  and is independent from the chaoticity of the system, having a topological and not a dynamical nature. The non-ergodicity-threshold exists only if the anisotropy induces an easy-axis of the magnetization, namely the minimal energy configuration is the one in which all the spins are aligned along one direction, which defines implicitly the easy-axis of the magnetization. In Chapter (2) we will compute analytically such threshold and, on the basis of our results, we will conjecture that it cannot exist for short range interaction ( we will prove this statement for the one-dimensional case and a potential decaying algebraically with the distance).

Each frozen components is defined by the sign of the total magnetization along the easy axis of the magnetization, namely the sign of the magnetization is positive in one component

and negative in the other. This makes the existence of frozen components interesting not only with respect to the problem of a dynamical foundation of the methods of Statistical Mechanics, indeed, in our case, the frozenness of these two components has interesting physical consequences: for instance the magnetization cannot change sign in time below the non-ergodicity threshold. We will analyze the consequences of this sharp breaking of ergodicity with respect to phase transitions and with respect to the time scale of magnetic reversal in Chapter (3). On the Quantum side we will handle with the same Model. The comparison between the classical and the quantum behavior is not an easy task, but in recent years many tools have been developed (14), which are very useful to interpret the dynamical properties of a system in terms of its spectral properties. Guided by this considerations, in Chapter (4), we will give evidence of the existence of a quantum signature of the classical non-ergodicity threshold. Indeed we will provide an independent definition of a quantum non-ergodicity threshold, motivated by considerations strictly valid in the quantum regime. We will then show the connection between the two thresholds, classical and quantum, and show how the latter consistently tends to the former in the classical limit. We will also discuss the relevance of the quantum non-ergodicity threshold with respect to quantum magnetic reversal.

In Chapter (5), we draw the conclusions concerning the Chapters so far, and point out that long-range interacting systems could have some relevance in designing quantum computing devices. Indeed, in the years of the present Ph.D. research work, we also focused on quantum computation, where interaction plays a crucial role. This is illustrated in Chapter (6), where the results of our research in this field are gathered.

## 1.1 Appendix A : Definition of Ergodicity

Let us consider a dynamical system on a given subspace  $V$ , defined by the dynamical variables  $\mathbf{x}$ . Let  $f(\mathbf{x})$  be a well defined and summable function on  $V$ . The infinite time average of  $f(\mathbf{x})$  is defined as follow:

$$\langle f \rangle^T = \lim_{T \rightarrow \infty} \int_{t_0}^T f(\mathbf{x}(t)) dt$$

Note that Birkhoff proved that this limit exist and that it is independent from  $t_0$ , (16).

While the space average of  $f(\mathbf{x})$  is given by:

$$\langle f \rangle^S = \int_V P(\mathbf{x}) f(\mathbf{x}) d\mathbf{x}$$

where  $P(\mathbf{x})$  is a continuum and invariant Probability distribution. With invariant it is meant:

$$\int_{\Gamma} P(\mathbf{x}) d\mathbf{x} = \int_{\Gamma^t} P(\mathbf{x}) d\mathbf{x}$$

where  $\Gamma$  is a subspace of  $V$  and  $\Gamma^t$  indicates the same subspace at time  $t$ .

We can now give the definition of ergodic dynamical system:

A dynamical system is ergodic if,  $\forall f$ :

$$\langle f \rangle^T = \langle f \rangle^S$$

Note that this implies that  $\langle f \rangle^T$  is independent from the initial conditions.

# Bibliography

- [1] M.Toda, R.Kubo, N.Saito, *Statistical Mechanics* Vol I, Springer-Verlag (1995).
- [2] R.C.Tolman, *The principles of Statistical Mechanics*, Dover Publications (1979).
- [3] besides the attempts to justify the methods of Statistical Mechanics on dynamical grounds, there are other alternative approaches. We recall here one inspired from information theory and based on purely statistical considerations, originally proposed by Janes: Phys. Rev. ,**106**, 620 (1957), Phys. Rev. , **108**, 171 (1957).
- [4] P. Weiss and R.Forrer, Ann. Phys. **5**, 153 (1926).
- [5] A.I.Khinchin *Mathematical Foundations of Statistical Mechanics*, Dover Publications, New York (1949)
- [6] Ya. G. Sinai, *The Boltzmann Equation*, Ed. by E.G.Cohen and W. Thirring, Springer-Verlag (1973).
- [7] R.G. Palmer, Adv. in Phys.**31**, 669 (1982)
- [8] S.A.Cannas, F.A.Tamarit, Phys. Rev. B, **54**, R12661 (1996).
- [9] J. Barré, D. Mukamel, S. Ruffo, Phys. Rev. Lett. **87**, 3, (2001)
- [10] E.Luijten and H.W.J.Blote, Phys. Rev. Lett., **89**, 25703 (2002), M.E. Fisher, S. Ma and B.G.Nickel, Phys. Rev. Lett., **29**, 917 (1972), B.P.Vollmayr-Lee and E.Luijten Phys. Rev. B, **63**, 31108 (2001).
- [11] V. Latora, A. Rapisarda, and S. Ruffo, Phys. Rev. Lett. **80**, 692, (1998), C. Anteneodo, C. Tsallis, Phys. Rev. Lett. **80**, 24, (1998), C. Tamarit, C. Anteneodo, Phys. Rev. Lett. **84**, 208, (2000), M. C. Firpo, Phys. Rev. E **57**, 6599, (1998); M. C. Firpo and S. Ruffo, Journal of Physics A, 34, L511, (2001); C. Anteneodo, R.N.P. Maia and R. Vallejos, Phys. Rev. E **68**, 036120, (2003).
- [12] R. B. Griffiths, C. Y. Weng, and J. S. Langer, Phys. Rev., **149**, 1 (1966), M. Antoni, S. Ruffo and A. Torcini, Europhys. Lett., **66**, 645 (2004), P.H.Chavanis and M.Rieutord Astronomy and Astrophysics, **412**, 1 (2003); P.H.Chavanis, astro-ph/0404251, G.L.Celardo, J.Barre, F.Borgonovi, S. Ruffo, cond-mat/04010119.
- [13] S.A. Cannas and F.A.Tamarit, Phys. Rev. B, **54** , R12661 (1996), A.Campa, A.Giansanti and D.Moroni, Phys. Rev. E, **57**, 615 (1985), F.A.Tamarit and C.Anteneodo, Phys. Rev. Lett., **84**, 208 (2000).
- [14] F.Izrailev, Physics Reports, **196**, 135 (1990).

- [15] T. Dauxois, S. Ruffo, E. Arimondo, M. Wilkens Eds., *Lect. Notes in Phys.*, **602**, Springer (2002).
- [16] V.I. Arnold, A. Avez, *Ergodic Problems of Classical Mechanics*, W.A. Benjamin (1968).
- [17] F. Borgonovi, G. L. Celardo, M. Maianti, E. Pedersoli, *J. Stat. Phys.*, **116**, 516 (2004).
- [18] J. Barré, Phd Thesis, ENS-Lyon, (2003).

## Chapter 2

# Broken Ergodicity

Infernal world, and thou profoundest Hell  
Receive thy new Possessor: One who brings  
A mind not to be chang'd by Place or Time.  
The mind is its own place, and in it self  
Can make a Heav'n of Hell, a Hell of Heav'n.

.....  
Better to reign in Hell, then serve in Heav'n.

—*Paradise Lost*, John Milton

### 2.1 Introduction

In this Chapter we will tell how we lost the “Paradise of Ergodicity”, see citation above. Most of the results presented in this this Chapter have been published in Ref.(1). We expanded some parts and added Sec.(2.5.2). In this Chapter we will define the non-ergodicity threshold, for a class of Classical Heisenberg Models and relate its existence to the long range of interaction and to the anisotropy of the coupling.

It is generally assumed that, due to a sufficiently strong interaction, chaos will provide the mechanism in order to have ergodicity on the energy surface. As we explained in Ch.(1), ergodicity could justify the equal probability hypothesis, which is the basic assumption in building statistical mechanics ensembles. Generally speaking, the degree of chaos will depend on the strength of the interparticle interaction and on the number of particles: it is a common lore that the larger the number of particles, the stronger is chaos, thus leading to more suitable conditions for ergodicity and statistical investigation.

This general behavior is far from being satisfied by many physical systems, as explained by R.G. Palmer in his seminal paper(2) where, using his words: “The breakdown of ergodic behavior is discussed as a general phenomenon in condensed matter physics”. In his paper the breakdown of ergodicity as due to an “effective” confinement of the system, respect to the observational timescale has been put forward. Nonetheless, to the best of our knowledge, there are no single examples where thresholds for broken ergodicity can be found analytically and, more important, where the relation with the interaction range has been remarked explicitly.

The relation between the dynamical properties, like chaos or ergodicity, and the kind of interparticle interaction has been studied since long (3), but only recently this relation has been considered with respect to the long or short range of the interaction (4). Indeed, long-range interacting systems display peculiar properties from the point of view of statistical mechanics. It

is well known for instance that, for such systems, the canonical and the microcanonical ensemble give different results, (5), thus questioning the validity of statistical mechanics. Moreover, chaos suppression in long-range interacting systems when the number of particles increases was recently found(6; 7; 8), and analytically investigated (9), thus leading to anomalous statistical behavior in the thermodynamical limit.

In this Chapter, we investigate a one-dimensional spin chain model with two different ranges of interaction, nearest neighbors and “infinite” (all particles are interacting with all the others). Depending on the interaction range, dynamical properties, as ergodicity and chaoticity are strongly different. Indeed, even in presence of chaoticity(10), the model displays a lack of ergodicity only in presence of all to all interaction and below an energy threshold, which we called the *non-ergodicity threshold*. Such non-ergodic behavior is mainly due to a non-connected phase space and the threshold for non-ergodicity can be obtained analytically. Moreover such non-ergodicity persists in the thermodynamical limit, actually the ratio between the disconnected portion and the whole energy range approaches one, as the number of particles goes to infinity.

Moreover we have found that, for all-to-all interaction, when the number of particles increases, the system dynamics becomes more regular. This is the phenomenon of chaos suppression, yet discussed in Ch.(1). We also give numerical evidence that there is room for chaos in the non-ergodic region, for any finite number of particles.

For sake of comparison, we consider the same model with short range interaction (nearest neighbor coupling) and we prove that this kind of disconnection does not exist. Of course, this does not imply that the system is ergodic, as also supported by our numerical simulations that indicate the presence of regular dynamics in some region of the energy space.

We then generalize our results taking into account a system with generic anisotropy. Finally we consider a Classical Heisenberg Model in which the spins interact through a potential which decays with a given function of the distance among the spins. In this case we prove that the non-ergodicity threshold can exist only if the interaction has a long range behavior.

## 2.2 The Model : chaoticity vs interaction range

Our model is a variant of the one-dimensional Classical Heisenberg model for  $N$ -spins,(11) . The Hamiltonian is given by:

$$H = J \sum_{\langle i,j \rangle} (S_i^x S_j^x - S_i^y S_j^y) \quad (2.1)$$

where  $\langle i,j \rangle$  stands for nearest neighbor ( $\mathcal{N}$ -interaction), or infinite range couplings (all-to-all,  $\mathcal{A}$ -interaction) and  $J$  is a positive constant. Since  $J$  is a multiplicative constant we could eliminate it with a proper rescaling of time, nevertheless we prefer to keep it because in the following we will use two different values of  $J$  depending to the kind of interaction,  $\mathcal{N}$ -interaction or  $\mathcal{A}$ -interaction.

Through the relations :

$$\dot{S}_i^\gamma = [S_i^\gamma, H],$$

where  $\gamma = x, y, z$ , Hamiltonian (6.3) gives rise to the standard nonlinear equations of motion:

$$\begin{cases} \dot{S}_i^x &= -JS_i^z \sum_{\langle j \rangle} S_j^y \\ \dot{S}_i^y &= -JS_i^z \sum_{\langle j \rangle} S_j^x \\ \dot{S}_i^z &= J \sum_{\langle j \rangle} (S_i^y S_j^x + S_i^x S_j^y), \end{cases} \quad (2.2)$$

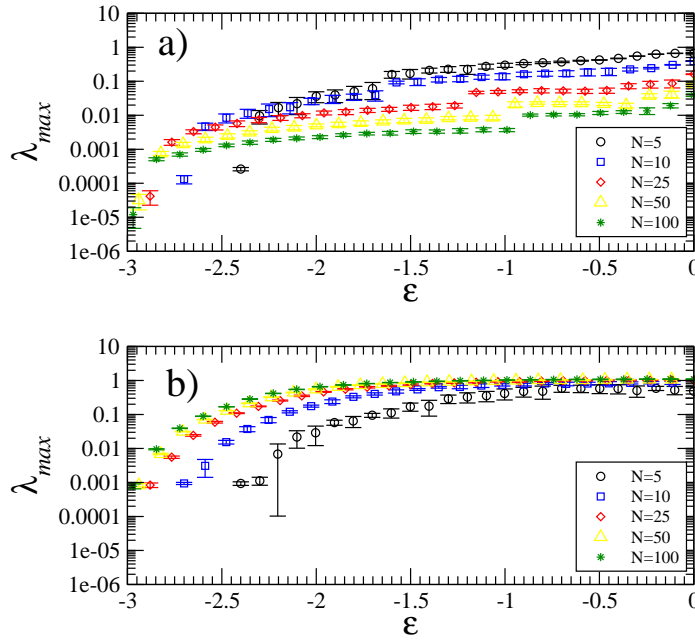


Figure 2.1: a) Maximal Lyapunov exponent,  $\lambda_{max}$ , for different number of particles  $N = 5$  (black) ,  $N = 10$  (blue),  $N = 25$  (red),  $N = 50$  (yellow) and  $N = 100$  (green), as a function of the energy per particle  $\epsilon = E/N$ , for  $\mathcal{A}$ -interaction a), and for  $\mathcal{N}$ -interaction b). Error bars have been obtained as the standard deviation from a set of 20 initial trajectories on the same energy surface. Trajectories have been integrated for a time of  $10^4$ . In a) the interaction constant has been chosen as  $J = 2I/N$ , with  $I = 3$ , while in b)  $J = I = 3$ .

where  $\langle j \rangle$  is a shorthand notation for  $j \neq i$  (in the case of  $\mathcal{A}$ -interaction) , and  $j = i \pm 1$  when  $\mathcal{N}$  interaction (without periodic boundary conditions) is assumed.

Constants of motion are the energy  $H = E$ , and the  $N$  squared moduli  $|\mathcal{S}_i|^2$  (which we set equal to 1 for simplicity). For  $N = 2$ , an additional constant of motion, in involution with the others, is given by  $S_1^z - S_2^z$ , and the system becomes exactly integrable.

Let us notice that, in general, the only free parameters are the total energy  $E$ , the interaction strength  $J$  and the number of particles  $N$ . Moreover, for any finite number of particles  $N$ , the energy is bounded  $|E| \leq E_{max}(J, N)$ . A rough estimate for such border are:  $E_{max} \sim JN^2$  for  $\mathcal{A}$ -interaction and  $E_{max} \sim JN$  for  $\mathcal{N}$ -interaction. Nevertheless the rigorous bound will be given below.

In order to make a fruitful comparison between  $\mathcal{N}$  and  $\mathcal{A}$  interaction and according to a general prescription (12) we rescale, for  $\mathcal{A}$  interaction, the strength  $J$  to the number of particles  $N$ , setting  $J = 2I/N$ . In this way the energy of  $\mathcal{A}$  systems scales with the number of particles in the same way as for  $\mathcal{N}$  systems. Note that with this rescaling the  $\mathcal{A}$  system becomes extensive but not additive.

For  $N > 2$ , and sufficiently strong interaction (both  $\mathcal{N}$  and  $\mathcal{A}$  interaction) the system is chaotic in a large energy range  $|E| < |E_{ch}(j, N)| < E_{max}$ , as indicated by a maximal positive Lyapunov exponent. From now on, all results will be restricted to the chaotic energy region only.

Chaotic properties of the model have been analyzed within the frame of Standard Lyapunov analysis(13; 14). In Fig.(2.1) we show the maximal Lyapunov exponent as a function of the energy per particle  $\epsilon = E/N$  for different number of particles and  $\mathcal{A}$  (upper) and  $\mathcal{N}$  (lower)

interaction. As one can see, while the maximal Lyapunov exponent  $\lambda_{max}$  depends on the energy per particle in some peculiar way, there is a large energy region where it is appreciably different from zero for both interactions. From the same picture it is clear that while increasing the number of particles in the case of  $\mathcal{N}$  interaction, does not produce an appreciable variation of  $\lambda_{max}$ , the same variation in  $N$ , for  $\mathcal{A}$  interaction, effectively decreases the value of  $\lambda_{max}$ . Even if it is difficult to give an exact scaling relation of the maximal Lyapunov exponent with all the system parameters  $(E, N, J)$  the approximate relation  $\lambda_{max}(E = 0, I = 3) \sim 1/N^\alpha$  holds, where  $\alpha = 0$  for  $\mathcal{N}$  interaction and  $\alpha = 1$  for  $\mathcal{A}$  interaction, see Fig. (2.2).

The numerical results and the corresponding approximate relations are shown in Fig.(2.2) and indicate the absence of a chaotic dynamics for all-to-all interacting systems with a large number of particles. This is what is called in literature *chaos suppression* in long range interacting systems (15). Note that chaos suppression in this model is much stronger than in other models with infinite range coupling (7; 15) where  $\alpha = 1/3$ . Note that the  $1/N$  decrease of the Lyapunov exponent cannot be explained only by the fact that the interaction strength also decreases as  $1/N$ , since two things change: we increase  $N$  and we decrease  $J$ . Indeed an increase of  $N$  also change the chaoticity of the system, for instance for  $N = 2$  the system is integrable while for larger  $N$  it becomes chaotic.

The general trend where the maximal Lyapunov exponent decreases with the number of particles can be understood from the fact that in the limit  $N \rightarrow \infty$  and for  $\mathcal{A}$  interaction the model becomes close to an integrable one.

Indeed the Hamiltonian per particle can be written as:

$$\frac{H}{N} = I h_0 + \frac{I}{N} h_1 \quad (2.3)$$

where  $h_0 = m_x^2 - m_y^2$  and  $h_1 = \frac{1}{N} \sum_{i=1}^N [(S_i^y)^2 - (S_i^x)^2]$  where we have defined the average magnetization  $m_k = \frac{1}{N} \sum_{i=1}^N S_i^k$ , with  $k = x, y$ .

While both  $h_0$  and  $h_1$  remain on order 1 in the limit of large  $N$ , and fixed interaction strength  $I$ , the constant in front of  $h_1$  goes to zero and the  $h_0$  term dominates. A close inspection(16), and our numerical results indicate that  $h_0$  represents an integrable model for any choice of parameters. This is a generic feature of chaos suppression in long range interacting systems: usually, because of long range, as  $N$  increases, most of the energy of the system is assigned to collective motions which, usually, turn out to be integrable.

## 2.3 Ergodicity : numerical results

While in two degrees of freedom systems the absence of ergodic motion in presence of chaos is somehow obvious (due to the presence of invariant tori), for many degrees of freedom systems the same occurrence is far from being trivial. In spite of that, we will now show that, for  $\mathcal{A}$  interaction, an energy threshold exists below which one cannot have ergodic motion.

In order to verify that a given function of the phase space has the ergodicity property we have to compare time averages with phase space averages. We sampled our phase space points from a uniform probability distribution over all the phase space (17), keeping those phase points for which  $H$  was in the desired energy interval. Now, because we set the spin modulus equal to one, the uniform distribution follows if we chose each spin in a uniform way on the unit sphere. We can achieve a uniform distribution over the unit sphere, if we choose  $S^z$  from a uniform distribution, between  $-1$  and  $+1$ , and the angle  $\phi$  in a uniform way between  $0$  and  $2\pi$ , where  $\phi$  is the angle between the  $x$  axis and the projection of  $\mathbf{S}_i$  over the  $xy$  plane.

Let us first consider for a fixed energy, the phase and time average of the mean magnetization along the  $y$  direction. Phase distributions have been obtained numerically by choosing an

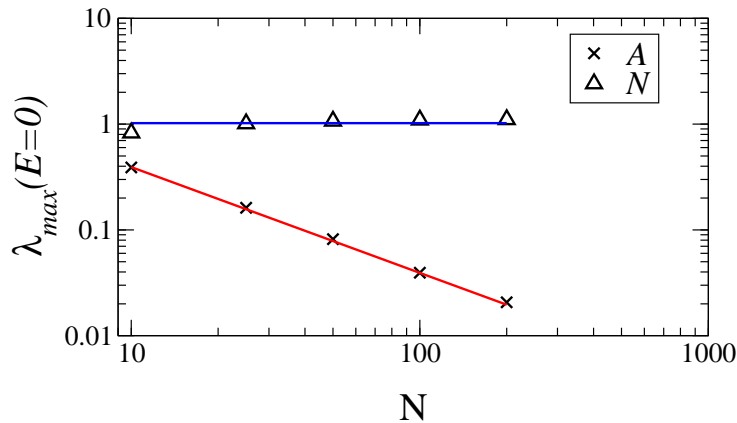


Figure 2.2: Maximal Lyapunov exponent as a function of the number of particles, for the same parameters of Fig.(2.1) and  $E = 0$ . Triangles refer to  $\mathcal{A}$  interaction, while crosses are for  $\mathcal{N}$  interaction. Also shown the best fit lines  $\lambda_N = 1.1 \pm 0.2$ (blue) and  $\lambda_A = (4.1 \pm 0.1)/N$  (red).

ensemble  $M$  of different points upon the energy surface and by taking the simple average

$$\bar{m}_y = \frac{1}{M} \sum_{j=1}^M m_y^{(j)} \quad (2.4)$$

where  $m_y^{(j)} = (1/N) \sum_{i=1}^N s_y^{i(j)}$  is the  $y$  component of the magnetization of the  $j$ -th element of the ensemble.

In the same standard way the time average can be obtained by taking one single point onto the energy surface, iterating it in time using the equations of motion (2.2) and computing its values at different times  $t_j$ , so that

$$\langle m_y \rangle = \frac{1}{T} \sum_{t=1}^T m_y(t) \quad (2.5)$$

Should the system be ergodic the averages (2.4) and (2.5) give the same result. Instead of comparing the averages (2.4) and (2.5) we consider the distributions,  $P^p(m_y)$  and  $P^t(m_y)$  and compare them directly.

Phase and time distributions of the mean magnetization are shown in Fig.(2.3) for the  $\mathcal{N}$ -interaction (right column) and  $\mathcal{A}$ -interaction (left column) with the same number of particles. All cases are characterized by a chaotic dynamics, as given by a maximal positive Lyapunov exponent, see Fig. (2.1).

As one can see, while for nearest neighbor interaction there is a good correspondence between the two averages (this of course does not mean ergodicity), in the case of all-to-all interaction there are strong deviations, in the lower energy case, see Fig.(2.3a). More precisely one trajectory with an initial  $m_y > 0 (< 0)$  cannot reach a region with  $m_y < 0 (> 0)$ , below some energy threshold. Another difference is related to the presence of a two-peaks distribution: this indicates the presence of a phase transition and it will be the subject of the next Chapter.

Strictly speaking, from these numerical results one can only infer that the time of transition from one peak to the other one is much larger than the simulation time. Nonetheless, in the next section we will show that such transition time does not exist. The origin of this deviation is that for those energy values less than the energy threshold the phase space is metrically decomposable(18) thus making the  $\mathcal{A}$  system rigorously non-ergodic.

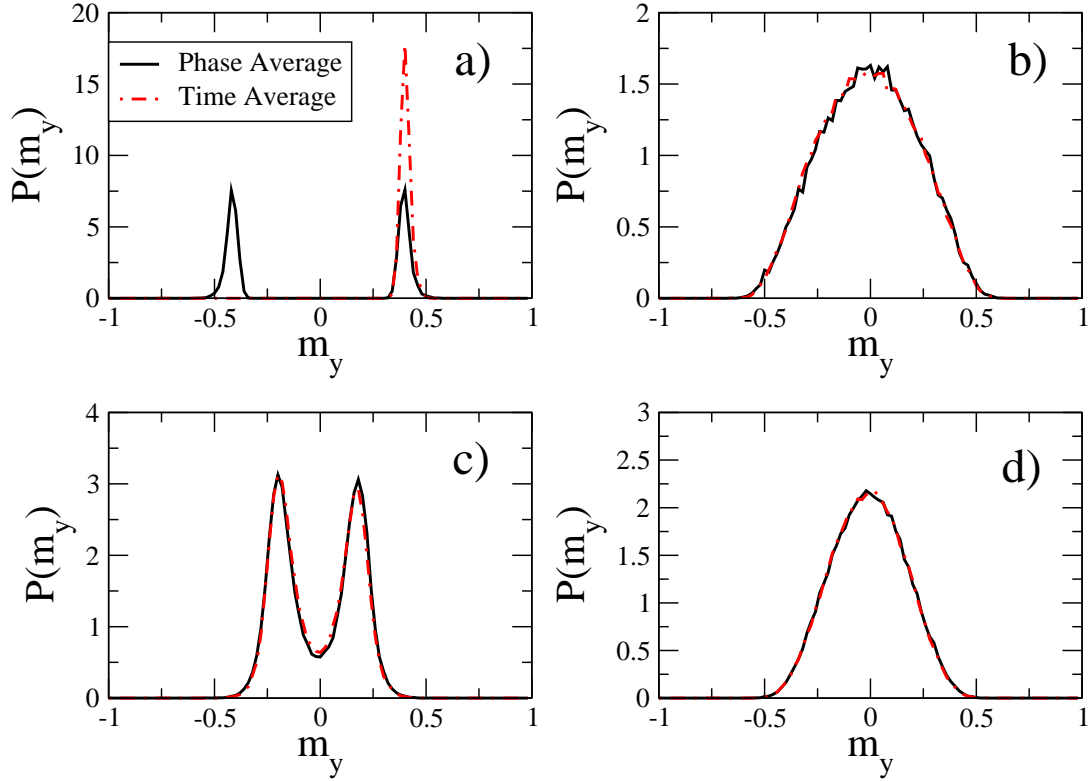


Figure 2.3: Distribution of mean magnetization along the  $y$ -axis for  $\mathcal{A}$  interaction (left column) and  $\mathcal{N}$  interaction (right column). As black lines we show the phase distributions,  $P^p(m_y)$ , while red ones stand for time distributions,  $P^t(m_y)$ . Phase distributions have been obtained taking  $M = 10^5$  different initial conditions upon the energy surface  $E = -5$ , a) and b) and  $E = -1$ , c) and d), while time averages have been obtained by computing one single trajectory in time on the same energy surface for a time  $T = 10^5$  and taking values at time steps  $\Delta t = 1$ . Results have been checked on increasing the number of initial points upon the energy surface for the phase average, and on increasing the integration time  $T$  for the time average. Here is  $N = 10$ , and  $I = 3$ . Maximal Lyapunov exponents are positive for all the cases shown in this figure, as can be deduced from Fig.(2.1).

## 2.4 Non-Ergodicity Threshold: analytical results

The existence of a threshold for the non ergodicity in case of  $\mathcal{A}$  interaction can be proved by the following argument. Let us assume that initially the spins are oriented in such a way that  $m_y(0) > 0$  with the energy  $E$ . It is clear that if we are able to prove that when  $E < E_{ne}$  one cannot have the solution  $m_y = 0$  on the energy surface  $H = E$ , it means that the trajectory should keep, for any time  $m_y(t) > 0$ . Since reversal of  $y$  single spin components results in change of  $y$  magnetization but not of the energy, the same argument can be applied to  $m_y(0) < 0$  as well. In other words the space is metrically decomposable, since one trajectory with  $m_y > 0$  cannot reach the region where  $m_y < 0$  (and viceversa), although both regions belong to the same energy surface.

In order to find the explicit value of  $E_{ne}$  one should consider the problem of minimizing the value of the energy  $E$  under the constraint  $m_y = (1/N) \sum_{i=1}^N S_i^y = 0$ , which means that the non-ergodicity threshold is defined in the following way:

$$E_{ne} = \min\{H|m_y = 0\}. \quad (2.6)$$

In principle this task can be faced by means of the Lagrange multipliers. Nevertheless from a very simple argument we can estimate the critical energy  $E_{ne}$ .

Let us first derive the minimal energy,  $E_{min}$ , and then the non-ergodicity energy,  $E_{ne}$ , for both  $\mathcal{N}$  and  $\mathcal{A}$  systems. Of course, only in the case  $E_{ne} > E_{min}$  the non-ergodicity threshold has some relevance, because it implies that the energy region between  $E_{ne}$  and  $E_{min}$  is disconnected.

### 2.4.1 Minimal energy

We can find the minimal energy by minimizing the Hamiltonian (6.3) under the constraint:

$$(S_i^x)^2 + (S_i^y)^2 + (S_i^z)^2 = 1, \quad i = 1, \dots, N \quad (2.7)$$

We can take conditions (2.7) into account, switching to spherical coordinates:

$$\begin{cases} S_i^x &= \sin(\theta_i) \cos(\phi_i) \\ S_i^y &= \sin(\theta_i) \sin(\phi_i) \\ S_i^z &= \cos(\theta_i). \end{cases} \quad (2.8)$$

We can now rewrite Hamiltonian (6.3) as:

$$H = J \sum_{\langle i,j \rangle} \sin(\theta_i) \sin(\theta_j) \cos(\phi_i + \phi_j) \quad (2.9)$$

where

$$J = \begin{cases} (2I/N) & \text{for } \mathcal{A}\text{-interaction} \\ I & \text{for } \mathcal{N}\text{-interaction} \end{cases} \quad (2.10)$$

One absolute minimum value is obtained, for instance, setting:

$$\begin{cases} \sin(\theta_i) &= 1 \\ \cos(\phi_i + \phi_j) &= -1 \end{cases} \quad (2.11)$$

where  $j = i + 1$  for  $\mathcal{N}$  system and  $j \neq i$  for  $\mathcal{A}$  system.

While the first equation of (2.11) can be easily satisfied by both  $\mathcal{N}$  and  $\mathcal{A}$  system, assuming

$$\theta = \frac{\pi}{2} \quad (2.12)$$

some care should be taken in order to fulfill the second one.

For  $\mathcal{N}$  system, we can put for instance:

$$\begin{cases} \phi_i = 0 & \text{for } i \text{ even} \\ \phi_i = \pi & \text{for } i \text{ odd} \end{cases} \quad (2.13)$$

On the contrary, for  $\mathcal{A}$  system, we set

$$\phi_i = \pi/2 \quad \text{for } i = 1, \dots, N. \quad (2.14)$$

Taking into account that there are  $N - 1$  couplings in the  $\mathcal{N}$  system and  $N(N - 1)/2$  in the  $\mathcal{A}$  system, the minimal energy is given by (for both interactions):

$$E_{min} = -I(N - 1). \quad (2.15)$$

## 2.4.2 Non-ergodicity threshold

We define the non-ergodicity threshold  $E_{ne}$  in such a way that for any energy  $E < E_{ne}$  the system is metrically decomposable. In order to find this non-ergodicity (or disconnection) energy we have to find the minimum of Hamiltonian (6.3) under the additional constraint

$$m_y = 0. \quad (2.16)$$

For  $\mathcal{A}$  system Hamiltonian (6.3) can be written as,

$$H = -\frac{I}{N} \sum (S_i^x)^2 + \frac{I}{N} \sum (S_i^y)^2 + INm_x^2 - INm_y^2 \quad (2.17)$$

Let us now search for the minimum of (2.17) under the constraints (2.7) and (2.16). In (2.17) the only term that can be negative under the given constraints is the first one, therefore,

$$E_{ne} \geq -I$$

If it is possible to minimize this term putting at the same time all the other to zero, we get the non-ergodicity energy.

When  $N$  is even we can put half spins with  $S_i^x = +1$ , and half such that  $S_i^x = -1$ . In this way  $m_x = 0$ ,  $S_i^y = 0$  and  $m_y = 0$ , so that:

$$E_{ne} = -I, \quad \text{for } N \text{ even}$$

When  $N$  is odd we cannot minimize the first term in (2.17), and at the same time let the other terms to be zero, so that:  $E_{ne} > -I$ , for  $N$  odd.

Anyway it is easy to give an upper bound for  $E_{ne}$  which is sufficient for our scope. Indeed we can arrange  $N - 1$  spins as in the previous case, and for the last spin we assume  $S_N^z = \pm 1$ . In this way we have  $m_x = 0$ ,  $S_i^y = 0$  and  $m_y = 0$ , so that:

$$-I < E_{ne} \leq -I + I/N, \quad \text{for } N \text{ odd}$$

For  $\mathcal{N}$  system, the non-ergodicity energy, if defined as the minimum energy for which Eq.(2.16) holds, coincides with the minimal energy. Indeed the same values of  $\phi_i$  (2.13) and  $\theta_i$  (2.12) which minimize the Hamiltonian, satisfy condition (2.16) too, so that:

$$E_{ne} = E_{min} = -I(N - 1)$$

$\mathcal{A}$	$E_{min}$	$E_{ne}$
$N_{even}$ :	$-I(N-1)$	$-I$
$N_{odd}$ :	$-I(N-1)$	$(-I, -I + I/N]$

Table 2.1: Minimal and non-ergodicity energy for  $\mathcal{A}$  system. Note that in the case of odd number of particles we give a lower and an upper bound for the non-ergodicity energy.

$\mathcal{N}$	$E_{min}$	$E_{ne}$
	$-I(N-1)$	$-I(N-1)$

Table 2.2: Minimal and non-ergodicity energy for  $\mathcal{N}$  system.

This of course does not exclude the possibility to have some other constraint that produces a disconnected phase space (even if such conclusion is not supported by our numerical simulations).

In Tables 2.1 and 2.2 we summarize the minimal and non-ergodicity energies found.

As an interesting consequence of our results we note that the ratio:

$$r = \frac{|E_{ne} - E_{min}|}{|E_{min}|} \quad (2.18)$$

between the disconnected portion of the energy range and the total energy range, in the limit of a large number of particles at fixed interaction strength, goes to one for  $\mathcal{A}$  interaction, and is exactly zero for  $\mathcal{N}$  interaction, thus showing that in this limit the energy range is completely disconnected for  $\mathcal{A}$  interaction only (note that in the positive region of the energy range the same argument used to show the existence of a non-ergodicity energy can be applied considering  $m_x$  instead of  $m_y$ ).

As one can see, for  $\mathcal{A}$  interaction, as the number of particles increases the region of non-ergodicity does not decrease thus indicating that caution should be taken when ergodicity is tacitly assumed due to small interactions between many particles.

The presence of the non ergodic region is not related with the chaoticity of the system. Indeed for any  $N$  we can find an  $I$  value such that there is developed chaos for  $E < E_{ne}$ . In order to validate this statement, we show in Fig.(2.4) how the maximal Lyapunov exponent varies as a function of  $I$ . More precisely the Lyapunov exponent has been computed for any  $N$  exactly at the non-ergodicity energy threshold,  $E = E_{ne}$ . As one can see  $\lambda(E_{ne})$  increases linearly with  $I$ , thus showing that, for any  $N$  fixed, it is possible to choose  $I$  such that the system is chaotic and non-ergodic, below  $E_{ne}$ . Note that this result is not just a trivial consequence of the fact that the Lyapunov exponent grows linearly with  $I$  at fixed energy. Actually  $E_{ne}$  changes with  $I$ , so that when we compute  $\lambda(E_{ne})$  as  $I$  increases, also the energy changes.

## 2.5 Generalization

Let us finally mention that the previous results can be easily generalized. We will first consider the generalization to a generic anisotropic coupling. We will then analyze what is possible to say when the interaction among spins decays like  $R^{-\alpha}$ .

### 2.5.1 Generic Anisotropy

Let us consider a generic  $XY$  Model:

$$H = -J \sum_{\langle i,j \rangle} (S_i^y S_j^y + \eta S_i^x S_j^x) \quad (2.19)$$

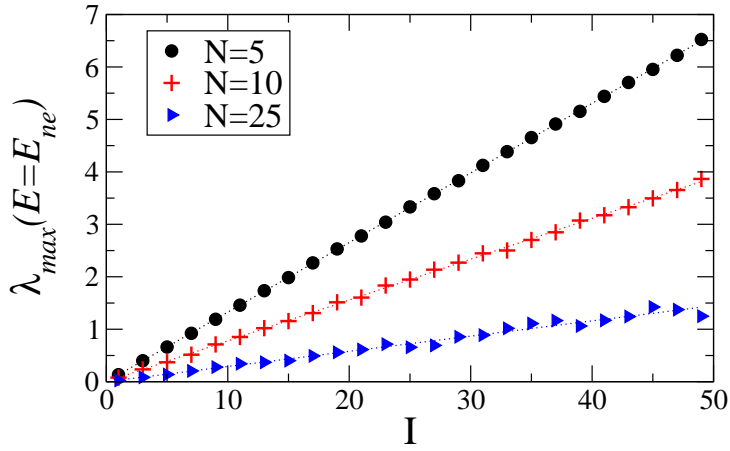


Figure 2.4: Maximal Lyapunov exponent as a function of the interaction strength  $I$  for  $\mathcal{A}$  interaction, at the energy threshold  $E = E_{ne}$ . for different number of particles  $N$  as indicated in the legend. Dotted lines show linear fitting.

where  $|\eta| \leq 1$  and  $J > 0$ . Following the same arguments given above, we can show the existence of a non-ergodicity energy and roughly estimate their dependence on system parameters.

We will mainly focus on the ratio between the disconnected portion of the energy range and the total energy range,  $r$ , Eq. (2.18), in the limit of a large number of particles.

For  $\mathcal{A}$  interaction, we can rewrite the Hamiltonian (2.19) as:

$$H = \frac{J}{2} \sum_i \left[ \eta (S_i^x)^2 + (S_i^y)^2 \right] - \frac{J}{2} N^2 (\eta m_x^2 + m_y^2) \quad (2.20)$$

From this equation we can estimate, for large  $N$

$$E_{min} \sim -\frac{J}{2} N^2,$$

As for the non-ergodicity energy, following the same procedure described in the previous section, we have:

$$E_{ne} \simeq \begin{cases} -\frac{J}{2} N^2 \eta & \text{for } \eta > 0 \\ 0 & \text{for } \eta = 0 \\ \frac{J}{2} N \eta & \text{for } \eta < 0 \end{cases} \quad (2.21)$$

so that

$$r \simeq \begin{cases} 1 - \eta & \text{for } \eta > 0 \\ 1 & \text{for } \eta \leq 0 \end{cases} \quad (2.22)$$

where we have neglected  $O(1/N)$  terms.

As one can see  $r = 0$  only for  $\eta = 1$ , while  $r \neq 0$  for asymmetric coupling.

For the  $\mathcal{N}$  case, we have that

$$E_{min} \sim -J(N - 1),$$

while

$$-J(N - 1) \leq E_{ne} \leq -J(N - 3)$$

as one can see setting, for instance,

$$S_i^x = \begin{cases} 1 & \text{for } i \text{ odd} \\ -1 & \text{for } i \text{ even} \end{cases} \quad (2.23)$$

Note that for  $N \gg 1$ ,  $E_{min} \simeq E_{ne}$  so that  $r = 0$  for any  $\eta$ , in the  $\mathcal{N}$  case.

Thus, we can conclude that broken ergodicity is generic for asymmetric coupling and all-to-all interaction.

### 2.5.2 $1/R^\alpha$ Interaction

We consider a classical Heisenberg model with anisotropic coupling and an interaction among spins which decays as  $1/R^\alpha$  (20), where  $R$  is the distance among spins and  $\alpha$  a real parameter which varies in the range  $[0, \infty]$ . Note that for  $\alpha \rightarrow 0$  we recover the  $\mathcal{A}$  interaction, while for  $\alpha \rightarrow \infty$  we have the  $\mathcal{N}$  interaction.

We consider a system described by the following Hamiltonian:

$$H = -J \sum_{\langle i,j \rangle} \frac{1}{R^\alpha} (S_i^y S_j^y) + J \sum_{\langle i,j \rangle} \frac{1}{R^\alpha} (S_i^x S_j^x) \quad (2.24)$$

In the following we limit our considerations to the one dimensional case,  $d = 1$ .

The Hamiltonian(2.24), switching to spherical coordinates (2.8), can be rewritten as

$$H = J \sum_{\langle i,j \rangle} \frac{1}{R^\alpha} \sin(\theta_i) \sin(\theta_j) \cos(\phi_i + \phi_j). \quad (2.25)$$

Now, the sum(2.25) is minimized if we can minimize each addend. Because the  $1/R^\alpha$  term is always positive, setting all the spins along the  $y$  direction, namely setting  $\theta_i = \pi/2$  and  $\phi_i = \pi/2$ , we have the minimal energy configuration, with:

$$E_{min} = -J \sum_{\langle i,j \rangle} \frac{1}{R^\alpha} \quad (2.26)$$

Note that this same configuration(all spins directed along the  $y$  direction) minimize the energy for any dimension,  $d$ . The minimal energy can be also written as:

$$E_{min} = -J \sum_{k=1}^{N-1} \sum_{l=1}^{N-k} \frac{1}{l^\alpha} \quad (2.27)$$

Let us now consider the following configuration: we put half of the spins up along the positive  $y$  direction and half of the spins down (we are supposing an even number of spins for simplicity). We can represent this configuration in the following way:

$$\dots \uparrow\uparrow\uparrow \dots \downarrow\downarrow\downarrow \dots$$

Let us indicate the energy of this configuration as  $E_{\uparrow\downarrow}$ . If we suppose to divide into two halves also the configuration that minimize the energy in such a way to have:

$$\dots \uparrow\uparrow\uparrow \dots \uparrow\uparrow\uparrow \dots$$

It is straightforward to realize that  $E_{min} = E_1 + E_2 - V$ , and  $E_{\uparrow\downarrow} = E_1 + E_2 + V$ , where  $E_1$  and  $E_2$  are the energy of the two halves, considered as independent, and  $V$  is the interaction energy between the two halves. We thus have:

$$E_{\uparrow\downarrow} - E_{min} = 2V, \quad (2.28)$$

where  $V$  can be written as:

$$V = J \sum_{k=1}^{N/2} \sum_{l=k}^{N/2+k-1} \frac{1}{l^\alpha} \quad (2.29)$$

Now, we are interested in computing the ratio  $r_{\uparrow\downarrow}$  which is given by:

$$r_{\uparrow\downarrow} = \frac{|E_{\uparrow\downarrow} - E_{min}|}{|E_{min}|} = \frac{2V}{|E_{min}|} \quad (2.30)$$

Eq.(2.30) allows us to make a general consideration. The configuration  $(\uparrow\downarrow)$  satisfies the constrain  $m_y = 0$  so that  $E_{\uparrow\downarrow} \geq E_{ne}$ . This implies that  $r_{\uparrow\downarrow} > r$ , where  $r$  is defined by Eq.(2.22). From Eq.(2.30) we have that if  $V$  is negligible, for  $N \rightarrow \infty$ , with respect to  $E_1$  and  $E_2$ , then  $r_{\uparrow\downarrow} \rightarrow 0$ , which implies that  $r \rightarrow 0$ . Let's put it in words: if the interaction energy between the two halves of the considered configuration  $\uparrow\downarrow$  is negligible in the large  $N$  limit respect to the energies of the two halves considered independently, then the disconnected portion of the spectrum vanishes.

The interaction energy  $V$ , Eq.(2.29), and  $E_{min}$ , Eq.(2.27), can be evaluated explicitly by substituting sums with integrals, the result is:

$$\begin{aligned} V &\sim -\frac{1}{(1-\alpha)(2-\alpha)} \left[ \frac{2-2^\alpha}{2} N^{2-\alpha} + 1 \right] \\ E_{min} &\sim \frac{N}{1-\alpha} + \frac{1}{(1-\alpha)(2-\alpha)} [1 - N^{2-\alpha}] \end{aligned} \quad (2.31)$$

Then we have computed  $r_{\uparrow\downarrow}$ , as  $N \rightarrow \infty$ , we have the following results:

$$r_{\uparrow\downarrow} \rightarrow 0 \text{ for } \alpha > 1 \quad (2.32)$$

$$r_{\uparrow\downarrow} \rightarrow 2 - 2^\alpha \text{ for } \alpha < 1 \quad (2.33)$$

So that we can say that for  $N \rightarrow \infty$  the non-ergodicity threshold doesn't exist for  $\alpha > 1$ .

We think that it is possible to generalize these results to any dimension,  $d$ . Work is still in progress.

On the other side, nothing can be said of the long range case: even if we prove that for the configuration  $(\uparrow\downarrow)$ ,  $r_{\uparrow\downarrow}$  remain finite for  $N \rightarrow \infty$ , there could be another configuration, let's call it  $(c)$ , which satisfies the condition  $m_y = 0$ , and for which  $r_c \rightarrow 0$  as  $N \rightarrow \infty$ . That means that we did not prove the existence of the non-ergodicity threshold for  $\alpha < 1$ , unless  $\alpha = 0$ , of course.

Note that if the interaction is isotropic, ( $\eta = 1$ ), then it can be easily shown, following the same arguments presented in this section, that the non-ergodicity threshold does not exist whatever the range of the interaction.

## 2.6 Conclusions

In conclusion we have studied a spin chain model from the dynamical point of view for two different ranges of inter-spin interaction (nearest neighbor and all-to-all). Both models are mainly

chaotic, in the sense that the dynamics is characterized by a positive maximal Lyapunov exponent in a wide energy region. Nevertheless, in the case of an infinite range of interaction, the motion does not explore the whole energy surface. This can be understood on the basis of a special topology of the phase space. An analytical estimate gives an energy threshold, the non-ergodicity threshold, below which the system is rigorously non-ergodic: the existence of this threshold has been also confirmed by numerical simulations. Note that the origin of the non-ergodicity threshold is topological and it is thus completely independent from dynamical properties, such as chaoticity. Moreover, for any interaction strength, on increasing the number of particles the range of energy values characterized by such non ergodic motion spans a finite portion of the whole energy range, if the interaction has an infinite range. This could be particularly relevant in the study of multidimensional systems, where usually ergodicity is tacitly assumed for a large number of weak-interacting particles. We have also shown that this phenomenon is generic for Classical Heisenberg Models with anisotropic coupling. Moreover we showed that if we consider an interaction which decays as  $R^{-\alpha}$  with the distance, then for  $\alpha > 1$ , the non-ergodicity threshold does not exist. On the basis of this result and numerical simulations we conjecture that the non-ergodicity threshold exist if a generic long-range anisotropic system is considered.



# Bibliography

- [1] F. Borgonovi, G. L. Celardo, M. Maianti, E. Pedersoli, J. Stat. Phys., **116**, 516 (2004).
- [2] R.G. Palmer, Adv. in Phys.**31**, 669 (1982)
- [3] Chirikov B.V. and Izrailev F.M. 1966 Sov. Phys. Dokl 11, N 1, 30.
- [4] A. Campa et al, Phys. Lett. A **286**, 251, (2001)
- [5] J. Barré, D. Mukamel, S. Ruffo, Phys. Rev. Lett. **87**, 3, (2001)
- [6] V. Latora, A. Rapisarda, and S. Ruffo, Phys. Rev. Lett. **80**, 692, (1998)
- [7] C. Anteneodo, C. Tsallis, Phys. Rev. Lett. **80**, 24, (1998)
- [8] C. Tamarit, C. Anteneodo, Phys. Rev. Lett. **84**, 208, (2000)
- [9] M. C. Firpo, Phys. Rev. E **57**, 6599, (1998); M. C. Firpo and S. Ruffo, Journal of Physics A, **34**, L511, (2001); C. Anteneodo, R.N.P. Maia and R. Vallejos, Phys. Rev. E **68**, 036120, (2003).
- [10] According to the common lore we here call chaotic system the ones characterized in some parameters range by a positive maximal Lyapunov exponent.
- [11] G. S. Joyce, Phys. Rev. **155**, 2 (1967).
- [12] J. Barré, T. Dauxois, S. Ruffo, Physica A **295**, 254 (2001)
- [13] G. Benettin, Physica **13D**, (1984) 211.
- [14] A.J. Lichtenberg and M.A. Lieberman, *Regular and Stochastic Motion*, Applied Math. Series 38 Springer-Verlag (1983)
- [15] M.C. Firpo, S. Ruffo, J. Phys. A, **34**, No 37, L511-L518, (2001).
- [16] in preparation.
- [17] M. Feingold, A. Peres, Physica **9D**, 433-438 (1983). In this article it is shown that for a spin system whose equations of motion are determined by  $\dot{S}_i^\gamma = [S_i^\gamma, H]$ , which is our case, the Liouville theorem is still valid, in the phase space determined by  $S_i$ . Also the difficulty to define an invariant surface measure is discussed.
- [18] A.I. Khinchin *Mathematical Foundations of Statistical Mechanics*, Dover Publications, New York (1949)
- [19] F. Borgonovi, G. Celardo, F. M. Izrailev, G. Casati, Phys. Rev. Lett. **88**, 5, (2002)
- [20] F. Borgonovi, G. Celardo, A. Musesti and R. Trasarti-Battistoni, in preparation.



## Chapter 3

# Time Scale for Chaotic Driven Magnetic Reversal

Aujourd'hui l'espace est splendide!  
Sans mors, sans éperons, sans bride,  
Partons a cheval sur le vin  
Pour un ciel feerique et divin!

—*Les Fleurs du Mal, Le Vin des Amants, Charles Baudelaire*

### 3.1 Introduction

The main results presented in this Chapter can be found in (1), nevertheless the discussion has been widely expanded, with new figures, and new results.

In the previous Chapter we have established the existence of a non-ergodicity threshold,  $\epsilon_{ne}$  in a Classical Heisenberg Model with an infinite range of the interaction (All-to-All) and anisotropic coupling. Below the non-ergodicity threshold, the constant energy phase space is disconnected in two components (subspaces), one for which the total magnetization is positive, and one for which is negative. One of the main consequence of this is that the magnetization cannot change sign in time. Below the non-ergodicity threshold there are no regions of the phase space for which the magnetization is zero, so that, because the dynamics is continuum, the magnetization cannot reach a region of phase space characterized by an opposite sign of the magnetization. This implies that time averages of the magnetization, below  $\epsilon_{ne}$ , will be always different from zero.

It is thus interesting to investigate what is the relation between the non-ergodicity threshold and the prediction of Statistical Mechanics respect to ferromagnetic/paramagnetic phase transition. We show that statistical mechanics predicts a phase-transition at an energy higher than the ergodicity threshold. Moreover we show that the non-ergodicity threshold and the statistical one, when they exist, are distinct for any finite number of spins.

Above the non-ergodicity threshold the magnetization can, in principle, reverse its sign, we will describe how later, for the moment it is interesting to compare the behaviour of our system with standard magnetic systems with short range interactions displaying a phase transition in the thermodynamic limit. In the standard Ising (or Heisenberg) model with short range interactions, below the critical temperature, reversing the order parameter (magnetization) requires a time of order  $O(\exp(\sqrt{N}))$ , where  $N$  is the total number of spins. Broken ergodicity appears in the thermodynamic limit, due to the exponential divergence of the reversing time (2).

Another type of broken ergodicity, not induced by the thermodynamic limit, can be caused by disconnections of the energy surface. Although it can generically appear only in low-dimensional phase-spaces, this effect is uncommon at large  $N$ . However, as we showed in the previous Chapter, below a given specific energy, an anisotropic classical Heisenberg model with all-to-all spin coupling exhibits this type of broken ergodicity for all  $N$ . Moreover, it is well known that, for systems with long-range interactions (4), the escape time from metastable states diverges like  $\exp(N)$  (5; 6; 7). Comparing with the reversing time quoted above for the Ising model, ergodicity breaking due to the large  $N$  limit is stronger for long-range interactions. Being related with the infinite range nature of the interaction, the presence of a *non-ergodicity threshold* could appear, at a first glance, a purely theoretical issue. Nevertheless, it could also have an experimental relevance since all-to-all interacting systems can be realized using modern experimental techniques (8). Thus, it is important to find characteristic signatures of this threshold.

In this Chapter, we investigate the classical Hamiltonian dynamics of an anisotropic Heisenberg model, for which a finite number  $N$  of spins interact with all-to-all couplings. The aim is to establish the main physical effects associated with the non-ergodicity threshold with respect to a phase-transition appearing at a higher energy. The phase-transition is studied in the micro-canonical ensemble, applying a recently developed solution method of mean-field Hamiltonians based on large-deviation theory (9). These two transitions remain distinct in the thermodynamic limit. We focus on finite size systems, because they allow a precise study of the interplay between dynamics and statistics. Moreover, it has been remarked that, due to dynamical chaos, even systems with a small number of degrees of freedom can acquire a statistical behavior (11).

An interesting result presented in this Chapter is that the ferromagnetic/paramagnetic transition can be *dynamically driven* below the statistical phase-transition. This happens if the spin coupling strength is big enough to produce fully chaotic motion, indeed in this case we will show that even if most of the accessible states are magnetized, the magnetization in its dynamics oscillates between positive and negative values, thus giving a zero time average. This means that, for all finite  $N$ , an *observation time* exists for which the time average of the magnetization vanishes in an energy region above the non-ergodicity threshold, and below the statistical one. This is due to a chaotic driven reversal of the magnetization. Indeed above this threshold, in a fully chaotic regime, magnetization changes sign in a stochastic way and its behavior can be fully characterized by an average magnetization reversal time. In this Chapter we present the derivation of an explicit expression for the time scale of *magnetization reversal*. At the ergodicity threshold, the reversal time diverges as a power law, with a characteristic exponent proportional to the number of spins  $N$ .

Beside a regime of fully chaoticity, we will also show that, for low interaction strength, a quasi-integrable regime is possible where reversal times strongly depends on initial conditions.

In Sec(3.2) we derive the non-ergodicity threshold and the statistical threshold. In Sec(3.3) we analyse the time scale for magnetic reversal, and in Sec(3.4) we discuss the non-ergodicity threshold as the critical threshold of a “chaotic driven” phase transition. Finally in Sec(3.5) we show numerical evidence of the quasi-integrable regime that can characterize the behaviour of the system for small interaction strength.

## 3.2 The two Thresholds

The Hamiltonian of the model is

$$H = B \sum_{i=1}^N S_i^z + \frac{J}{2} \sum_{i=1}^N \sum_{j \neq i}^N (S_i^x S_j^x - S_i^y S_j^y), \quad (3.1)$$

where  $\mathbf{S}_i = (S_i^x, S_i^y, S_i^z)$  is the spin vector with continuous components,  $N$  is the number of spins,  $B$  is the rescaled external magnetic field strength and  $J$  the all-to-all coupling strength (the summation is extended over all pairs). Hamiltonian (6.3) is different from the Hamiltonian we considered in the previous Chapter. Indeed we added an external magnetic field to generalize our considerations.

The equations of motion are derived in a standard way from this Hamiltonian, and we have:

$$\begin{cases} \frac{dS_i^x}{dt} = -BS_i^y - JS_i^z \sum_{\langle j \rangle} S_j^y \\ \frac{dS_i^y}{dt} = BS_i^x - JS_i^z \sum_{\langle j \rangle} S_j^x \\ \frac{dS_i^z}{dt} = J \sum_{\langle j \rangle} (S_i^y S_j^x + S_i^x S_j^y) \end{cases} \quad (3.2)$$

The total energy  $E = H$  and the spin moduli  $|\mathbf{S}_i|^2 = 1$  are constants of the motion. The dynamics of this model was found to be characterized by chaotic motion (positive maximal Lyapunov exponent) for not too small energy values and spin coupling constants. For  $J = 0$  the model is exactly integrable, while for generic  $J$  and  $B$  there is a mixed phase space with prevalently chaotic motion for  $|E| < JN$ .

We will now show the existence of two distinct threshold in this model: first we will derive analytically the non-ergodicity threshold, then we will present the microcanonical analysis and the analytical evaluation of the statistical threshold, at which a second order phase transition occurs in the  $N \rightarrow \infty$  limit.

### 3.2.1 The non-ergodicity Threshold

The non-ergodicity energy density  $\epsilon_{ne}$  for the Hamiltonian (6.3) can be obtained in the same way as we did in the previous Chapter. Even in this case, it is possible to show (see Appendix A), that the phase space of the system is topologically disconnected below  $\epsilon_{ne}$ . From symmetry considerations both positive and negative regions of  $m_y$  exist on the same energy surface. Switching from a negative  $m_y$  value to a positive one requires, for continuity, to pass through  $m_y = 0$ . Hence, for all energy values above  $\epsilon_{ne} = \min(\epsilon|m_y = 0)$  magnetization reversal is possible, while below this value magnetization cannot change sign. Computing the minimum, we get (14),

$$\epsilon_{ne} = \begin{cases} -B \text{ for } J \leq B \\ -(\frac{B^2}{2J} + \frac{J}{2}) \text{ for } J > B. \end{cases} \quad (3.3)$$

The existence of  $\epsilon_{ne}$  does not represent a sufficient condition in order to demagnetize a sample for  $\epsilon > \epsilon_{ne}$ . As will be shown in Sec.(3.5), regular structures indeed appear that prevent most of trajectories to cross the  $m_y = 0$  plane.

### 3.2.2 The statistical Threshold

We will first determine the statistical phase-transition energy of the model in the microcanonical ensemble. The Hamiltonian can be rewritten as

$$H = BNm_z + \frac{J}{2}N^2 (m_x^2 - m_y^2) + \frac{J}{2} \sum_i (S_i^y)^2 - (S_i^x)^2, \quad (3.4)$$

where  $\mathbf{m} = (m_x, m_y, m_z) = 1/N \sum_i \mathbf{S}_i$ . To keep the calculations easy, we will first neglect the term  $J/2 \sum_i (S_i^y)^2 - (S_i^x)^2$ . We will show later how to take into account this term. In order to facilitate the calculations we will also set,

$$\begin{aligned} \epsilon &\rightarrow \epsilon/B \\ I &\rightarrow \frac{JN}{B}, \end{aligned} \quad (3.5)$$

and we will consider the case  $B = 0$  later. Thus we can consider the following Mean-Field Hamiltonian:

$$H = N \left[ m_z + \frac{I}{2} (m_x^2 - m_y^2) \right], \quad (3.6)$$

The most remarkable difference of Hamiltonian (3.6) with respect to (6.3) is that a new constant of the motion appears: the modulus of the total angular momentum  $M^2 = m_x^2 + m_y^2 + m_z^2$ . In numerical simulations we always find a vanishing Lyapunov exponent: hence, we presume that model (3.6) becomes exactly integrable. The dynamics of the global magnetization is indeed integrable, but this does not obviously imply the integrability of Hamiltonian (3.6), in the same way that the integrability of the center of mass does not imply the integrability of the motion of all the particles. It is not difficult to show that the motion of the magnetization must be integrable for Hamiltonian (3.6): the phase space is three dimensional, but the two constant of motion  $H$  and  $M^2$  forces the magnetization vector to move in a one dimensional phase space, which proves integrability.

Using this simplified Hamiltonian, we can calculate the entropy, counting the number of microscopic configurations associated with given values of  $m_x$ ,  $m_y$  and  $m_z$ , independently of the energy of the system. This can be done using the Cramér theorem, a basic tool of Large Deviation theory (10). Each single spin is characterized by two angles  $\theta$  and  $\phi$ , such that  $S_z = \cos \theta$ ,  $S_x = \sin \theta \cos \phi$ ,  $S_y = \sin \theta \sin \phi$ . We calculate the function

$$\Psi(\lambda_x, \lambda_y, \lambda) = \frac{1}{4\pi} \int_0^\pi \sin \theta \, d\theta \int_0^{2\pi} d\phi e^{\lambda \cos \theta} e^{\lambda_x \sin \theta \cos \phi + \lambda_y \sin \theta \sin \phi}. \quad (3.7)$$

Then, from Cramér's theorem, we get the entropy  $s(m_x, m_y, m_z)$  through a Legendre-Fenchel transform of  $\ln \Psi$ :

$$s(m_x, m_y, m_z) = \sup_{\lambda_x, \lambda_y, \lambda} [\lambda_x m_x + \lambda_y m_y + \lambda m_z - \ln \Psi(\lambda_x, \lambda_y, \lambda)]. \quad (3.8)$$

The equilibrium state is now computed by maximizing the entropy (3.8), under the constraint of a constant energy. Of course, for small  $N$ , there will be large fluctuations around this equilibrium value, we turn to this point later. Our goal is now just to locate the statistical phase transition  $\epsilon_{stat}$ . We will simplify the problem somewhat. As we are interested in finding a possible phase transition between a  $m_y = 0$  and an  $m_y \neq 0$  states, and assuming the transition is second order, it is sufficient to study the entropy around  $m_y = 0$ . We will also set  $m_x = 0$ , since it is easy to see that any non-zero  $m_x$  would only decrease the entropy for negative energy states. Physically, the picture is the following: the negative energy has to be absorbed by either a non-zero  $m_z$ , or a non-zero  $m_y$  or both. For small negative energies, it is entropically favorable to decrease a bit  $m_z$ , since it has a linear effect on the energy. For negative enough energies however, it costs much entropy to decrease  $m_z$  further (formally,  $m_z = -1$  corresponds to a  $-\infty$  entropy); a non-zero  $m_y$  is then favored, this is the phase transition. We thus develop  $\Psi$  up to second order in terms of  $\lambda_y$ , and compute the entropy  $s(m_x = 0, m_y, m_z)$  up to second

order in  $m_y$ . Using the energy conservation  $m_z = \epsilon + Im_y^2/2$ , we obtain the entropy  $s(m_y; \epsilon)$  as a function of  $m_y$  alone,  $\epsilon$  being now a parameter. The vanishing of the second derivative in  $m_y = 0$  yields the critical energy:  $\epsilon_{stat} = -1/I$ , which, from Eq.(3.5), in the old variables becomes:

$$\epsilon_{stat} = -\frac{B^2}{JN}. \quad (3.9)$$

At this threshold the entropy has a maximum in  $m_y = 0$ , indicating the the probability distribution of the magnetization becomes sigle peaked, instead of double peaked, for  $\epsilon > \epsilon_{stat}$ . It can be shown (13) that in the thermodynamic limit the second derivative of the entropy becomes discontinuous in  $\epsilon_{stat}$ , indicating that a second order phase transition occurs at  $\epsilon_{stat}$ , for  $N \rightarrow \infty$ . This value of  $\epsilon_{stat}$ , analytically obtained, is in good agreement with numerical results obtained using the full Hamiltonian (6.3).

For finite  $N$ , the system is actually best described by a probability distribution  $P(m_x, m_y)$  for each energy. The previous calculation gives us an approximate expression for this probability:

$$P(m_x, m_y) \propto \exp \left( Ns(m_x, m_y, m_z = e - \frac{I}{2}(m_x^2 - m_y^2)) \right). \quad (3.10)$$

The paramagnetic (resp. ferromagnetic) phase then corresponds to a probability distribution single (resp. double) peaked around  $m_y = 0$ .

Neglecting the fluctuations for  $m_x$ , the probability distribution for  $m_y$  at a given energy density  $\epsilon$  is:

$$P(m_y, \epsilon) \propto e^{Ns(m_y, \epsilon)}, \quad (3.11)$$

where

$$s(m_y, \epsilon) = -\frac{m_y^2}{2\phi(\lambda)} - \lambda \left( \epsilon + \frac{I}{2}m_y^2 \right) + \ln \left( \frac{\sinh \lambda}{\lambda} \right) \quad (3.12)$$

and

$$\phi(\lambda) = \frac{\lambda \cosh \lambda - \sinh \lambda}{\lambda^2 \sinh \lambda} \quad (3.13)$$

with  $\lambda$  defined implicitly from the equation

$$\epsilon + \frac{I}{2}m_y^2 = \lambda\phi(\lambda) \quad (3.14)$$

From Eqs.(3.12,3.13,3.14) we can get the most probable value  $m_y^*(\epsilon)$ , we will compare in Sec.(3.4), the most probable value of  $m_y$  thus obtained with the one obtained dynamically.

In this scheme, the non-ergodicity threshold  $\epsilon_{ne}$  can be recovered as the energy such that  $s(0, \epsilon_{ne}) = -\infty$ . From Eqs.(3.12,3.14) with  $m_y = 0$ , it is easy to get  $\epsilon_{ne} = -1$ , that using Eq.(3.5) implies  $\epsilon_{ne} = -B$ , which is the same as in Eq.(6.13) in the limit  $N \rightarrow \infty$ .

Also the minimal energy can be easily estimated (see Appendix B) as

$$\epsilon_{min} = \begin{cases} -\frac{B^2}{2JN} - \frac{JN}{2} & \text{for } J \geq \frac{B}{N} \\ -B & \text{for } J < \frac{B}{N} \end{cases} \quad (3.15)$$

The statistical analysis has been done so far neglecting the term  $J/2 \sum_i (S_i^y)^2 - (S_i^x)^2$  in the Hamiltonian (3.4). The results are qualitatively correct; to have a better agreement for small  $N$ , this term should be included. This can be done in the following way. The Hamiltonian

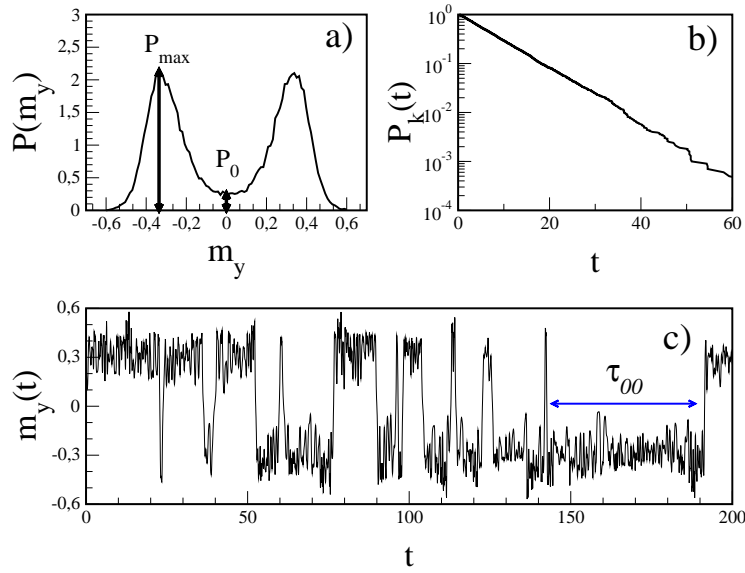


Figure 3.1: a) Probability distribution of  $m_y$  for  $\epsilon = -0.9$ . The maximal probability,  $P_{max}$ , and  $P_0 = P(m_y = 0)$  are indicated by vertical arrows. b) Probability of keeping magnetization sign up to time  $t$  vs time. c) Magnetization  $m_y$  vs time. In this figure all data refer to the  $N = 6$ ,  $B = 1$ ,  $J = 3$  case.

depends now on another global quantity,  $\Delta = \langle (S_i^x)^2 - (S_i^y)^2 \rangle$ . It is possible to include it in the large deviation calculation; Eq.3.7 is modified in:

$$\tilde{\Psi}(\lambda_x, \lambda_y, \lambda, \mu) = \frac{1}{4\pi} \int_0^\pi \sin \theta d\theta \int_0^{2\pi} d\phi e^{\lambda \cos \theta + \lambda_x \sin \theta \cos \phi + \lambda_y \sin \theta \sin \phi + \mu \sin^2 \theta (\cos^2 \phi - \sin^2 \phi)} \quad (3.16)$$

One proceeds with the maximization procedure to compute  $s(m_x, m_y, m_z, \Delta)$ .  $P(m_y, \epsilon)$  is then obtained maximizing  $s$  over the variables  $m_x, m_z, \Delta$  at fixed energy. This last step has to be carried out numerically, and no simple expression as (3.9) is available any more.

Finally note that, for the case  $B = 0$ ,  $\epsilon_{stat}$ , obtained from direct numerical computation of the specific energy for which the probability distribution becomes single peaked, is consistent with Eq.(3.9) with  $B = 0$ .

### 3.3 Time Scale for Magnetic Reversal

In the following, we will study the dynamics of the full Hamiltonian (6.3), which, at variance with (3.4), is non-integrable and displays chaotic motion. Moreover, we will restrict ourselves to the case  $J > B/N$  for which  $\epsilon_{stat} > \epsilon_{ne} > \epsilon_{min}$ . The two thresholds,  $\epsilon_{ne}$  and  $\epsilon_{stat}$ , define three energy regions which show different dynamical and statistical properties:

1) For  $\epsilon < \epsilon_{ne}$ , the probability distribution of  $m_y$ ,  $P(m_y)$ , obtained by a random sampling of constant energy surface (16), as explained in Chapter(2), Sec.(2.3), shows two separate peaks, with  $P(m_y = 0) = 0$ , so that  $m_y$  cannot change sign in time.

2) For  $\epsilon_{ne} < \epsilon < \epsilon_{stat}$ , the probability distribution is double peaked around the most probable values of the magnetization. These two peaks are not separated and  $P(m_y = 0) \neq 0$ , see Fig. (3.1a). What actually happens dynamically depends on the relative strength of the coupling  $J$  with respect to  $B$ . For  $J$  big enough the behaviour of  $m_y(t)$  resembles a random telegraph

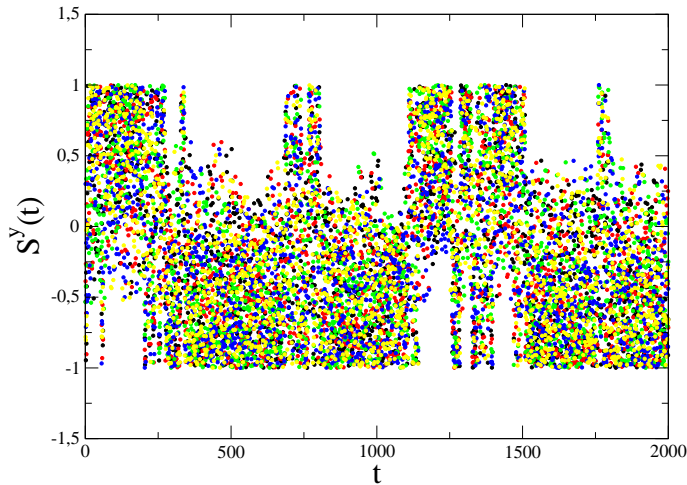


Figure 3.2: With different colors we show the time dependence of the  $y$  component of each spin for a system of 5 spins with  $B = J = 1$  and  $\epsilon = -0.8$ . The collective behaviour of all the spins in correspondence to the sign reversal of  $S_i^y$  is clearly visible.

noise (17), Fig.(3.1c): magnetization switches randomly between its two most probable values, reversing its sign at random times. We note here that in correspondence of the magnetic reversal of the magnetization we found a collective behaviour: all the spins of the system reverse the sign of the  $y$  component almost at the same time, see Fig.(3.2). This behavior has been found to be common when the change of the magnetization is large enough, for instance if the magnetization changes from  $-0.9$  to  $+0.9$ . Indeed in this case only a collective behaviour of all the spins can induce such a big change in the magnetization.

We computed the reversal times in two different ways:

- a) Starting from a single initial condition, on a given energy surface, and integrating the equations of motion for a long time interval. We then sampled the time needed for the magnetization to cross zero twice,  $\tau_{00}$ , see Fig.(3.1 c).
- b) Starting from an ensemble of initial conditions on a given energy surface. We computed, for each initial condition, the time needed for the magnetization to cross zero:  $\tau_{first}$ .

In a fully chaotic regime the Probability distribution of the reversal times computed in the two different ways,  $P(\tau_{00})$  and  $P(\tau_{first})$ , turn out to be the same: the probability distribution of magnetization reversal times follows a Poissonian law. Hence, we can characterize the behavior of the system through an average magnetization reversal time  $\tau$ . The Poissonian distribution of the reversal times is a consequence of strong chaos: the system loses its memory due to sensitivity to initial conditions and the reversal probability per unit time becomes time independent. As a consequence of the Poissonian distribution of the reversal times we have that the probability for the magnetization to keep its sign up to time  $t$  decays exponentially with  $t$ :  $P_k(t) \sim e^{-t/\tau}$ , see Fig. (3.1b), for any initial conditions.

On the contrary, for small  $J$ , we observe a quasi-integrable behavior almost everywhere in the energy range: reversal times strongly depend on initial conditions. We will show the behaviour of the magnetization in this regime in Sec(3.5). For the moment we will limit our considerations to the large  $J$  case.

3) Finally, for  $\epsilon_{stat} \leq \epsilon \leq 0$ ,  $m_y$  quickly changes sign and  $P(m_y)$  is peaked at  $m_y = 0$ .

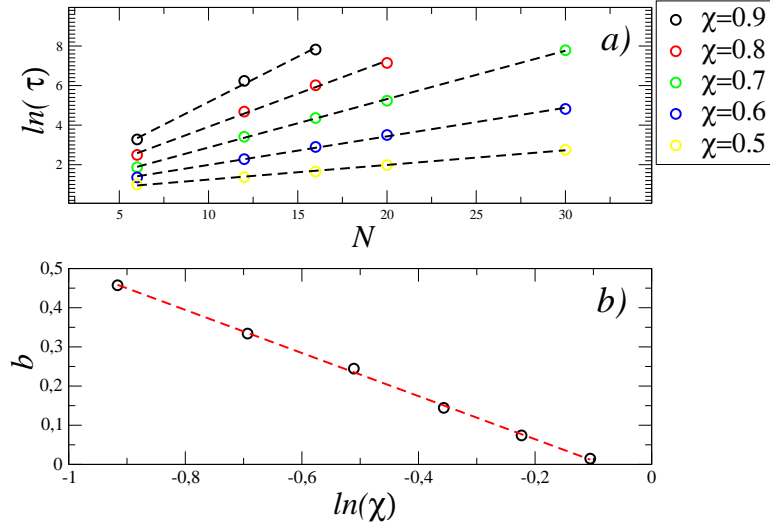


Figure 3.3: In Fig. a) we show the average magnetization reversal time  $\tau$  vs.  $N$  for different  $\chi$  and for  $B = J = 1$ . The exponential growth of  $\tau$  (circles) with the number of particles is evident. As dashed black line we show the linear fit  $\ln(\tau) = a + bN$ . In Fig. b) we show the slopes,  $b$  (circles), of this fitting formula vs.  $\ln(\chi)$ . From the linear fit (dashed red line) we have:  $b = -0.55\ln(\chi)$ . The linear fit shows that  $\tau$  has a power law dependence on  $\chi$ .

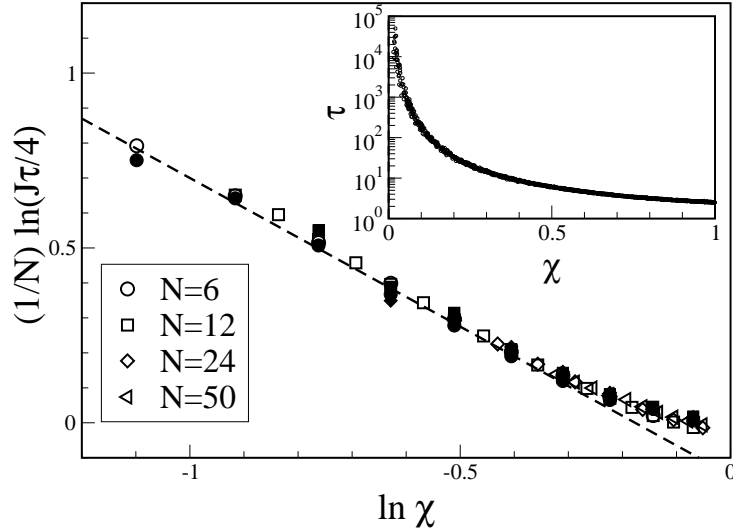


Figure 3.4: Average magnetization reversal times  $\tau$  obtained dynamically (open symbols) and statistically (full symbols), vs the energy scaling parameter  $\chi = (\epsilon - \epsilon_{ne}) / (\epsilon_{stat} - \epsilon_{ne})$  for different  $N$  values and  $B = 0$ . The dynamical determination of  $\tau$  has been obtained by iterating  $10^4$  randomly chosen trajectories for each energy and computing the average reversal time explicitly. The statistical determination of  $\tau$  is obtained from formula (3.20), where  $P_{max}/P_0$  is numerically determined for each energy density. The dashed line is  $\ln(J\tau/4) = -0.15 - 0.85\ln \chi$ , where the constants have been obtained through a fitting. Inset : divergence of  $\tau$  at  $\chi = 0$  for  $N = 5$  and  $J = B = 1$ .

For all energies in the range  $(\epsilon_{ne}, \epsilon_{stat})$ , we analyzed the average reversal time. We find that the reversal time  $\tau$  grows exponentially with the number of spins for sufficiently large  $N$ , see Fig.(3.3). We derive empirically an explicit formula for the dependence of  $\tau$  on the parameter  $\chi = (\epsilon - \epsilon_{ne})/(\epsilon_{stat} - \epsilon_{ne})$

$$\tau \sim \chi^{-\alpha N}. \quad (3.17)$$

Eq. (3.17) is valid above the non-ergodicity threshold and not too close to the statistical border (observe that  $\chi$  varies in this range between 0 and 1). The comparison of this formula with numerical results is shown in Fig.(3.3 and 3.4). Let us remark that the reversal time diverges at  $\epsilon_{ne}$ , see the inset of Fig.(3.4), as a power law, showing that this energy threshold shares many peculiarities with standard second order phase transitions. In the case  $B = 0$ , we find  $\alpha = 0.85$ , Fig.(3.4), which is at variance with the value  $\alpha = 1$  obtained, for  $N \rightarrow \infty$ , in the mean field approximation (see below). This small discrepancy can be attributed to a finite  $N$  effect. Extensions of these results to the  $B \neq 0$  case show additional dependences of  $\alpha$  on the parameters  $B$  and  $J$ : when  $J = B$  one has  $\alpha \approx 1/2$ , see Fig.(3.3), while for  $J \gg B$ ,  $\alpha$  has the same value as for  $B = 0$ .

A justification of Eq. (3.17) can also be given in terms of statistical properties. In Refs. (6; 7), on the basis of fluctuation theory (20; 5), it has been argued that metastable states relax to the most probable state on times proportional to  $\exp(N\Delta s)$  where  $N$  is the number of degrees of freedom and  $\Delta s$  is the specific entropic barrier. In our case  $\exp(N\Delta s)$  is nothing but  $P_{max}/P_0$ , see Fig. (3.1a).

From the statistical approach presented in Sec(3.2.2) it is possible to determine the dependence of  $P_{max}/P_0$  on the parameters of the system in the Mean-Field model, Eq.(3.6), and for  $N \rightarrow \infty$ .

Below the statistical specific energy,  $P(m_y)$  is doubly peaked with a minimum in  $m_y = 0$ ; the entropic barrier per particle is thus  $s(m_y^*) - s(m_y = 0)$ , where  $m_y^*$  is the most probable value of  $m_y$  on the considered energy surface. A rough estimate of the switching time between  $m_y^*$  and  $-m_y^*$  can be given, following Ref. (5), by

$$\tau(N, \epsilon) \sim \exp\left(N(s(m_y^*) - s(m_y = 0))\right). \quad (3.18)$$

There ought to be some prefactor, of course: we will discuss this point here below. Anyway the wild exponential dependence in  $N$  is the most prominent phenomenon, as is evident from the comparison with the numerics, see Fig.(3.3 and 3.4). Using Eq.(3.18), it is possible to show, see Appendix C, that  $\tau(N, \epsilon)$  diverges at the critical point  $\epsilon_{ne}$  with a power law depending on  $N$  only, namely

$$\tau \sim 1/(\epsilon - \epsilon_{ne})^N \quad (3.19)$$

Note that Eq.(3.19) reproduces the main features of Eq. (3.17) and gives  $\alpha = 1$ . Note that the same calculations can be made for  $B = 0$ , considering the full Hamiltonian(3.4), and we have that  $\alpha = 1$  also in this case.

We also analysed numerically the relation between the reversal times and  $P_{max}/P_0$ . Empirically, for  $B = 0$ , we find a very good agreement with the reversal times setting

$$\tau = \frac{4}{J} \frac{P_{max}}{P_0}. \quad (3.20)$$

While the  $P_{max}/P_0$  factor in this formula has a theoretical justification, because it represents the probability to cross the entropic barrier, the  $1/J$  factor can be heuristically associated with the typical time scale of the system. A deeper theoretical justification of this formula should

be obtained in view of its success in describing the numerical results for different  $N$ , values (Fig.(3.4)).

Because the reversal of the magnetic moment is a stochastic process, as we showed in this section, we can consider  $1/\tau$  the escape rate of the magnetization through the entropic barrier  $N\Delta s = \Delta S$ . If we call  $\lambda$  the escape rate we can thus write, from Eq.(3.20):

$$\lambda = \omega_0 e^{\Delta S} \quad (3.21)$$

From Eq.(3.20) we have  $\omega_0 = J/4$  and all the dependence on  $N$  is contained in the entropic barrier term.

It is now interesting to compare Eq.(3.21) with the escape rate of the Kramers Model, see Ref.(21) and references therein.

In the Kramers Model a classical particle, with mass  $M$ , moves in a one dimensional asymmetric double well potential. The system is supposed to be in contact with an heat bath at temperature  $T = 1/(k\beta)$ . The action of the heat bath on the dynamics of the system is taken into account through a fluctuating random force, and a damping term  $-M\gamma\dot{x}$ . The escape rate from one well can be written as:

$$\lambda_k = c\omega_0 e^{-\beta\Delta E} \quad (3.22)$$

where  $\Delta E$  is the energy barrier,  $\omega_0$  is the frequency of the motion at the bottom of the potential well (obtained expanding the potential up to second order in the position coordinate), and  $c$  depends both on the damping rate  $\gamma$  and on the frequency of the motion at the top of the potential well.

The similarity between Eq.(3.21) and Eq.(3.22) is self-evident. We can then make the following consideration: In the Kramers Model the escape mechanism is due to the external noise, while in our case is due to the internal noise (chaos).

### 3.4 Chaotic Driven Phase Transition

In this section we will answer the following question: if the measured value of the magnetization are given by the time average of the magnetization, for which energies the system will be found magnetized and for which unmagnetized?

From Eq. (3.17) it is clear that the infinite time average of the magnetization is zero above the non-ergodicity threshold and different from zero below, due to the divergence of the reversal time. Nevertheless, this is not what we obtain during a finite observational time  $\tau_{obs}$ . In Fig.(3.5) we show the time-averaged magnetization

$$\langle m_y \rangle_{obs} = (1/\tau_{obs}) \int_0^{\tau_{obs}} dt m_y(t)$$

vs the specific energy  $\epsilon$  for  $N = 5$  (Fig.3.5a) and  $N = 50$  (Fig.3.5b) spins during a fixed observational time. While in (a)  $\langle m_y \rangle_{obs}$  is zero just above  $\epsilon_{ne}$ , in (b) it vanishes at a value  $\epsilon_{obs}$  located between  $\epsilon_{ne}$  and  $\epsilon_{stat}$ . Indeed, if  $\tau_{obs} \gg \tau$ , the magnetization has time to flip between the two opposite states and, as a consequence,  $\langle m_y \rangle_{obs} \simeq 0$ . On the contrary, if  $\tau_{obs} \ll \tau$  the magnetization keeps its sign and cannot vanish during  $\tau_{obs}$ . Defining an effective transition energy  $\epsilon_{obs}$  from  $\tau_{obs} = \tau(\epsilon_{obs})$ , one gets, inverting Eq. (3.17), the value indicated by the vertical arrow in Fig. (3.5b). This is, *a posteriori*, a further demonstration of the validity of Eq. (3.17) for any  $N$ .

From Eqs.(3.12,3.13,3.14) we can get the most probable value of the magnetization,  $m_y^*(\epsilon)$ . A plot of  $m_y^*(\epsilon)$ , is given in Fig.(3.5a,b) as dashed lines. As one can see, the agreement with the numerical results obtained from the full Hamiltonian is excellent in the ferromagnetic phase.

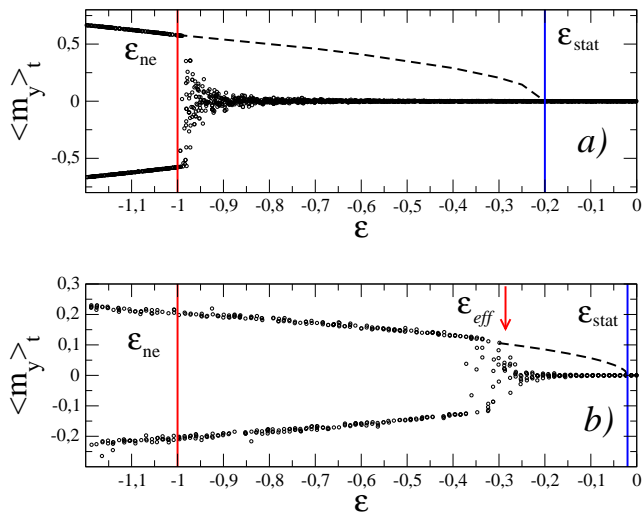


Figure 3.5: Time average of  $m_y$  over the observational time  $\tau_{obs}$  vs  $\epsilon$  for different number of particles (a)  $N = 5$ , (b)  $N = 50$ , with fixed  $J = B = 1$ . Each single point has been obtained taking the time average over the time intervals  $\tau_{obs} = 10^5$  (a) and  $\tau_{obs} = 10^4$  (b). Dashed curves indicate the equilibrium value of  $m_y$  obtained from statistical mechanics. Vertical lines represent the non-ergodicity and the statistical threshold respectively. The arrow in (b) indicates the energy value  $\epsilon_{obs}$  of the dynamical transition due to the finite observational time.

From a theoretical point of view, it is interesting to note that, for any fixed  $N$ , and sufficiently large  $J$ ,  $\epsilon_{obs} \rightarrow \epsilon_{ne}$  when  $\tau_{obs} \rightarrow \infty$ . On the other side, in agreement with statistical mechanics, for any finite  $\tau_{obs}$ ,  $\epsilon_{obs} \rightarrow \epsilon_{stat}$  when  $N \rightarrow \infty$ . This implies that the limits  $\tau_{obs} \rightarrow \infty$  and  $N \rightarrow \infty$  do not commute.

From the above considerations it follows that if  $\tau_{obs} \rightarrow \infty$ , the threshold which distinguishes between a magnetized energy region and an unmagnetized one is  $\epsilon_{ne}$  and not  $\epsilon_{stat}$ . We can thus consider  $\epsilon_{ne}$  as the critical threshold at which a “dynamical” phase transition takes place: we call this transition a *chaotic driven phase transition*.

Let us finally note that, usually, for long-range interactions, the interaction strength is rescaled in order to keep an extensive energy(19). In our case this can be done setting  $J = I/N$ . With this choice of  $J$  as  $N \rightarrow \infty$ , at fixed  $I$ ,  $J$  becomes much smaller than  $B$ , then a quasi-integrable regime sets in and Eq. (3.17) loses its validity, see Sec(3.5). The presence of the non-ergodicity threshold is therefore hidden.

### 3.5 Quasi-integrable Regime

In this section we will give numerical evidence of the quasi-integrable regime we can find for  $J < B$  in the energy region between  $\epsilon_{ne}$  and  $\epsilon_{stat}$ . If the system dynamics is not in a fully chaotic regime, there are important consequences with respect to the reversal times and escape rates (for instance Eq(3.17) loses validity).

Perhaps the most striking example has been reported in Fig.(3.6). We consider here a system with  $N = 6$  spins and  $B = 1$ , and different interaction strength,  $J = 0.5$ , Fig.(3.6) a) and b) and  $J = 1$ , Fig.(3.6) c) and d). The energy in the two cases has been chosen so that the entropic barrier is roughly the same, see Fig.(3.6) b) and d): this means that from a statistical point of view both systems are characterized by the same probability to jump the barrier. Nevertheless, as one can see in a) and b), the probability to keep the sign of the magnetization differs by

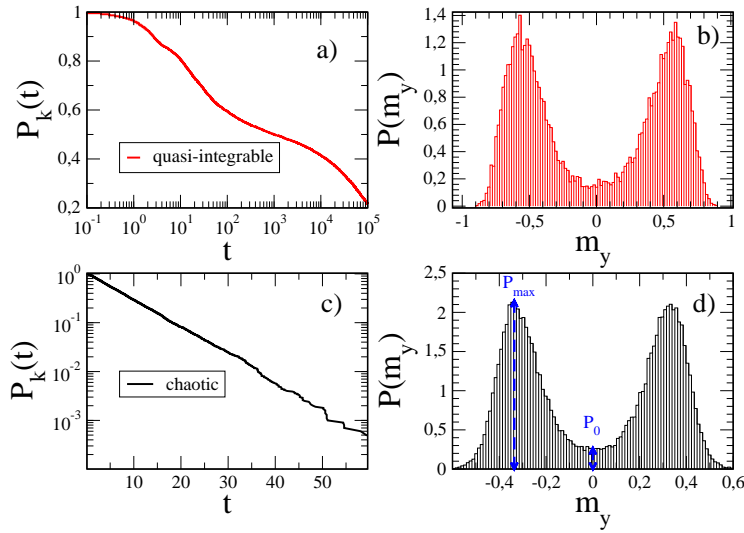


Figure 3.6: The case  $N = 6$   $B = 1$  is considered. We consider two different cases:  $J = 0.5$  and  $\epsilon = -0.8$ , Fig. a) and b), for which the system displays a quasi-integrable regime, and  $J = 1$   $\epsilon = -0.9$ , Fig. c) and d), for which the system displays a fully chaotic regime. The specific energies have been chosen in such a way that  $P_{max}/P_0$  are almost the same for the two cases, see Fig. b) and d). We compare the probability to keep the sign of the magnetization up to time  $t$ ,  $P_k(t)$ , for the two different dynamical regime: in the fully chaotic regime, Fig.c),  $P_k(t)$  decays exponentially with  $t$  and the average magnetization time is of order 10. While in the quasi-integrable regime, the dependence of  $P_k(t)$  on  $t$  is far from exponential and after a time of order  $10^5$ ,  $P_k(t)$  is still large.

many orders of magnitude. This cannot be explained from the different  $J$  value, that, as we have shown in the previous section, has only a linear effect on the reversal probability per unit time. Such a big difference in the reversal times can be explained only with a drastic change of the dynamical properties of the system: indeed while Fig.(3.6 a) refers to a quasi-integrable regime, Fig.(3.6 b) refers to a fully chaotic regime. Quasi-integrability, or at least a lack of ergodicity, has been also supported by different phase-space and time average of the magnetization, see Fig.(3.7 a). While they agree in the fully chaotic regime, Fig.(3.7 b), in the quasi-integrable regime, Fig.(3.7 a), the time average strongly depend on the initial conditions.

To assess the origin of this quasi-integrable regime in many-body systems is not an easy task. Anyway we want to address a characteristic feature of this regime shared by standard KAM systems.

In order to explain this point let us compare the dynamics obtained from the full Hamiltonian(3.4) with the dynamics obtained from the Mean-Field Model,

$$H = BNm_z + \frac{J}{2}N^2 (m_x^2 - m_y^2). \quad (3.23)$$

In Fig.(3.8) we show the projection of the trajectory of  $\mathbf{m}$  on the  $xy$  plane, namely we show  $m_y(t)$  versus  $m_x(t)$ . We considered the different dynamical regimes described above. To fix the idea we consider different interaction strength and the same scaling parameter  $\chi = \chi(\epsilon) = 0.663$  (therefore  $\epsilon > \epsilon_{ne}$  for the two cases). We recall here that what we called magnetization in this Chapter is  $m_y$  because the  $y$  direction is the easy axis of the magnetization of our system.

Let us first discuss Fig.(3.8a). Dark lines represent orbits of the Mean-Field Hamiltonian. The orbits of the macroscopic variable  $\mathbf{m} = (m_x, m_y, m_z)$  cover KAM tori since the Mean-Field

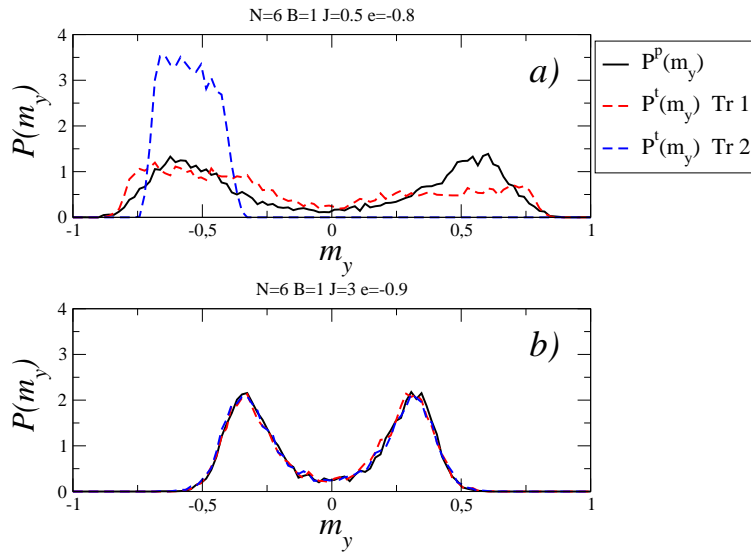


Figure 3.7: In Fig. *a*) the case  $N = 6$ ,  $B = 1$ ,  $J = 0.5$  and  $\epsilon = -0.8$  is considered. We compare the probability distribution of the magnetization,  $P^p(m_y)$ , obtained from phase space average, (continuum black lines), with  $P^t(m_y)$  obtained from the time average of two different trajectories (dashed lines). The system clearly shows a non-ergodic behaviour, within the considered integration time ( $10^4$ ). In Fig. *b*) the case  $N = 6$ ,  $B = 1$ ,  $J = 1$  and  $\epsilon = -0.9$  is considered. Note that  $P^p(m_y)$  and  $P^t(m_y)$  obtained from two different trajectories agrees within the considered integration time ( $10^4$ ). Note finally that the entropic barriers are the same for the two cases.

Model in the macroscopic variable  $\mathbf{m}$  is exactly integrable (as discussed in Sec.(3.2.2)  $m^2$  is another constant of motion for the Mean-Field Model). Despite the complete integrability the trajectories display different features: while (1) cross the line  $m_y = 0$ , (2) remains confined in the negative ( $m_y < 0$ ) branch (let us stress that the trajectories belong to the same energy surface). This means that the property to cross the  $m_y = 0$  line can also occur for a completely integrable case.

Two trajectories of the full Hamiltonian and the same initial conditions are then considered, (3) and (4). As one can see the orbits stay for a long time sufficiently close to the Mean-Field orbits. Again, while (4) gives rise to a “ferromagnetic” behavior, (3) originates a “paramagnetic” one. Both trajectories, (3) and (4), are characterized by a positive maximal Lyapunov exponent, so, according to common terminology, they are both chaotic, nevertheless the latter, (3), demagnetizes, while the former, (4), does not. On increasing  $J$ , keeping the same value of  $\chi$ , we enter in the regime described by Fig.(3.8b). Here, in the same way an orbit of the Mean-Field Model has been indicated, (5) (actually a “ferromagnetic” one). The orbit of the full Hamiltonian, (6), still characterized by a maximal Lyapunov exponent, covers both branches,  $m_y > 0$  and  $m_y < 0$ , thus inducing the demagnetization of the system. What is important to stress is that in this case all the trajectories of the full Hamiltonian cover both the branches on the same energy surface. Having in mind the mechanism producing a transition to the global stochasticity in the Standard Map, with the breakdown of the last golden curve, we can thus conjecture that invariant curves, confining the motion, exist in case (a), above the non-ergodicity threshold in some region of the energy surface. The breakdown of this last invariant curve, signals the transition to a fully chaotic motion. Of course, finding such threshold is an hard task, due to the high-multidimensionality of the problem (and to the related problems,

such as Arnold diffusion among tori(22)). The question about in which parameter region one expect to find a quasi-integrable regime and in which a fully chaotic one is still open. We can only make few qualitative considerations, reported below. Let us consider Hamiltonian (3.4), it represents a sum of two terms: a Mean-Field integrable term plus the term  $J/2 \sum_i (S_i^y)^2 - (S_i^x)^2$ , which is responsible for the chaoticity of the system. The specific minimal energy of this term is  $\sim -J/2$ , we will call it  $\epsilon_{ch}$  in the following. We can thus suppose that for  $\epsilon < \epsilon_{ch}$  the quasi-integrable regime prevails, while for  $\epsilon > \epsilon_{ch}$  a fully chaotic regime is possible. Thus in order to have a fully chaotic regime in the energy region between  $\epsilon_{ne}$  and  $\epsilon_{stat}$ , it is necessary that  $\epsilon_{ne} > \epsilon_{ch}$ . Now this is always the case if  $J > 2B$ , indeed for these values of  $J$   $\epsilon_{ne} \sim \epsilon_{ch}$ . While for  $J < 2B$  we expect a quasi integrable regime between  $\epsilon_{ne}$  and  $\epsilon_{ch}$ , which could persist in the thermodynamical limit. Our first numerical experiments do not falsificate this argument, but more analysis is needed in order to confirm it, or to find a better one.

### 3.6 Conclusions

Summarizing, a simple spin model with anisotropic and long-range couplings has been studied as a paradigmatic example. We discuss the relevance of the ergodicity breaking (3; 2) occurring for any finite  $N$  with respect to the phase-transition. Two distinct energy thresholds are addressed: the non-ergodicity threshold,  $\epsilon_{ne}$ , below which phase space is disconnected and magnetization cannot change sign in time, and the statistical threshold,  $\epsilon_{stat}$ , at which a second order phase-transition occurs in the thermodynamic limit. The non-ergodicity threshold does not disappear in the thermodynamic limit and remains always distinct from the statistical threshold. In the highly chaotic regime, between  $\epsilon_{ne}$  and  $\epsilon_{stat}$ , the behavior of the system can be characterized by an average magnetization reversal time  $\tau$ . Numerical simulations and statistical arguments allow us to give a characterization of the reversal time above the non-ergodicity threshold, pointing out a power law divergence at  $\epsilon_{ne}$ . This behavior is likely to be valid beyond the toy model studied in this Letter and could be a characteristic signature of the non-ergodicity threshold. The dynamical magnetization reversal times are also found to be in good agreement with those obtained from simple fluctuation theory arguments. The infinite-time average of the magnetization is zero above the non-ergodicity threshold, and different from zero below. Therefore, the system, when chaotic, dynamically demagnetizes well below the statistical threshold. This is the reason why we consider the non-ergodicity threshold as a chaotic driven phase transition.

We also gave numerical evidence that besides a fully chaotic regime, between  $\epsilon_{ne}$  and  $\epsilon_{stat}$ , a quasi-integrable regime is also possible. This can occur if the interaction strength, ( $J$ ), is smaller than the intensity of the external magnetic field, ( $B$ ). Also in this regime the magnetization can reverse its sign but the reversal times turn out to be strongly dependent on the initial conditions. Finally a possible mechanism for which the dynamics becomes quasi-integrable has been addressed, indeed we showed that the motion of the magnetization remains confined for a long time around the orbits of the Mean-Field Hamiltonian, in the quasi-integrable regime. We expect that this confinement persists in the thermodynamical limit, but more research is needed in order to confirm this expectation.

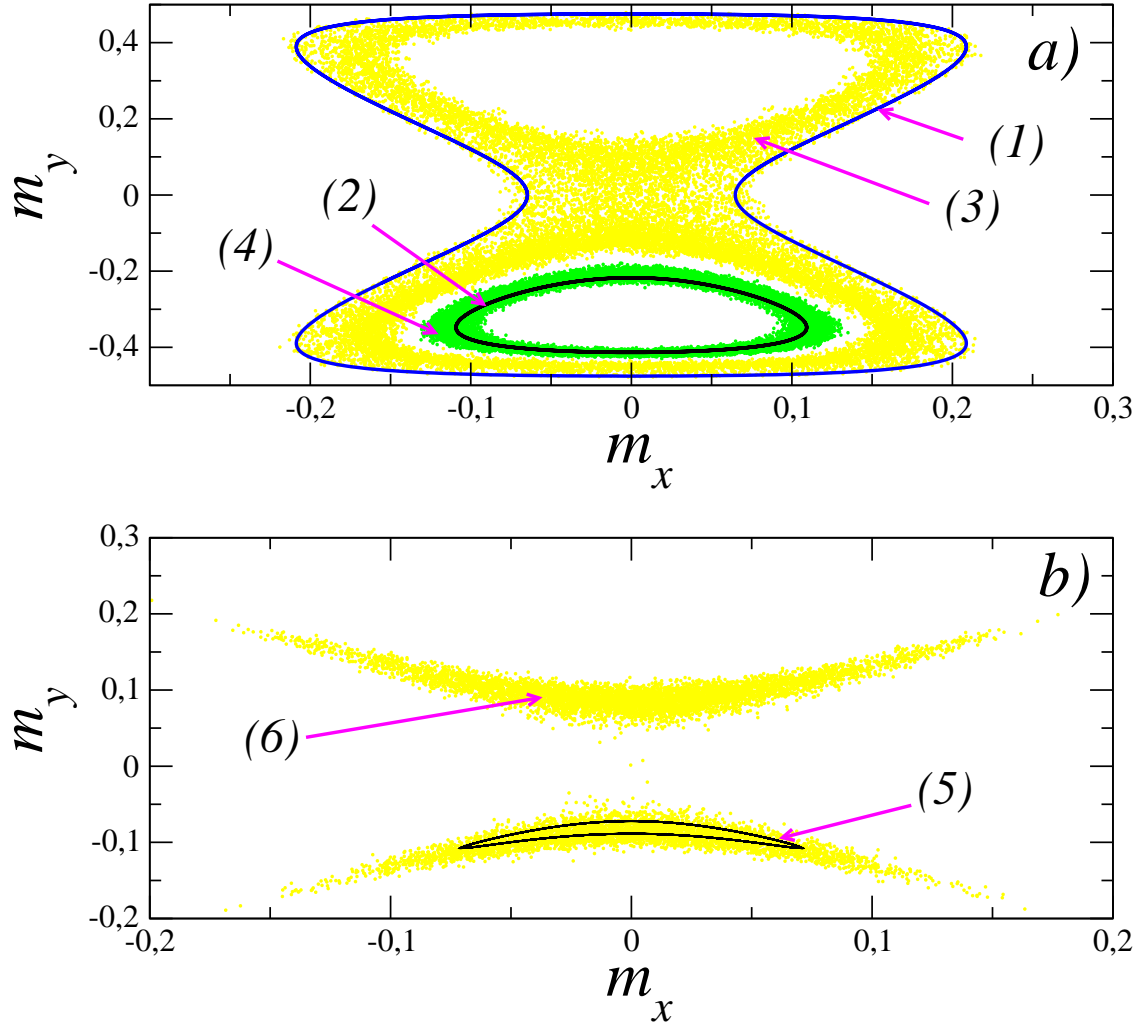


Figure 3.8: In this Fig. we consider the case  $N = 50$ ,  $B = 1$  and  $\chi = 0.663$ . We recall that  $\chi = (\epsilon - \epsilon_{ne})/(\epsilon_{stat} - \epsilon_{ne})$ . We have chosen  $J$  in order to have two different dynamical regimes: quasi-integrable,  $J = 0.1$ , Fig.a), and an highly chaotic one,  $J = 3$ , Fig.b). We plot the projection of the trajectory of  $\mathbf{m}$  over the  $xy$  plane, namely  $m_y(t)$  versus  $m_x(t)$ . In Fig. a) (quasi-integrable regime) we show two different orbits of the Mean-Field Model, labelled with (1) and (2). We also show the correspondent orbits, (3) and (4), of the full Hamiltonian, obtained starting from the same initial conditions. As one can see in the quasi-integrable regime the orbits of the full Hamiltonian remain close to the orbits of the Mean-Field Hamiltonian for all the integration time considered ( $2 * 10^4$ ). Note also that in the quasi-integrable regime some of the orbits cross the  $m_y = 0$  line, thus demagnetizing the system, and some don't. In Fig. b) (highly chaotic regime) we show one trajectory of the Mean-Field Hamiltonian, (5), and the correspondent orbit of the full Hamiltonian, obtained starting from the same initial condition. As one can see in this case the orbit of the full Hamiltonian does not remain close to the trajectory of the Mean-Field one, and covers most of the available phase-space. The integration time in this case is  $10^4$ .

### 3.7 Appendix A : Non-ergodicity threshold

Using the mean magnetization:

$$m_{x,y,z} = (1/N) \sum_{i=1}^N S_i^{x,y,z}$$

we can now rewrite the Hamiltonian (6.3) as follows:

$$H = BNm_z - \frac{J}{2} \sum_i [(S_i^x)^2 - (S_i^y)^2] + \frac{JN^2}{2}(m_x^2 - m_y^2) \quad (3.24)$$

The non-ergodic border is defined as the minimum of this Hamiltonian under the constraints:

$$\begin{aligned} a) (S_i^x)^2 + (S_i^y)^2 + (S_i^z)^2 &= 1 \\ b) m_y &= 0 \end{aligned} \quad (3.25)$$

Instead of considering the minimum of (3.24) under the constraints (3.25)b we simplify somewhat the problem calculating the absolute minimum of

$$F = BNm_z - \frac{J}{2} \sum [(S_i^x)^2 - (S_i^y)^2].$$

If such minimum value satisfy both

$$m_x = 0 \text{ and } m_y = 0 \quad (3.26)$$

the problem is equivalent to the original one.

We can take conditions (3.25a) into account setting:

$$S_i^z = \cos \theta_i, \quad S_i^x = \sin \theta_i \cos \phi_i, \quad S_i^y = \sin \theta_i \sin \phi_i$$

Taking the derivatives we obtain:

$$\begin{aligned} \frac{\partial F}{\partial \phi_i} &= J \sin^2 \theta_i \cos \phi_i \sin \phi_i = 0 \\ \frac{\partial F}{\partial \theta_i} &= \sin \theta_i [B + J \cos \theta_i \cos^2 \phi_i] = 0 \end{aligned} \quad (3.27)$$

If  $B > J$  we have just one solution:  $\sin \theta_i = 0$  that also satisfy Eq(3.26). That way all spins lye along the  $z$ -axis and

$$\epsilon_{ne} = -B, \quad \text{for } B > J \quad (3.28)$$

If  $B < J$  then from Eq.(3.27) we have two possible solutions:

- 1)  $\theta_i = \pi$ ;
- 2)  $\sin \phi_i = 0$  and  $\cos \theta_i = -BN/J$

Let us define  $0 \leq n_z \leq N$  as the number of spins satisfying 1), then

$$F(n_z) = \frac{n_z}{2J} (B - J)^2 - N \left( \frac{B^2}{2J} + \frac{J}{2} \right)$$

so that the minimum is for  $n_z = 0$  or  $\cos \theta_i = -B/J$  and  $\sin \phi_i = 0$  for all  $i$ . This is turn implies  $m_y = 0$  and for  $N$  even  $m_x = 0$  choosing for instance  $\phi_i = \pi/2$  for  $i = 1, N/2$  and  $\phi_i = -\pi/2$  for  $i = N/2 + 1, N$ .

Then we have (for  $N$  even):

$$\epsilon_{ne} = - \left( \frac{B^2}{2J} + \frac{J}{2} \right), \quad \text{for } J > B \quad (3.29)$$

### 3.8 Appendix B : Minimum energy

In this section we find the minimum of the mean Field model (3.6):

$$\epsilon = m_z + \frac{I}{2}(m_x^2 - m_y^2) \quad (3.30)$$

It is sufficient to find the absolute minimum of

$$m_z - (I/2)m_y^2$$

and verify that it satisfies  $m_x = 0$  too. Taking derivatives

$$\begin{aligned} \frac{\partial N\epsilon}{\partial \phi_i} &= Im_y \sin \theta_i \cos \phi_i = 0 \\ \frac{\partial N\epsilon}{\partial \theta_i} &= -\sin \theta_i - Im_y \cos \theta_i \sin \phi_i = 0 \end{aligned} \quad (3.31)$$

one gets two kind of solutions (both with  $m_x = 0$ ) :

- 1)  $\theta_i = \pi$  and  $\phi_i = 0, \pi$
- 2)  $\phi_i = \pm\pi/2$  and  $\tan \theta_i = \pm Im_y$

Let us define  $Nn_1$  the number of solutions of 1) and  $Nn_2$  the number of solutions of 2) so that  $n_1 + n_2 = 1$ .

Since  $m_z = -n_1 - n_2 \cos \bar{\theta}$  and  $m_y = \pm n_2 \sin \bar{\theta}$  where  $\bar{\theta}$  is the solution of 2), condition 2) is equivalent to  $\cos \bar{\theta} = 1/In_2$ . Therefore, when  $In_2 < 1$  the set defined from 2) is empty and only solutions in the class 1) can be obtained.

It is also easy to find the expression for the energy in terms of  $1/I \leq n_2 \leq 1$ :

$$\epsilon = -1 - \frac{1}{2I} + n_2 - \frac{I}{2}n_2^2 \quad (3.32)$$

Minima are at the extrema so that when  $n_2 = 1$  then  $\epsilon_{min} = -1/2I - I/2$  and when  $n_2 = 1/I$  then  $\epsilon_{min} = -1$ . In terms of  $I$ , one then has

$$\epsilon_{min} = \begin{cases} -1/2I - I/2 & \text{for } I \geq 1 \\ -1 & \text{for } I < 1 \end{cases} \quad (3.33)$$

From Eq.(3.33) we have Eq.(3.15), using transformations in Eq.(3.5).

### 3.9 Appendix C : Critical exponents

In this section we show that, assuming the reversal time dependence:

$$\tau \simeq e^{-Ns(m_y=0,\epsilon)}$$

one gets, for the ‘‘mean field model’’ described in Section II, Hamiltonian (3.6),

$$\tau \simeq \frac{1}{(\epsilon - \epsilon_{ne})^N} \quad (3.34)$$

when  $\epsilon \rightarrow \epsilon_{ne}^+$ , where  $\epsilon_{ne}$  is the non-ergodicity threshold. We consider here the case  $I > 1$ . From Eq. (3.12), we have:

$$s(m_y = 0, \epsilon) = -\lambda\epsilon + \ln\left(\frac{\sinh \lambda}{\lambda}\right) \quad (3.35)$$

where  $\lambda$  is implicitly defined by the equation

$$\epsilon = \frac{\cosh \lambda}{\sinh \lambda} - \frac{1}{\lambda}. \quad (3.36)$$

Since  $I > 1$  then  $\epsilon_{ne} = -1$ . Setting  $\epsilon = -1 + \delta$ , in Eq.(3.36), one gets  $\lambda \simeq -1/\delta$ , so that;

$$s(m_y = 0, \delta) \simeq \ln \delta = \ln(\epsilon - \epsilon_{ne}) \quad (3.37)$$

and Eq.(3.34) holds.

# Bibliography

- [1] G.L.Celardo, J.Barre, F.Borgonovi, S. Ruffo, cond-mat/04010119.
- [2] R. G. Palmer, Adv. in Phys., **31**, 669 (1982).
- [3] F. Borgonovi, G. L. Celardo, M. Maianti, E. Pedersoli, J. Stat. Phys., **116**, 516 (2004).
- [4] T. Dauxois, S. Ruffo, E. Arimondo, M. Wilkens Eds., Lect. Notes in Phys., **602**, Springer (2002).
- [5] R. B. Griffiths, C. Y. Weng, and J. S. Langer, Phys. Rev., **149**, 1 (1966).
- [6] M. Antoni, S. Ruffo and A. Torcini, Europhys. Lett., **66**, 645 (2004).
- [7] P.H.Chavanis and M.Rieutord Astronomy and Astrophysics, **412**, 1 (2003); P.H.Chavanis, astro-ph/0404251.
- [8] L.Q. English et al., Phys. Rev. B ,**67**, 24403 (2003); M. Sato et al., Jour. of Appl. Phys., **91**, 8676 (2002).
- [9] R.S. Ellis, Physica D, **133**, 106 (1999); J. Barré, F. Bouchet, T. Dauxois, S. Ruffo, cond-mat/0406358; J. Barré, Phd Thesis, ENS-Lyon, (2003).
- [10] A. Dembo, O. Zeitouni, *Large Deviations Techniques and Applications*, (Springer, Berlin, 1998).
- [11] F. Borgonovi, G. Celardo, F. M. Izrailev, and G. Casati Phys. Rev. Lett., **88**, 054101 (2002); V. V. Flambaum and F. M. Izrailev, Phys. Rev. E, **56**, 5144, (1997); F. Borgonovi and F. M. Izrailev, Phys. Rev. E ,**62**, 6475 (2000); F.Borgonovi, I.Guarneri, F.M.Izrailev and G.Casati, Phys. Lett. A,**247** , 140 (1998).
- [12] G. L. Celardo, PhD Thesis, Univ. of Milan (2004).
- [13] J. Barré, F.Borgonovi, G.L.Celardo and S.Ruffo, in preparation.
- [14] For  $J > B$  the results for odd and even  $N$  coincide up to  $(1/N)$  corrections.
- [15] B.V.Chirikov Phys. Rep., **52**, 253 (1979).
- [16] Note that the same distribution can be obtained, in a fully chaotic regime, from the time series of  $m_y(t)$ .
- [17] Sh. Kogan, *Electron Noise and Fluctuations in Solids* Cambridge Univ. Press., Cambridge (1996).
- [18] When  $J = B$  one has  $\alpha \approx 1/2$ , while for  $J \gg B$ ,  $\alpha$  has the same value as for  $B = 0$ .

- [19] M.Kac, G.E.Uhlenbeck and P.C.Hemmer, *J. Math. Phys.*, **4**, 216 (1963).
- [20] L. D. Landau and E. M. Lifshitz, *Statistical Physics* Pergamon Press, Oxford (1985).
- [21] P.Hanggi, P.Talkner, M.Borkovec, *Rev. Mod. Phys.*, **62**, 2 (1990).
- [22] V.I. Arnol'd, *DAN. USSR*, **156**, 9 (1964), A.J. Lichtenberg, M.A. Lieberman, *Regular and Stochastic Motion*, Springer-Verlag (1983).

## Chapter 4

# Quantum Signatures of the Non-Ergodicity Threshold

O what can ail thee Knight-at-arms  
Alone and palely loitering?  
The sedge has withered from the Lake  
And no birds sing!

—*La Belle Dame Sans Merci*, John Keats

### 4.1 Introduction

The content of this Chapter is completely unpublished, while in the previous Chapters we considered Classical systems, here we gathered our results on the quantum side. In this Chapter we will consider the same Models we considered in the previous Chapters. We will quantize them and we will look for quantum signatures of the classical non-ergodicity threshold,  $\epsilon_{ne}$ . The comparison between the Quantum system and the Classical one is far from being an easy task. The physicist may feel like the *knight-at-arms* of the citation quoted above, respect to *La Belle Dame sans merci* (Quantum Mechanics).

The results in the Classical case guided our investigations on the Quantum side. Mainly we are interested in a quantum signature of the classical non-ergodicity threshold, and on its relevance with respect to quantum reversal times of the magnetic moment.

Thus in this Chapter we will analyse a quantum Heisenberg model with anisotropic coupling and infinite range of the interaction.

A possible objection to the study of the infinite range coupling case could be that this kind of Models are not very common in realistic physical situations. We considered these kind of models in the quantum case too, mainly for two reasons:

- a) Our main aim is to assess the relevance of the classical non-ergodicity threshold on the quantum side. Actually, even if, as we showed in Ch.(2), the existence of the non-ergodicity threshold is a property which is likely to be valid for a generic long range interacting system with anisotropic coupling, we derived analytically this threshold for the infinite range coupling case only. Thus the infinite range case is the right choice for our theoretical purposes.
- b) There are physical systems that can be realized with modern experimental technics (1), which are described by Heisenberg Hamiltonian that contain an infinite range term, which

could induce the presence of a non-ergodicity threshold.

In this Chapter we will first analyse the spectral properties of the system, and we will establish the existence of a quantum non-ergodicity threshold in correspondence with the classical one. We will give an analytical estimate of this quantum threshold, Sec.(4.3.1). We will then study the system from a dynamical point of view and we will analyse the time scale for magnetic reversal in the quantum system, Sec.(4.5). We will compare the quantum magnetic reversal times with the classical ones. We will show the relevance of the non-ergodicity threshold respect to the time scale of the reversal of the magnetic moment in the quantum system. Moreover we will show that, due to the existence of the non-ergodicity threshold the interesting phenomena of *Macroscopic Quantum Tunneling and Coherence* emerge, Sec.(4.5.1). This opens interesting perspectives that will be briefly considered in Sect.(4.5.4).

## 4.2 Quantum considerations: generals

We will consider a system of  $N$  particles of spin  $l$ , described by the same Hamiltonian of Chapter(1),

$$H = \frac{J}{2} \sum_{i=1}^N \sum_{j \neq i} S_i^x S_j^x - \frac{J}{2} \sum_{i=1}^N \sum_{j \neq i} S_i^y S_j^y \quad (4.1)$$

Quantization of the Hamiltonian follows the standard rules. Now,  $\hat{S}_i$  are spin operators which acting on the single particle basis states in the  $z$ -representation give:  $\hat{S}_i^2 |l, s\rangle = \hbar^2 l(l+1) |l, s\rangle$  and  $\hat{S}_i^z |l, s\rangle = \hbar s |l, s\rangle$ , with  $-l \leq s \leq l$ . According to the correspondence principle, the classical limit is recovered as  $l \rightarrow \infty$ . As in the classical case we fix the modulus of the spins to one. This can be achieved with an appropriate rescaling of the Planck constant, setting  $\hbar = \hbar/|S_i| = 1/\sqrt{l(l+1)}$ . With this choice, in the classical limit,  $l \rightarrow \infty$ , the rescaled Planck constant tends to zero, but the modulus of the spins remain constant and equal to 1. Because of the infinite range nature of the interaction, the Hamiltonian (4.1) is a completely symmetric operator, respect to particle exchange. It is thus natural to limit ourselves to subspaces of definite symmetry. We chose to consider the bosonic case (an ensemble of integer spins), so we will limit our analysis in the subspace of the Hilbert space of all possible completely symmetrized states, with dimension  $\mathcal{N} = (N+2l)!/(N!(2l)!)$ , where  $N$  is the number of particles. This choice reduces considerably the dimension of the Hilbert space, allowing to extend our analysis further in the classical limit and in the large  $N$  limit. The fermionic case will be the object of a future work.

We use, for convenience, the second quantization formalism and label the basis-states according to the number of particles in the corresponding single particle states, so that  $|\Psi\rangle = |n_{-l}, n_{-l+1}, \dots, n_l\rangle$  and  $n_k$  are the occupation numbers in the  $k$ -th single particle level (or  $k$ -th projection of the spin along the  $z$ -axis). We determined the Hamiltonian matrix on this basis, to this purpose we derived analytically the action of the Hamiltonian on the basis states for generic  $N$  and  $l$ , see Appendix (A). In the same way we were able to derive the matricial form of other operator of interest, like  $m_y = 1/N \sum_{i=1}^N S_i^y$ .

An important properties of Hamiltonian (4.1) is its invariance under a rotation of  $\pi$  around the  $z$ -axis. So the Hamiltonian commutes with the operator  $e^{i\pi \sum S_i^z}$ , this implies that its eigenstates can be labeled as odd (-) or even (+) according to whether they change or do not change the sign under such rotation. Another consequence of this invariance is that the quantum probability distribution of  $m_y$  is symmetric respect to  $m_y = 0$ , in complete analogy to the classical case.

The first aim of our analysis on the quantum system is to assess the quantum signature of the classical non-ergodicity threshold,  $\epsilon_{ne}$ . Classically the non-ergodicity threshold was defined

as the threshold below which there are no phase space points such that  $m_y = 0$ , namely the probability distribution of the magnetization,  $P(m_y)$ , is zero for  $m_y = 0$  if we consider a constant energy surface below the non-ergodicity threshold. One of the main implication of the existence of this threshold is that, for continuity, the magnetization cannot change sign in time, below the non-ergodicity threshold. In order to establish the relevance of the non-ergodicity threshold in the quantum case we could consider the probability distribution of the magnetization and analyse  $P(m_y = 0)$ . But this is not the best thing to do. Indeed while in the classical case  $P(m_y = 0) = 0$  on a given energy surface implies that dynamically the magnetization cannot change sign, this is not true anymore in the quantum case. This can be shown with a simple example: let us suppose that two eigenvectors of the Hamiltonian can be written as:  $|E_1\rangle = 1/\sqrt{2}(|+\rangle + |-\rangle)$  and  $|E_2\rangle = 1/\sqrt{2}(|+\rangle - |-\rangle)$ , where  $|+\rangle$  and  $|-\rangle$  are eigenvectors of  $m_y$  corresponding to two opposite eigenvalues. The probability to have zero magnetization  $|\langle 0|E\rangle|^2$  is zero for both cases, nevertheless for any given superposition of  $|E_1\rangle$  and  $|E_2\rangle$ , the sign of the magnetization will change, unless  $E_1 = E_2$ . This shows that the same topological reasoning cannot be advocated in the quantum case to show that the magnetization cannot change sign.

It is thus advisable to take another point of view. First of all let us say that we have a striking result on the quantum side: because the spectrum of Hamiltonian 4.1 is non degenerate, see Sec(4.4), then the magnetization can always change its sign whatever the energy range we consider. This can be understood if we consider the following two facts:

- a) As seen above eigenstates can be divided into odd and even, Actually because under a rotation of  $\pi$  around the  $z$ -axis,  $m_y \rightarrow -m_y$  and  $|E_{1,2}\rangle \rightarrow \pm|E_{1,2}\rangle$ , then  $\langle E_1|m_y|E_2\rangle = -\langle E_1|m_y|E_2\rangle$ , if  $|E_1\rangle$  and  $|E_2\rangle$  are both even or odd. This implies that  $m_y$  cannot connect two eigenstate with the same parity. In particular we have  $\langle E|m_y|E\rangle = 0, \forall E$ .
- b) Let us consider an arbitrary initial state  $|\psi\rangle$ , at time  $t$  we have:  $|\psi\rangle = \sum_E C_E e^{-iEt/\hbar}|E\rangle$ . For any operator  $A$ , we can write its mean value at time  $t$  as:

$$\langle \psi(t)|A|\psi(t)\rangle = \sum_E |C_E|^2 \langle E|A|E\rangle + \sum_{E_1 \neq E_2} C_{E_1}^* C_{E_2} e^{-i(E_2 - E_1)t/\hbar} \langle E_1|A|E_2\rangle$$

Now it is immediate to recognize that the infinite time average of any operator,  $A$ , for which  $\langle E|A|E\rangle = 0 \forall E$ , is zero if the spectrum is non degenerate (2).

Obviously this implies that the infinite time average of  $m_y$  must be zero, then  $m_y$  must change sign. Despite its simplicity, this argument does not supply any information about the time scale at which this happens. Indeed it can be easily shown that in presence of quasi-degenerate levels, magnetization can keep its sign well above any experimental observational time for a large number of particles. We will then look for quantum signatures of the non-ergodicity threshold analysing the spectral properties of the system. Indeed it is clear from the above discussion that the presence of quasi-degenerate levels and their dependence on parameters ( $N$ ,  $E$ ,  $J$  and  $l$ ) plays a crucial role for the macroscopic behaviour understanding. The possibility for the magnetization to reverse its sign also in the energy region where it would be classically forbidden, can be interpreted as a manifestation of a Macroscopic Quantum Tunneling. The evaluation of the tunneling rates becomes then crucial to obtain the time scale for the quantum magnetic reversal. In Sect.(4.4) we will evaluate the tunneling rates for the Mean-Field approximation of our Model. Note that we will consider the first non-zero contribution of the perturbative theory, which, usually, is a high order contribution. For instance, to evaluate the splitting between the ground state and the first excited state (such splitting is deeply related to the tunneling rate as we will show), we have to take into account the  $Nl$ -th order contribution of the perturbative approach, since all the lower order contributions are zero.

Moreover, in the light of the correspondence principle, there should also be a fingerprint of the classical phase transition and quantum results should recover the classical ones at least in the limit  $l \rightarrow \infty, \hbar \simeq 1/l \rightarrow 0$ .

Having all this in mind we will first look for quantum signature of classical non-ergodicity threshold in the spectral properties of the system, analysing the level of degeneracy of the spectrum.

The properties of the system are very different depending on the value of  $l$ . We can distinguish two different regime: the semiclassical regime ( $l \gg 1$ ), and the hard quantum regime ( $l = 1$ ). We will discuss this two regimes separately.

In order to generalize our considerations we will introduce, when necessary, an anisotropic parameter,  $\eta$ , in the Hamiltonian (4.1).

## 4.3 Quantum signature of classical broken ergodicity

### 4.3.1 The Semiclassical Regime

The most evident property of the energy spectrum is the presence in the low energy regions of quasi degenerate doublets, see Fig.(4.1 a). Each doublet is composed by an even and an odd eigenstate. Even if from Fig.(4.1 a) they seem degenerate, they are actually splitted by an energy difference  $\delta$ . At higher energy the doublets are not well defined anymore. In Fig.(4.1 a) we have also indicated the level spacing of even states  $\Delta$ . Note that the doublets are well defined as soon as  $\delta \ll \Delta$ .

In order to obtain the splittings of the doublets,  $\delta$ , for each even eigenstate we computed numerically the minimal energy difference from an odd state. Note that, in the low energy range, because each doublet is composed by an even and an odd eigenstate, Fig.(4.1 a) ,  $\delta$  coincides with the energy difference of the eigenstates belonging to the same doublet. We could also consider  $\delta$  as a degree of degeneracy of the spectrum. In Fig.(4.1 b) we show how  $\delta$  varies with the specific energy,  $\epsilon = E/N$ , a change of slope is clearly visible, from exponential to almost constant. Note that the energy at which the slope changes is very close to the classical non-ergodicity threshold, Fig((4.1 b) . It is possible to have a better estimate of the energy at which the slope changes, considering the energy for which the doublets disappear, namely the energy,  $\epsilon^*$ , for which  $\delta(\epsilon^*) \sim \Delta(\epsilon^*)$ , see Fig((4.1 b). Note that the value  $\epsilon^*$ , distinguishes two regions of the spectrum, namely the one characterized by the quasi-degenerate eigenvalues pairs and the one which is not. Moreover we have numerical evidence that  $\epsilon^* \rightarrow \epsilon_{ne}$  as  $l$  increases, see Fig.(4.2 a).

One could then think to evaluate  $\epsilon^*$  as a quantum correction to the classical non-ergodicity threshold. An hand-waving argument to evaluate this quantum correction could be the following: in the classical case we obtained  $\epsilon_{ne}$  computing the minimum of  $-J/2 \sum (S_i^x)^2$ , see Ch.(2). Thus the lowest eigenvalue of this same operator(namely  $-J/2(\hbar l)^2$ ), could give an approximate evaluation of the quantum correction we are looking for. Note that  $\hbar l \rightarrow 1$  as  $l \rightarrow \infty$ . We will call this threshold the quantum non-ergodicity threshold,  $\epsilon_{ne}^q$ . In order to confirm this heuristic argument we considered an Hamiltonian with a generic anisotropic coupling:

$$H = \frac{J}{2} \eta \sum_{i=1}^N \sum_{j \neq i} S_i^x S_j^x - \frac{J}{2} \sum_{i=1}^N \sum_{j \neq i} S_i^y S_j^y$$

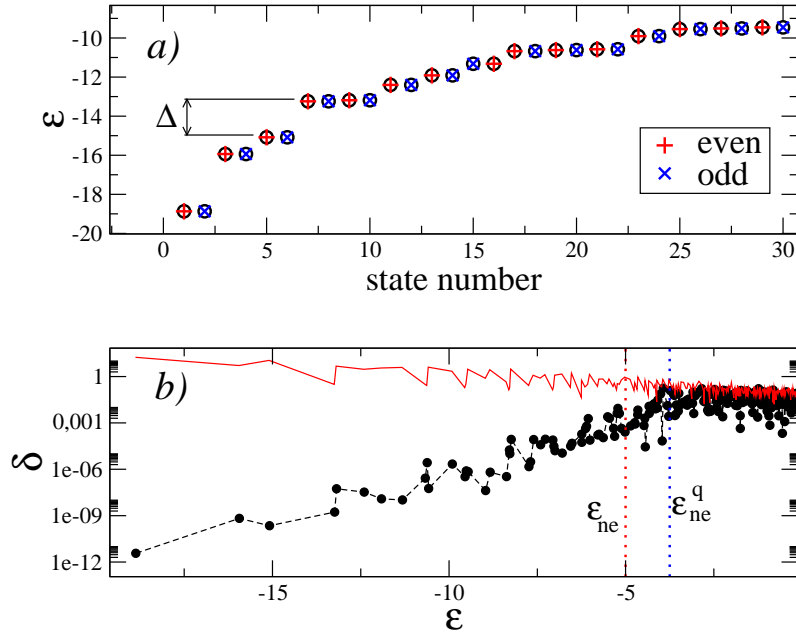


Figure 4.1:  $N = 6$   $l = 3$   $B = 0$   $J = 10$ ,  $\eta = 1$ . a) Doublet structure of the low region of the energy spectrum. The different parity of the states constituting the doublets is shown. We also indicated the level distance among even eigenstates,  $\Delta$ . Note that, even if the doublets seem to be degenerate, their states are actually separated by an energy difference  $\delta$ . b) the splitting of the doublets,  $\delta$ , is plotted versus the specific energy,  $\epsilon$  (black circles connected by dashed black line). The even level spacing  $\Delta(\epsilon)$  (red line) is also shown. As You can see the change of slope of  $\delta(\epsilon)$  approximatively occurs at  $\epsilon^*$  for which:  $\Delta(\epsilon^*) \sim \delta(\epsilon^*)$ . Also shown are the quantum non-ergodicity threshold,  $\epsilon_{ne}^q$  (dotted blue line), computed analytically from Eq.(4.2), and the classical non-ergodicity threshold,  $\epsilon_{ne}$  (dotted red line).

Where  $|\eta| < 1$  is an anisotropic parameter. Following what we did in the classical case, see Ch.(2), we evaluate  $\epsilon_{ne}^q$  from the minimum of the operator  $-J/2\eta \sum (S_i^x)^2$  when  $\eta > 0$ , and from the minimum of  $J/2\eta N^2 m_x^2 - J/2\eta \sum (S_i^x)^2$  when  $\eta < 0$ , so that we have:

$$\begin{aligned} \epsilon_{ne}^q &\sim -\frac{J}{2}\eta(\hbar l)^2 \text{ for } \eta > 0 \\ \epsilon_{ne}^q &\sim \frac{J}{2}\eta(N-1)(\hbar l)^2 \text{ for } \eta < 0 \end{aligned} \quad (4.2)$$

In Fig(4.2 b) we show that this analytical evaluation of  $\epsilon_{ne}^q$  is in good agreement with the value numerically obtained of  $\epsilon^*$ , as  $\eta$  is varied.

With the aid of  $\epsilon_{ne}^q$  it has also been possible to obtain an approximate scaling relationship for  $\delta$ , see Fig.(4.3):

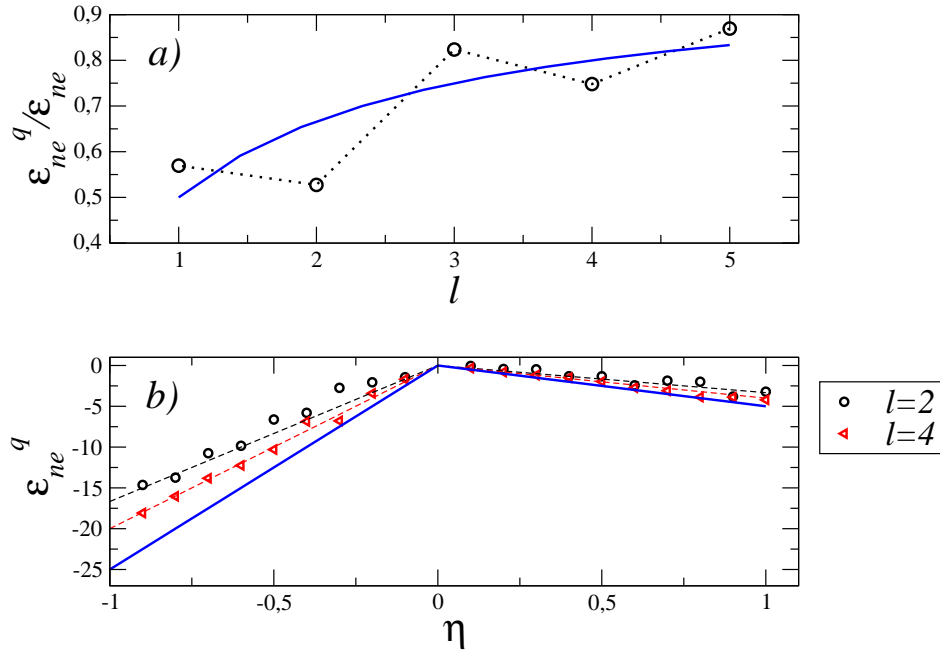


Figure 4.2: *a*) We show the ratios  $\epsilon_{ne}^q/\epsilon_{ne}$  (blue line), and  $\epsilon^*/\epsilon_{ne}$  (black circles) versus  $l$ . The quantum non-ergodicity threshold,  $\epsilon_{ne}^q$  has been obtained analytically from the formula,  $\epsilon_{ne}^q = -J(\hbar l)^2/2$ . While  $\epsilon^*$  has been obtained numerically, as the energy for which the splitting of the doublets is equal to the level spacing,  $\Delta(\epsilon^*) \sim \delta(\epsilon^*)$ . In *b*) The cases  $N = 6$ ,  $B = 0$ ,  $J = 10$ ,  $l = 2$  and  $l = 4$  are here considered. We plot  $\epsilon_{ne}^q$  vs  $\eta$  (dashed lines),  $\epsilon^*$  vs  $\eta$  (circles and triangles) for both the values of  $l$ , as indicated in figure *b*). A comparison with  $\epsilon_{ne}$  vs  $\eta$  (blue line) is also shown. Note that the agreement between  $\epsilon_{ne}^q$  and  $\epsilon^*$  is fairly good. Note also that the values of  $\epsilon_{ne}^q$  and  $\epsilon^*$  approach the ones of  $\epsilon_{ne}$  as  $l$  increases.

$$\delta \sim J e^{(-Nl\chi')} \quad (4.3)$$

Where

$$\chi' = \frac{\epsilon_{ne}^q - \epsilon}{\epsilon_{ne}^q - \epsilon_{min}}$$

The Eq.(4.16) implies that for  $l \rightarrow \infty$ , and for  $N \rightarrow \infty$ ,  $\delta \rightarrow 0$ . We will consider the dynamical consequences of Eq.(4.16) in Sec.(4.5.3).

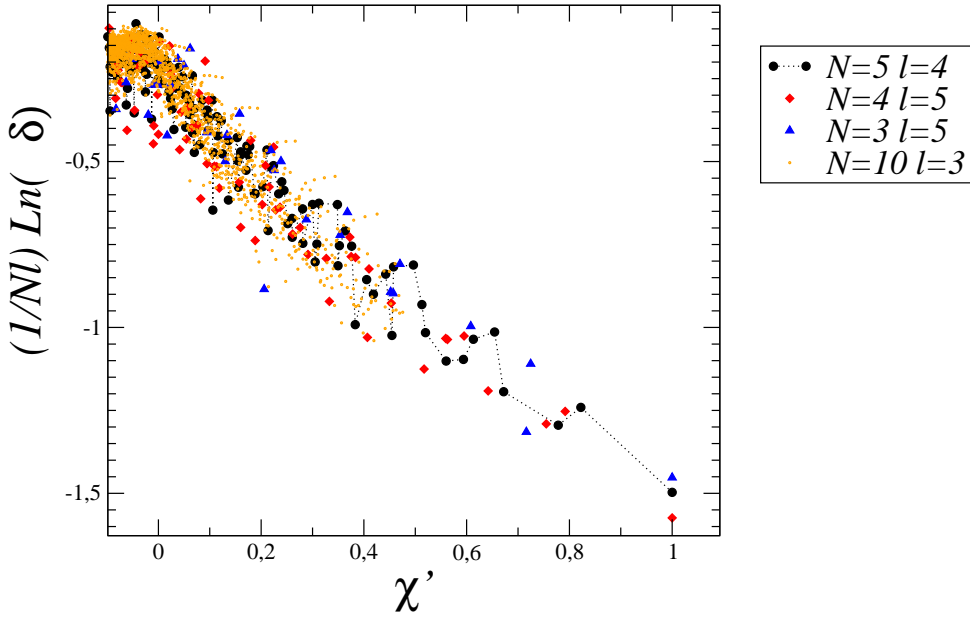


Figure 4.3: Approximate scaling relationship for  $\delta$  as a function of the parameters of the system.  $\chi' = (\epsilon_{ne}^q - \epsilon) / (\epsilon_{ne}^q - \epsilon_{min})$ .

### 4.3.2 The Hard Quantum Regime

The hard quantum regime,  $l = 1$  case, shows many differences with the large  $l$  case. In the hard quantum regime we still have doublets and an approximate exponential dependence of  $\delta$  with the energy, but it is also evident that they change regularly of many order of magnitude in small energy bins, see Fig.(4.4 a). Below we will explain why and will evaluate  $\delta$  analytically.

In order to understand the origin of this regularities better, it is useful to rewrite the Hamiltonian(4.1) in the following way:

$$H = H_{MF} + H_1 = \frac{J}{2} N^2 \{m_x^2 - m_y^2\} + \frac{J}{2} \{ \sum (S_i^y)^2 - (S_i^x)^2 \}, \quad (4.4)$$

where  $m_{x,y} = 1/N \sum_i S_i^{x,y}$ . We have rewritten the Hamiltonian of the system as a sum of a Mean-Field part, which is integrable in the classical limit, see Ch.(3), plus an additional term,  $H_1$ , which is the one responsible for the non integrability of the system.

Let us consider the eigenvectors of  $H_{MF}$ ,  $|E_{MF}\rangle$ , and let us expand the eigenvectors of  $H$ ,  $|E\rangle$  over them, so we consider the quantity:  $p_0 = |\langle E_{MF}|E\rangle|^2$ , which represents the probability that a given eigenvectors of  $H$  occupies a given eigenvector of  $H_{MF}$ .

In Fig.(4.5) we plotted for each  $|E\rangle$  the occupation probability,  $p_0$ , over the eigenvectors of the Mean-Field Hamiltonian. We identified with different colors the occupation probabilities. We see that in the  $l = 1$  case the eigenvectors of the full Hamiltonian are almost completely localized on the eigenvectors of the Mean-Field Hamiltonian, see Fig.(4.5 a) , over the majority of the energy range. Actually in the low energy region the eigenvectors occupies just one eigenstate of the Mean-Field Hamiltonian with probability greater the 0.9, while all the other

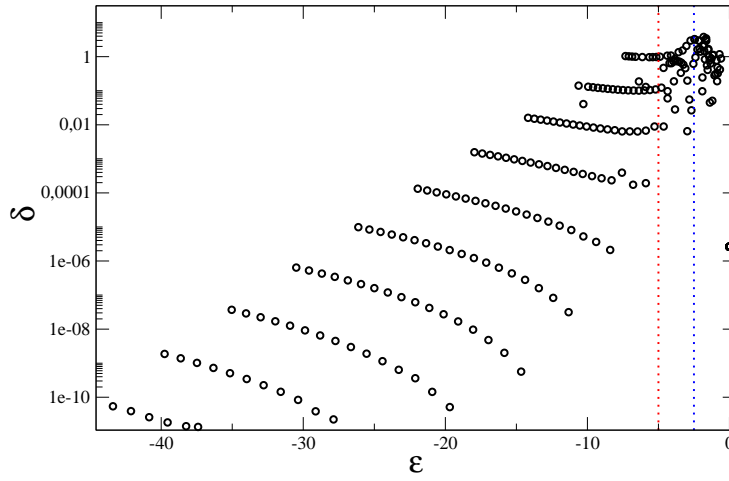


Figure 4.4: We show the splittings  $\delta$  as a function of the energy per particle, for the case  $l = 1$ ,  $J = 10$ ,  $N = 50$ . As dashed vertical dashed lines the classical non-ergodicity threshold (red) and the quantum non-ergodicity threshold (blue) have been indicated.

states are occupied with probability smaller the 0.01. The same does not happen in the large  $l$  case, see Fig.(4.5 b).

In Fig.(4.5) we compared two systems, which differ not only in  $l$  but also in  $N$ , indeed we considered the cases  $N = 100$ ,  $l = 1$  and  $N = 6$   $l = 4$ . One could think that the localization over the Mean-Field eigenvectors is due to the large number of spins and not to the low value of  $l$ . After all also the classical system tends towards the Mean-Field model as  $N \rightarrow \infty$ . On the other side we have numerical evidence, see Fig.(4.6) that keeping  $N$  constant and increasing  $l$  there is a spreading of the eigenvectors of  $H$  over the eigenvectors of  $H_{MF}$ , thus indicating that this “localization” effect is a quantum effect and not a large  $N$  effect. A possible explanation of this behaviour could lie in the pathological nature of a bosonic ensemble of particles which distribute over few single particle levels, see (3).

It interesting to note that the Mean Field Hamiltonian commutes with the total angular moment,  $m^2$ : actually in the mean Field Hamiltonian only the square of the components of the total magnetization are present, and the square of the total magnetic moment commutes with the square of its components. We have shown that in the hard quantum regime the eigenstates of the Hamiltonian are very localized over the eigenstates of the Mean-Field Hamiltonian, which are also eigenstates of  $m^2$ . Therefore in the hard quantum regime the total magnetic moment is almost a conserved quantity, in the low energy region, at variance of the correspondent classical system, see Fig.(4.7).

In the following we will analyse the consequences of the quasi-integrability of the quantum system in the hard quantum regime. In the next section we will explain the regular way in which  $\delta$  distributes over the specific energy, see Fig.(4.4), while in Sec.(4.5) we will address the dynamical consequences of this quasi-integrability.

Moreover from the above analysis follows that we can use the Mean-Field Hamiltonian to study the total Hamiltonian in the hard quantum regime, at least in the low energy range. In the next section we will show how to evaluate the eigenvalues of the Mean-Field Hamiltonian for the most part of the spectrum.

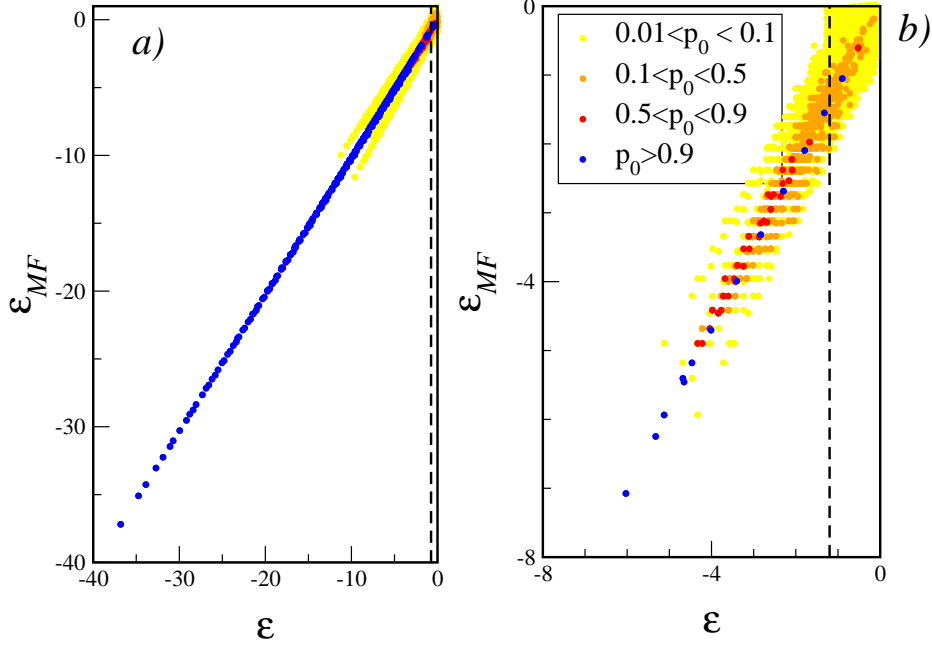


Figure 4.5: We show the probability  $p_0 = |\langle E | E_{MF} \rangle|^2$  that an eigenstate  $|E\rangle$ , with specific energy  $\epsilon$ , occupies an eigenstate  $|E_{MF}\rangle$ , with specific energy  $\epsilon_{MF}$ . Localization of eigenvectors of the full Hamiltonian, Eq.(4.4), on the Mean Field eigenvectors is evident in Fig. a) in the low energy region. The parameter values  $B = 0$ ,  $J = 3$  refer to both the figures, in a) we show the case  $N = 100$ , and  $l = 1$  and in b) the case  $N = 6$   $l = 4$ . Note that in the hard quantum regime,  $l = 1$  case, the eigenstate of the system are almost completely localized on the eigenstates of the Mean-Field Hamiltonian.

## 4.4 High Order Perturbative Approach

In this section we will present the results of a high order perturbative calculation of the eigenvalues of the Mean-Field Hamiltonian (4.4). After a rotation of  $\pi$  around the  $x$  axis which carries  $y$  in  $z$  and  $z$  in  $-y$ , and does not affect the physics of the problem, (this rotation simply facilitates the calculations), the Mean-Field Hamiltonian can be rewritten as:

$$H_{MF} = -\frac{J}{2}M_z^2 + \frac{J}{2}\eta M_x^2, \quad (4.5)$$

where  $\eta$  is the anisotropic parameter, and  $M_{z,x} = Nm_{z,x}$ . The introduction of the anisotropic parameter will help us to show the generality of our results. As discussed above the Hamiltonian(4.5) commutes with  $M^2$ . The possible values of  $M^2$  are given by the possible values of the total magnetic moment which can be obtained combining  $N$  particles of spin  $l$ , and are determined by the quantum numbers:  $Nl, Nl - 1, \dots, 0$ . From this values we should exclude the ones which cannot be combined to give completely symmetric states, if one is interested in the bosonic case. Anyway let us notice that the present approach is independent from the statistics. We can thus consider each subspace with different  $M^2$  separately: in this way the many-spin Hamiltonian(4.5), is equivalent to a set of single spin systems, described by the same Hamiltonian (4.5), if we use the rescaled Planck constant,  $\hbar = 1/(l(l+1))$ , for both the cases. Note that  $l$  is the magnitude of the spin of the many-spin problem.

In the following we will thus limit our considerations to a single spin of magnitude  $L = Nl, Nl - 1, \dots$ ,  $z$  component  $L_z$  with  $|L_z| \leq L$ . With  $|L, L_z\rangle$  as basis states, the action of  $M_z$  is

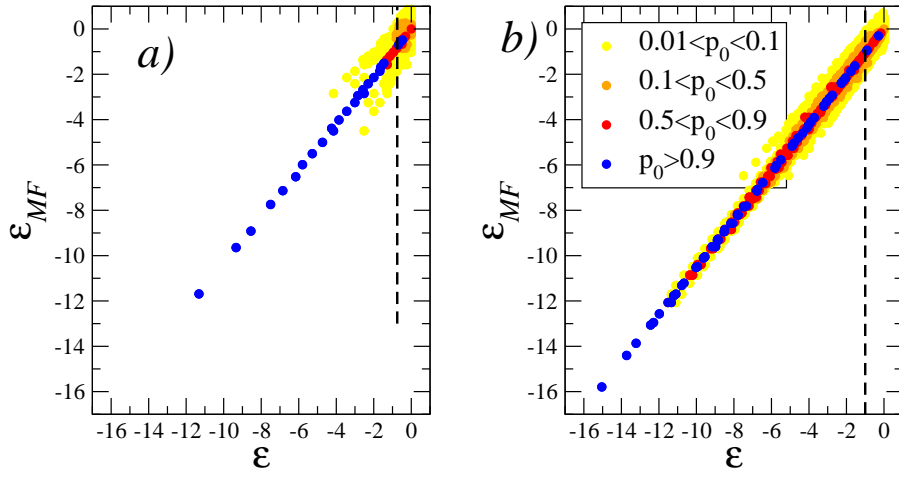


Figure 4.6: We show the probability  $p_0 = |\langle E | E_{MF} \rangle|^2$  that an eigenstate  $|E\rangle$ , with specific energy  $\epsilon$ , occupies an eigenstate  $|E_{MF}\rangle$ , with specific energy  $\epsilon_{MF}$ . The parameter values  $B = 0$ ,  $J = 3$  refer to both the figures, in a) we show the case  $N = 16$ ,  $l = 1$  and in b) the case  $N = 16$ ,  $l = 2$ . Note that as  $l$  increases the eigenstates of the full Hamiltonian become less localized over the eigenstates of the Mean-Field Hamiltonian.

the standard one:  $M_z |L, L_z\rangle = \hbar L_z |L, L_z\rangle$ .

We can further simplify the problem: Considering that  $M_x = 1/4(M^+M^+ + M^-M^-) + 1/4(M^+M^- + M^-M^+)$ , and separating the diagonal from the off diagonal contributions can write the Mean-Field Hamiltonian as

$$H_{MF} = H_0 + V$$

with

$$\begin{aligned} H_0 &= -\frac{J}{2}M_z^2 + \frac{J}{8}\eta(M^+M^- + M^-M^+) \\ V &= \frac{J}{8}\eta(M^+M^+ + M^-M^-) \end{aligned} \quad (4.6)$$

We will consider  $H_0$  as the unperturbed part of the Hamiltonian(4.5) and  $V$  as the perturbation. With this choice the perturbative approach will work fairly well as we will show in the following.

Recalling the action of  $M^+$  and  $M^-$  on the basis states:

$$\begin{aligned} M^+ |L, L_z\rangle &= \sqrt{L(L+1) - L_z(L_z+1)} |L, L_z+1\rangle = C^+(L, L_z) |L, L_z+1\rangle \\ M^- |L, L_z\rangle &= \sqrt{L(L+1) - L_z(L_z-1)} |L, L_z-1\rangle = C^-(L, L_z) |L, L_z-1\rangle \end{aligned} \quad (4.7)$$

we can compute the unperturbed energies:

$$E_0(L, L_z) = -\frac{J}{2}\hbar^2 L_z^2 + \frac{J}{4}\hbar^2 \eta [L(L+1) - L_z^2] \quad (4.8)$$

From Eq.(4.8) we see that each unperturbed energy level is doubly degenerate, with eigensubspaces spanned by  $|L, \pm|L_z|\rangle$ .

Let us consider a doublet characterized by  $L$  and  $l_0$ , where  $l_0 = |L_z|$ . We will define  $E_0^*$  the unperturbed energy of the basis states of the doublet. As we will show below the first non-zero

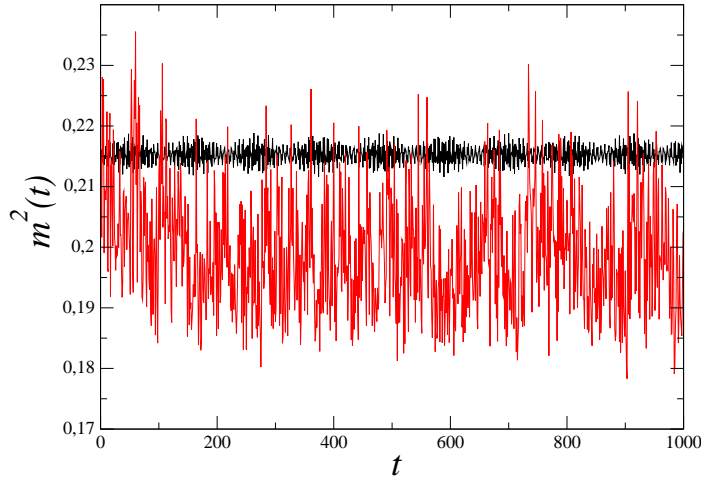


Figure 4.7: We plot  $m^2(t)$  versus  $t$  comparing the quantum behaviour (black line) with the classical one (red line). For the classical case we consider the case  $N = 16$   $J = 10$   $m^2(0) = 0.21$  and  $\epsilon = -13.78 < \epsilon_{ne} = -5$ . In the quantum case we considered the same system with  $l = 1$ . We computed  $m^2(t)$  starting from an eigenstate of the Mean-Field Hamiltonian, with  $\langle H/N \rangle = \epsilon = -13.78$ , and  $\langle m^2(0) \rangle = 0.21$ . We recall here that eigenstates of the Mean-Field Hamiltonian are eigenstate of  $m^2$  too. Note also that the Mean-Field eigenstates have a well defined energy, because they are very localized on the eigenstates of the full Hamiltonian, see Fig.(4.6).

perturbative contribution to the splitting of the degenerate unperturbed doublet defined by  $l_0$ , is at the  $l_0$ -th order. Let us thus define the  $n$ -th order perturbation operator (5):

$$\mathcal{P}^n = V \left( \frac{\phi}{E_0 - H_0} V \right)^{n-1}, \quad (4.9)$$

where  $\phi = 1 - \sum_{E_0 \neq E_0^*} |E_0\rangle \langle E_0|$  is the projector out of the considered degenerate subspace. Now, in order to find the right linear combination of the unperturbed basis vectors  $|L, \pm l_0\rangle$  to which the eigenstates of  $H_{MF}$  tend as  $V \rightarrow 0$ , we have to diagonalize the following matrix:

$$\begin{pmatrix} \langle L, +l_0 | \mathcal{P}^{(n)} | L, +l_0 \rangle & \langle L, +l_0 | \mathcal{P}^{(n)} | L, -l_0 \rangle \\ \langle L, -l_0 | \mathcal{P}^{(n)} | L, +l_0 \rangle & \langle L, -l_0 | \mathcal{P}^{(n)} | L, -l_0 \rangle \end{pmatrix} \equiv \begin{pmatrix} \mathcal{P}_{++}^{(n)} & \mathcal{P}_{+-}^{(n)} \\ \mathcal{P}_{-+}^{(n)} & \mathcal{P}_{--}^{(n)} \end{pmatrix} \quad (4.10)$$

increasing the perturbative order until we do not have two different eigenvalues of matrix (4.10). It is easy to see that  $\mathcal{P}_{++}^{(n)} = \mathcal{P}_{--}^{(n)}$  and  $\mathcal{P}_{+-}^{(n)} = \mathcal{P}_{-+}^{(n)}$ . This follows from the fact that if we make a rotation of  $\pi$  around the  $x$  axis then  $|L, +l_0\rangle$  becomes  $|L, -l_0\rangle$ , but  $\mathcal{P}^{(n)}$  does not change (indeed  $M^+ \rightarrow M^-$  and  $M^- \rightarrow M^+$  so that  $V$ , turns out to be invariant). This allows us to obtain immediately the right combination of unperturbed basis vectors, namely:

$$|+m_0\rangle = \frac{1}{\sqrt{2}}(|L, +l_0\rangle + |L, -l_0\rangle), \quad |-m_0\rangle = \frac{1}{\sqrt{2}}(|L, +l_0\rangle - |L, -l_0\rangle)$$

and the eigenvalues, given by  $E \pm \delta/2$ , where  $\delta/2 = \mathcal{P}_{+-}^{(n)}$ . Once we know the right unperturbed eigenvectors, we can write the generic  $n$ -th order energy shift,  $\Delta^{(n)}$ , induced by the perturbation as:

$$\Delta^{(n)} = \langle \pm m_0 | \mathcal{P}^{(n)} | \pm m_0 \rangle \quad (4.11)$$

Note that the effect of the perturbation can be of two different kinds: if at a given perturbative order ( $n$ ), the diagonal elements of the matrix(4.10) are different from zero but the off-diagonal elements are zero, then the perturbation will induce an overall shift,  $D$ , but will not remove the degeneracy of the considered doublet. On the other hand if the off-diagonal matrix elements are different from zero then the perturbation will remove the degeneracy, inducing a splitting,  $\delta$ .

In order to compute  $D$  and  $\delta$ , we will consider the action of  $\mathcal{P}^{(n)}$  on the basis states  $|L, \pm l_0\rangle$ .

If  $n = 1$  then  $\mathcal{P}^1 = V$ . In this case the diagonal elements of the matrix(4.10) are zero. Indeed  $\langle L, +l_0|V|L, +l_0\rangle$  is zero because  $V$  can change  $l_0$  only in  $l_0 \pm 2$ . We consider now the off-diagonal elements  $\langle L, -l_0|V|L, +l_0\rangle$ : in order to be different from zero  $V$  must carry  $|L, +l_0\rangle$  into  $|L, -l_0\rangle$ , this cannot happen unless  $l_0 = 1$ .

If  $n = 2$  then  $\mathcal{P}^2 = V \frac{\phi}{E_0 - H_0} V$ . The action of the operator  $\frac{\phi}{E_0 - H_0}$  on  $|L, L_z\rangle$  is the following: if  $|L_z| = l_0$  then it gives zero, while if  $|L_z| \neq l_0$  it leaves the state unchanged multiplied by the factor:  $\gamma = 1/(E_0(L, l_0) - E_0(L, L_z))$ . So in order to understand the action of  $\mathcal{P}^2$  we have to apply  $V$  twice. Let's consider the diagonal elements: Can we go from  $|L, +l_0\rangle$  and back to  $|L, +l_0\rangle$ , using  $V$  twice? Yes:

$$VV|L, +l_0\rangle \rightarrow |L, +l_0 - 2\rangle + |L, +l_0 + 2\rangle \rightarrow |L, +l_0\rangle + |L, +l_0 - 4\rangle + |L, +l_0 + 4\rangle + |L, +l_0\rangle$$

Note that we did not write the coefficients in front of the states (they can be easily obtained from (4.7)). Bracketing the final states thus obtained with  $|L, +l_0\rangle$ , only the first and the last remain. We can thus say that there are two “ways” in which the operator  $\mathcal{P}^2$  can carry  $|L, +l_0\rangle$  in itself: if  $l_0 > 1$  then  $|L, +l_0\rangle \rightarrow |L, +l_0 - 2\rangle \rightarrow |L, +l_0\rangle$ , and if  $l_0 < L - 1$  then  $|L, +l_0\rangle \rightarrow |L, +l_0 + 2\rangle \rightarrow |L, +l_0\rangle$ . It is now straightforward to compute the first non zero contribution to the overall shift. From (4.11) we have:

$$D = \langle L, \pm l_0|V\left(\frac{\phi}{E_0 - H_0}V\right)|L, \pm l_0\rangle, \quad (4.12)$$

and calling  $D_1$  and  $D_2$  the contributions coming from the two ways described above we have:

$$\begin{aligned} D_1 &= J\left(\frac{\eta\hbar}{4}\right)^2 \frac{[L(L+1) - l_0(l_0-1)][L(L+1) - (l_0-1)(l_0-2)]}{4(\eta+2)(1-l_0)}, \quad \text{for } l_0 > 1 \\ D_1 &= 0 \quad \text{for } l_0 \leq 1 \end{aligned} \quad (4.13)$$

And

$$\begin{aligned} D_2 &= J\left(\frac{\eta\hbar}{4}\right)^2 \frac{[L(L+1) - l_0(l_0+1)][L(L+1) - (l_0+1)(l_0+2)]}{4(\eta+2)(1+l_0)}, \quad \text{for } l_0 < L - 1 \\ D_2 &= 0 \quad \text{for } l_0 \geq L - 1. \end{aligned} \quad (4.14)$$

Thus we have that  $D = D_1 + D_2$  is the first non zero overall energy shift.

Let us now go on considering the second order perturbative operator. What can we say about the off-diagonal matrix element? Can we go from  $|L, +l_0\rangle$  to  $|L, -l_0\rangle$  using  $V$  twice? The answer is : No, unless  $l_0 = 2$ . It is also straightforward to realize that in this case we have only one way:  $|L, +l_0\rangle \rightarrow |L, +l_0 - 2\rangle \rightarrow |L, -l_0\rangle$ .

In general the first perturbative operator which splits the doublet characterized by  $L, l_0$  is the  $l_0$ -th order perturbative operator. Thus from (4.11) we have:

$$\delta = 2\langle L, +l_0|V\left(\frac{\phi}{E_0 - H_0}V\right)^{l_0-1}|L, -l_0\rangle \quad (4.15)$$

Now, from Eq.(4.15) we have that there is only one way to go from  $|L, l_0\rangle$  to  $|L, -l_0\rangle$ , which is:  $|L, l_0\rangle \rightarrow |L, l_0 - 2\rangle \dots \rightarrow |L, -l_0 + 2\rangle \rightarrow |L, -l_0\rangle$ . Therefore we get:

$$\delta = \frac{J\hbar^2}{4} \eta^{l_0} \left(\frac{-1}{2}\right)^{l_0-1} \frac{\prod_{j=-l_0}^{l_0-1} \sqrt{L(L+1) - j(j+1)}}{\prod_{p=1}^{l_0-1} (8 + 4\eta)p(l_0 - p)} \quad (4.16)$$

For  $\eta = 1$  it becomes :

$$\delta = \frac{J\hbar^2}{4} \left(\frac{-1}{24}\right)^{l_0-1} \frac{(L + l_0)!}{(L - l_0)![(l_0 - 1)!]^2} \quad (4.17)$$

So, for a given degenerate doublet characterized by  $L$  and  $l_0$ , we can compute the first non zero contribution to the overall shift  $D$  and to the splitting  $\delta$ . We will show in the next section that the first non zero contributions are enough to have a good agreement with the numerically computed eigenvalues of the Hamiltonian (4.5). Mostly we were interested in evaluating the order of magnitude of  $\delta$ . The first non-zero contributions of the perturbative approach evaluate  $\delta$  with a relative error of  $\sim 0.25$ . While it evaluates the eigenvalues with a relative error of  $\sim 10^{-3}$ . Note that here we gave average relative errors.

#### 4.4.1 Comparison with Numerical Results

As explained in the previous section the Hamiltonian(4.5) can be considered a many spin Hamiltonian and a single spin Hamiltonian as well.

We consider the single spin case first. We compare the eigenvalues and the splittings, obtained numerically, of Hamiltonian (4.5) for a single spin of magnitude  $L$ , with our perturbative results, see Eqs.(4.8,4.13,4.14,4.16):

$$E = E_0 + D + \delta$$

In Fig.(4.8) we show the splittings  $\delta$  as a function of the energy,  $E$ . We considered three different value of the total angular momentum,  $L = 10, 16, 20$  and different values of  $\eta$ ,  $\eta = 1$ , Fig.(4.8 a), and  $\eta = -0.5$ , Fig.(4.8 b).

From Fig.(4.8) we can see that the perturbative approach furnishes a very good estimate for  $E$  and  $\delta$ , in the low energy region of the spectrum, but it fails in the upper energy region. One could ask: at what energy does the perturbative approach fail? We expect that when the splittings are of the same order of the average energy difference between levels, then the perturbative approach should fail. In the previous section we called this threshold  $\epsilon^*$ , and we evaluated it with the quantum non-ergodicity threshold,  $\epsilon_{ne}^q$ . Thus we can hope to give an upper bound to the energy at which the perturbative approach fails, evaluating the quantum correction to  $\epsilon_{ne}$  for the single spin Hamiltonian. Therefore evaluating the lowest eigenvalue of the operator  $J/2\eta M_x^2$ , we get:

$$\begin{aligned} \epsilon_{ne}^q &= 0 \text{ for } \eta > 0 \\ \epsilon_{ne}^q &= J/2\eta\hbar^2 L^2 \text{ for } \eta < 0 \end{aligned} \quad (4.18)$$

In Fig.(4.8) as vertical dotted lines we show  $\epsilon_{ne}^q$ , obtained from(4.18). Note that  $\epsilon_{ne}^q$  gives a good evaluation of the energy at which the perturbative approach fails.

It is interesting to note that if  $L$  is half-integer the splittings are rigorously zero. This follows from our perturbative approach, indeed, for half-integer  $L$  values, it is not possible to go from

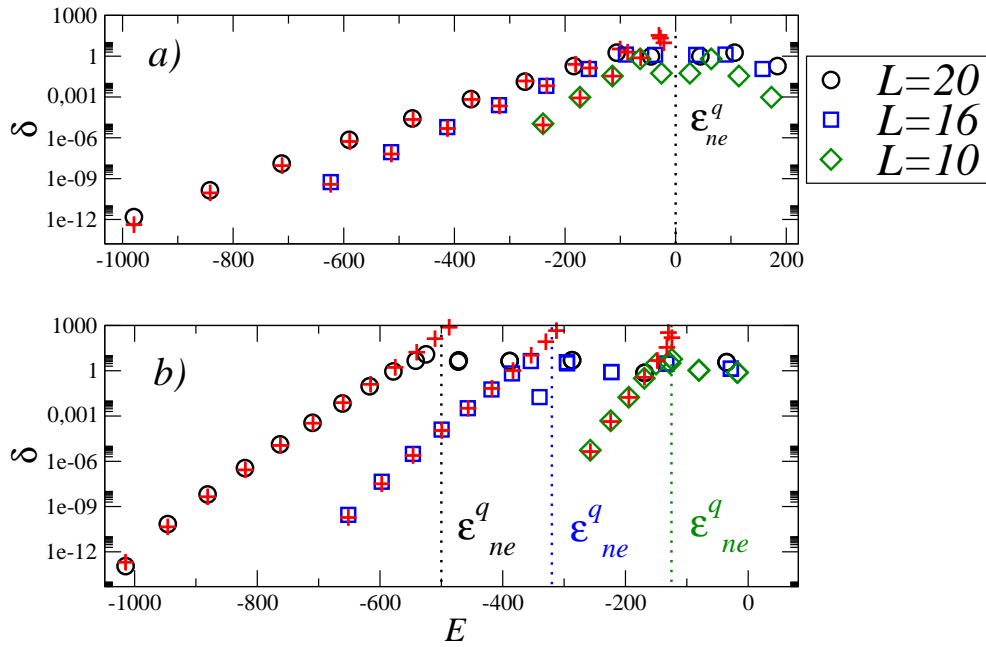


Figure 4.8: We plot  $\delta$  versus  $E$ . We compare the eigenvalues and the splittings obtained numerically for a single spin  $L$  (indicated in Figure) with the theoretical result obtained from the perturbative approach, (red crosses) for the case  $\eta = 1$ , Fig *a*), and  $\eta = -0.5$ , Fig. *b*). We also show that the upper bound for the validity of the perturbative approach (dotted lines), whose definition coincides with that of the quantum non-ergodicity threshold, is actually a very good estimation of the energy at which the perturbative approach starts to fail. Data in this Figure refer to the case  $J = 10$ ,  $l = 1$ .

$|L, +l_0\rangle$  to  $|L, -l_0\rangle$  with the perturbation operator  $V$ : because  $l_0$  will be half integer too, and  $V$  changes  $l_0$  in  $l_0 \pm 2$  only. Thus the perturbed splitting is zero (this is also called Kramers degeneracy (4)).

We will now compare our analytically eigenvalues with the eigenvalues of the Mean-Field Hamiltonian(4.5), considered as a many spin hamiltonian. We can achieve this by considering the possible eigenvalues of  $M^2$ , which are obtained when an ensemble of  $N$  particles of spin  $l$  is considered. Note that from the set of possible eigenvalues of  $M^2$  we have to exclude the ones that are not compatible with the symmetrization postulate (for the bosonic case). For each possible value of  $M^2$  we apply our perturbative approach to the correspondent single spin problem. Then, putting things together, we obtain the perturbative results for the many-spin Hamiltonian.

In Fig.(4.9) we plot the splittings versus the specific energy for the Mean-Field Hamiltonian(4.5) (black circles) and for the full Hamiltonian(4.4) (blue squares). In Fig.(4.9) also is shown the comparison with the perturbative results (red crosses). As one can see we can give a good approximation of the low energy region of the spectrum also of the full Hamiltonian in the hard quantum regime.

From Fig.(4.9) we can also see how the regular features of  $\delta$  in the hard quantum regime, Sec(4.3.2), are related to the total angular momentum quantum numbers.

One could ask if the same perturbative approach could work in the semiclassical regime for the total Hamiltonian(4.4). Another perturbative term,  $H_1$  should be added. This term can be splitted in a diagonal contribution plus a non-diagonal one. But now the calculations

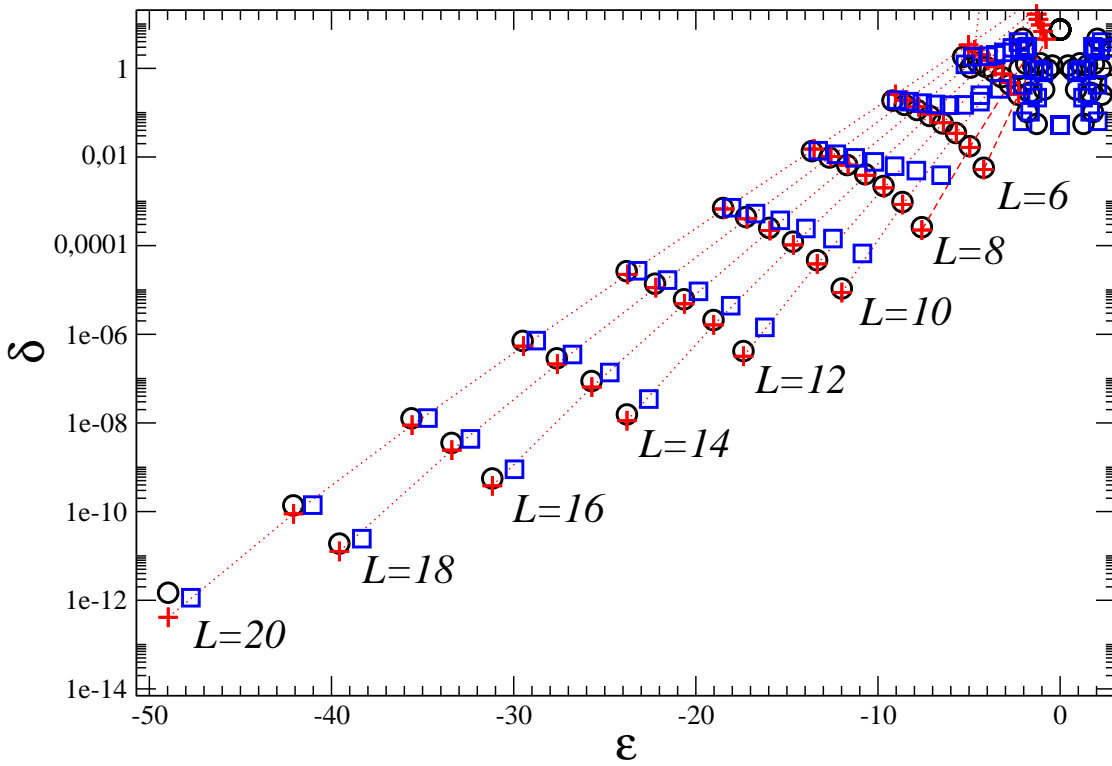


Figure 4.9: We plot  $\delta$  versus  $E$ . In this Figure we consider the many-spin case. We compare the eigenvalues and the splitting obtained numerically for the case  $N = 20$ ,  $J = 10$ ,  $\eta = 1$  and  $l = 1$  in the Mean-Field approximation (black circles), and for the full Hamiltonian, (blue squares), with the theoretical result obtained from the perturbative approach, (red crosses). The Figure shows that the perturbative gives a good evaluation of the eigenvalues and of the splitting below the quantum non-ergodicity threshold. Deviation obviously appear when the perturbative approach is compared with the splittings of the full Hamiltonian, nevertheless the perturbative approach give a fairly good estimate of the eigenvalues and splitting in the low energy region.

are not easy because many “ways” contribute to the splittings. Anyway the fact that the doublet structure of the low energy spectrum is preserved in the semiclassical regime suggest that both  $V(4.6)$  and  $H_1(4.4)$  could still be regarded as small perturbation below  $\epsilon_{ne}^q$ . Actually the perturbative splitting obtained from the Mean-Field Model works fairly well for the ground state and the first-excited-state splitting, also in the semiclassical limit, as we will show below. From Eq.(4.17) we have that the ground state splitting can be approximately written as:

$$|\delta_{GS}| = \frac{J\hbar^2}{4}(1/6)^{Nl} \quad (4.19)$$

Eq.(4.19) reproduces main features of the dependence of the ground state splitting. It shows that the splitting between the ground state and the first excited state, decreases exponentially with  $l$ , see Fig.(4.10 a), and with  $N$ , see Fig.(4.10 b). Note that in Fig.(4.10) is shown that Eq.(4.10) give the right slope of  $\delta_{GS}$  with respect to  $l$  and  $N$ . Note also that the perturbative approach furnishes the right ground state splitting for large values of  $l$  also.

Let us conclude this section noting that Mean-Field Hamiltonians are very used in micro-magnetism as phenomenological models (6; 7). Due to their experimental importance much

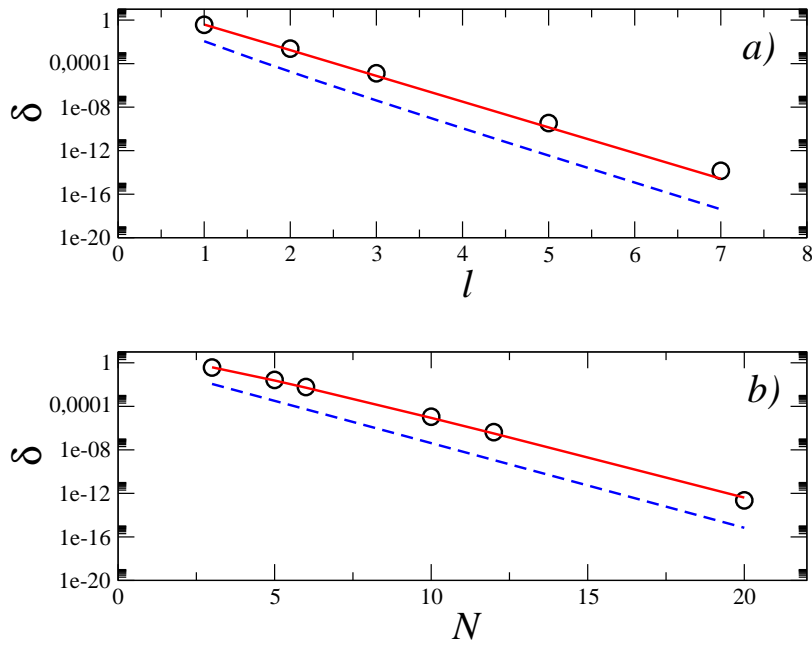


Figure 4.10: We show the splitting between the ground state and the first excited state vs  $l$ , Fig. a), and vs  $N$ , Fig. b). Numerical results, (black circle), are compared with the results obtained from the perturbative approach (red lines) Also shown is the value of  $\delta$  obtained from Eq.(4.10), (dashed blue lines).

efforts have been dedicated to compute their eigenvalues. The usual methods presented in literature to evaluate the low lying energy values are based on WKB-like approaches(8), or path integral approaches (6; 7; 9). We think that the high-order perturbative method presented here could be of some interest for its simplicity, moreover it can be easily generalized for a generic Mean-Field Hamiltonian.

## 4.5 Time Scale for Quantum Magnetic Reversal

In this section we will analyse the time scale for magnetic reversal in the Quantum system, comparing the results with what we found in the Classical system, see Ch.(3).

We studied the mean value of the magnetization in time. Let us note that if we consider the mean value of the magnetization with respect to any energy eigenstate, this would be always zero, since we showed, see Sec.(4.3.1), that  $\langle E|m_y|E\rangle = 0$ . This is not surprising if we consider that the phase space average magnetization on the whole energy surface is zero in the classical case too. Because in the classical case we determined the reversal times, fixing the energy of the system, in the quantum case we decided to compute the magnetic reversal times starting from an ensemble of initial states,  $\psi$ , built randomly combining energy eigenstates in a given energy interval. Indeed each state,  $\psi$ , is given by  $\psi = \sum' C_E|E\rangle$ , where the primed summation indicates that the sum comprehends those energy eigenstates for which the energy lies in the given energy interval  $E \pm \Delta E$ . The coefficients  $C_E$  have been randomly chosen in modulus and phase. The time dependence of the average magnetization is then given by

$$\langle m_y(t) \rangle = \langle \psi(t)|m_y|\psi(t) \rangle = \sum_{E,E'}^I C_E^* C_{E'} e^{-i(E-E')t/\hbar} \langle E'|m_y|E \rangle.$$

Since  $m_y$  connects only energy eigenstates with different parity, it can further simplified in the following way:

$$\langle m_y(t) \rangle = 2\mathcal{R}e\left\{ \sum_{E_e, E_o}^I C_{E_e}^* C_{E_o} e^{-i(E_o - E_e)t/\hbar} \langle E_e|m_y|E_o \rangle \right\} \quad (4.20)$$

From  $\langle m_y(t) \rangle$  we compute the times of first passage through zero,  $\tau_{first}$ , for each initial state of the ensemble. From these times we obtain their distribution  $P(\tau_{first})$  and the average magnetic reversal time  $\tau$ . Before presenting the results of our analysis let us mention that in the quantum case, at variance with the classical one, we are legitimate to ask what is the time scale for magnetic reversal in the whole energy range. Indeed, because the spectrum of the quantum system is completely non-degenerate, from Eq.(4.20), it is clear that the average magnetization will soon or later reverse its sign, even below the classical non-ergodicity threshold. This can be physically interpreted in terms of Macroscopic Quantum Tunneling. We will first show evidence of the possibility for the magnetization, which is a macroscopic variable, to tunnel between regions with opposite sign of the magnetization, below the classical non-ergodicity threshold, Sec.(4.5.1). We will also compare the quantum reversal times above  $\epsilon_{ne}$  with the classical one, Sec.(4.5.2). Then we will analyse the quantum reversal time below  $\epsilon_{ne}$ , Sec.(4.5.3).

### 4.5.1 Macroscopic Quantum Tunneling

In order to show the possibility of Macroscopic Quantum Tunneling for the magnetization, we have analyzed the probability to have a positive magnetization,  $P_+$ , in time, both in the classical and in the quantum case.

In the classical case we have considered an ensemble of initial condition in a given energy interval, then we have computed  $P_+$  as a function of time, counting, for each  $t$ , the number of trajectories for which  $m_y > 0$ .

Above  $\epsilon_{ne}$ , in the Classical case,  $P_+(t)$  can change in time. As seen in Ch.(3), we can characterize, in the fully chaotic regime, the behaviour of  $m_y(t)$  with an average magnetic reversal time,  $\tau$ , given by  $1/\lambda$ , where  $\lambda$  is the probability per unit time for the magnetization to reverse its sign. Since the reversal of magnetic moment in the classical case occurs at random times we can determine explicitly the time dependence of  $P_+$ . Starting with an ensemble

of  $n$  initial conditions of which  $n_+$  with a positive magnetization and  $n_-$  with a negative magnetization, such that  $n = n_+ + n_-$ . Assuming that  $m_y$  can have two values only,  $+$  and  $-$ . We can then write a set of differential equation for the population with positive and negative magnetization:

$$\begin{aligned}\dot{n}_+ &= -\lambda n_+ + \lambda n_- \\ \dot{n}_- &= -\lambda n_- + \lambda n_+\end{aligned}$$

From which we have, setting  $P_+ = n_+/n$ :

$$P_+(t) - \frac{1}{2} = (P_+(0) - \frac{1}{2})e^{-2\lambda t} \quad (4.21)$$

In Fig.(4.11 a) we show that  $P_+(t)$ , computed numerically, approaches the equilibrium value  $1/2$  in an exponential way, as predicted by Eq.(4.21). From Eq.(4.21) we also have that the time needed for  $P_+ - 1/2$  to reach the value  $(P_+(0) - 1/2)/e$  (half time), is independent of the initial distribution, and it is equal to  $1/(2\lambda)$ . In the following we will indicate the half time with  $T$ . Numerical experiments confirmed the independence of  $T$  from the distribution of initial conditions, and showed that  $T \propto \tau$ .

Below  $\epsilon_{ne}$ , in the classical system,  $P_+$  cannot change in time because for any trajectory the sign of  $m_y$  will remain the same in time.

Now, in the quantum case, we considered an initial state,  $\psi$ , built with a random superposition of energy eigenstates whose eigenvalues lie in a narrow energy range,  $\epsilon \pm \Delta\epsilon$ , and we computed the probability to have a positive magnetization at time  $t$ :

$$P_+(t) = \sum_{m>0} |\langle m|\psi(t)\rangle|^2,$$

where  $|m\rangle$  are the eigenvectors of  $m_y$  with eigenvalue  $m$ . In Fig.(4.11 b) we show the probability to have a positive magnetization versus time. We started with a random superposition of two energy eigenstates, belonging to a single doublet whose specific energy is below  $\epsilon_{ne}$ . One can see that  $P_+(t)$  changes in time. In general if we start from a doublet,  $P_+(t)$  changes in time with a frequency determined by the splitting of the considered doublet, as we will explain below. On the contrary in the Classical case  $P_+(t)$  should keep its initial value for the considered energy interval.

This undoubtedly shows the possibility of *Macroscopic Quantum Tunneling* of the magnetic moment. Usually the Tunnel effect is described in terms of an energy barrier. This can be done in this case too. Indeed in the classical case if we have a system with  $E < E_{ne}$ , we should supply at least an energy equal to  $E_{ne} - E$  if we want the magnetic moment to reverse its sign. We can thus think that in the classical case, for each system with energy  $E < E_{ne}$ , an energy barrier given by  $E_{ne} - E$  prevents the system to change the sign of the initial magnetization.

In order to show how  $P_+$  changes in the quantum case, we computed the half times,  $T$ , for different specific energies. Results are shown in Fig.(4.11 c) where  $T$  (red circles), is obtained starting from a random superposition of eigenstates, in a narrow energy range, and computing  $P_+(t)$ . As one can see  $P_+$  do change in time in the whole energy region below  $\epsilon_{ne}$ . Note that  $T$  increases exponentially with the absolute value of the energy.

The perturbative approach previously developed can give an explanation of this phenomenon, at least in the Mean-Field approximation. Indeed the eigenstates,  $E_1$  and  $E_2$ , belonging to a given doublet, in the zero order approximation, can be written as:  $|E_1\rangle \sim |L, +l_0\rangle + |L, -l_0\rangle$ , and  $|E_2\rangle \sim |L, +l_0\rangle - |L, -l_0\rangle$ . Since  $\delta = |E_1 - E_2|$ , it is immediate to realize that  $P_+$  oscillate in time between 0 and 1 with a period given by  $2\pi\hbar/\delta$ . Actually in Fig.(4.11 c) the comparison

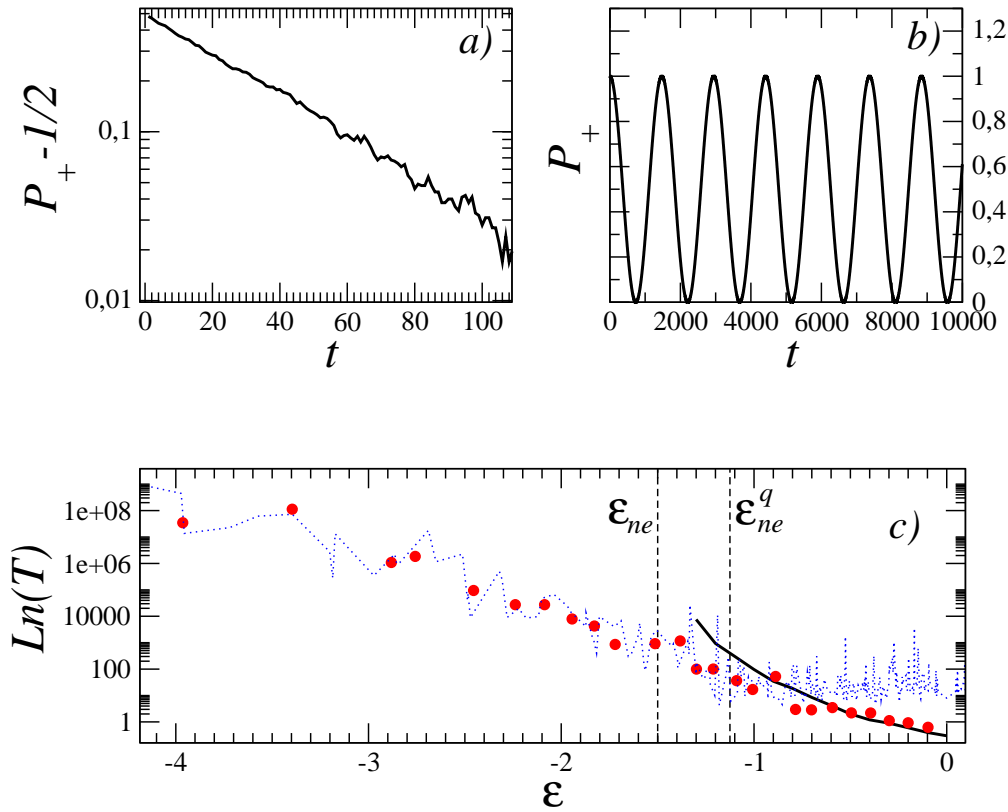


Figure 4.11: In Fig. a) it is shown the exponential decay in time of the classical probability to have a positive magnetization,  $P_+(t)$ .  $P_+(t)$  was obtained starting with an ensemble of  $10^3$  initial condition with  $m_y > 0$  for the case  $N = 6$ ,  $J = 3$  and  $\epsilon = -0.9$ . In Fig. b) the behaviour of  $P_+(t)$  is shown obtained in the quantum case for  $N = 6$ ,  $J = 3$   $l = 3$  using as a initial state a random superposition of two eigenstates belonging to a single doublet, with specific energy  $\epsilon = -2.108 < \epsilon_{ne} = -1.5$ . In Fig. c) we show the classical half times (black line). The case  $N = 6$  and  $J = 3$  has been considered. The correspondent Quantum quantity is also shown (red circles), for the case  $l = 3$  and same parameters of the classical system. Also shown (dotted blue line) is the quantity  $2\pi\hbar/(8\delta)$ , which is a good evaluation of the quantum times below  $\epsilon_{ne}^q$ . As vertical dashed black lines  $\epsilon_{ne}$  and  $\epsilon_{ne}^q$  are shown.

between  $T$  and  $2\pi\hbar/(8\delta)$  shows a good agreement. This also explains the exponential dependence of  $T$  on the specific energy and the suppression of Tunneling in the classical limit ( $\delta$  tends exponentially to zero as  $l \rightarrow \infty$ , see Sect.(4.3.1)).

The occurrence of Macroscopic Quantum Tunneling is a well known phenomenon in micro-magnetism. It has been explored both theoretically and experimentally, (9; 10; 11). Anyway, in order to interpret this phenomenon, phenomenological models, which are supposed to describe the macroscopic variables of the system, like the total magnetization, are taken into account. These phenomenological models are formally identical to the Mean-Field models, of which Eq.(4.5) is an example. On the other side let us stress that in our case the existence of the macroscopic quantum tunneling of the magnetization has been found for a microscopic spin model. Moreover we have related it to the existence of the non-ergodicity threshold and thus to the long range nature of the interaction.

Finally let us note that from Fig.(4.11 a) we see that  $P_+$  varies in time, oscillating between one and zero. This can be explained as a consequence of a quantum interference of macroscopic distinct states,  $|L, +l_0\rangle$  and  $|L, -l_0\rangle$ , a phenomenon known as *Macroscopic Quantum Coher-*

ence, that could have, if experimentally revealed, important consequences for the foundation of Quantum Mechanics (12). We will give a brief account of this in Sect.(4.5.4).

### 4.5.2 Quantum Reversal Times: Above $\epsilon_{ne}$

We will compare now the behaviour of the quantum reversal times with the classical ones above  $\epsilon_{ne}$ , both in the semiclassical regime and in the hard quantum regime.

In Fig.(4.12 a), we compare  $\tau$ , in the semiclassical regime,  $N = 6$ ,  $l = 4$ , with the classical reversal times. As we can see while they agree, approximatively above  $\epsilon_{ne}^q$ , there are deviations in the vicinity of  $\epsilon_{ne}$ , actually the classical times diverge there while the quantum ones do not. This is not surprising since the possibility of tunneling will enhance the probability for the magnetization to reverse its sign. Following what we did in the classical case we computed  $P_{max}/P_0$  from the quantum probability distribution of the magnetization,  $P(m_y)$ . We then compared the “statical” times, obtained from the same equation we used in the classical case (Eq.(3.20)), with the dynamical ones. As you can see from Fig.(4.12 a), the agreement between the statical quantum time and the dynamical ones is fairly good even in the region where the classical and the quantum times differ.

We analysed also probability distribution of first passage times ,  $P(\tau_{first})$ , in the quantum case, and it turns out to be Poissonian in the semiclassical regime, above  $\epsilon_{ne}^q$ .

On the other side, the behaviour of  $\tau$  is very different from the classical one, in the hard quantum regime, see Fig.(4.12 b). First of all quantum times are much smaller then the classical case. Moreover, above  $\epsilon_{ne}^q$ , they do not show a marked dependence with  $N$ , see Fig.(4.14), at variance with the classical ones, characterized by an exponential growth. Work is still in progress in this direction.

In the quantum hard regime Eq.(3.20) fails, of course, to give a good evaluation of  $\tau$ . In any case  $\tau$  can be evaluated from the spectral properties. Due to the quasi-integrability of the motion, see Sec.(4.3.2), one can think that few frequencies will be relevant in order to detect the time scale over which  $\langle m_y(t) \rangle$  oscillate, (that coincides with the first crossing to zero). Taking for instance  $\tau \sim \pi\hbar/(2\delta_{max})$ , where  $\delta_{max}$  is the frequency defined by the maximal matrix element  $\langle E_{odd}|m_y|E_{even} \rangle$ , one gets a good agreement with numerical results, see Fig.(4.12 b).

Moreover in the hard quantum regime  $P(\tau_{first})$  is very different from a Poissonian distribution.

### 4.5.3 Quantum Reversal Times: Below $\epsilon_{ne}$

We will now discuss the behaviour of the quantum reversal times below  $\epsilon_{ne}$ .

In the low energy region of the spectrum, due to the doublet nature of the spectrum, the dynamics will be intirely characterized by the energy difference  $|E_{even} - E_{odd}| = \delta$ . In other words, since oscillatory behaviour occurs in a time scale  $t \sim \hbar/\delta$ , this also represents the time for the first passage to zero of  $\langle m_y(t) \rangle$ . One thus expect:  $\tau \sim \hbar/(2\delta)$ . In Fig.(4.15) we show that the agreement is reasonably good in the semiclassical regime.

On the other side, the hard quantum regimes ( $l = 1$ ) does not follow this simple rule. The reason is simple and a look at Fig.(4.4) will convince the reader. In a small energy window, many different  $\delta$ , differing in many orders of magnitude are present. Therefore the dynamics will depend in a crucial way on the initial state.

From the results presented in this section we can address the problem of the dynamical signature of the classical non-ergodicity threshold. From a general point of view  $\epsilon_{ne}^q$  defines two different energy regions, both in the semiclassical regime and in the hard quantum regime. In the semiclassical regime, above  $\epsilon_{ne}^q$ , quantum reversal times, agrees with the classical ones. Below  $\epsilon_{ne}^q$ , in the classically forbidden region, quantum reversal times show an exponential dependence

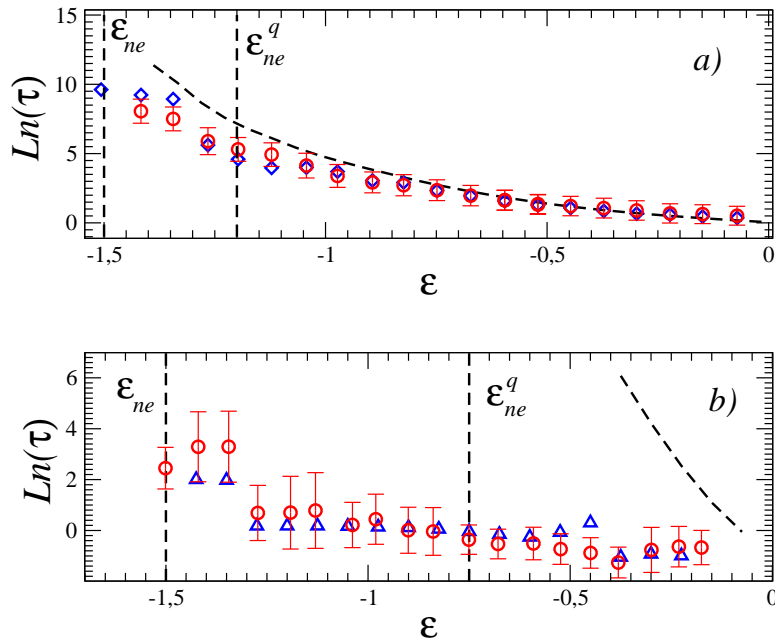


Figure 4.12: In Fig. (a) the quantum average reversal times,  $\tau$  (red circles), as a function of  $\epsilon$  is shown for the case  $B = 0$ ,  $J = 3$ ,  $N = 6$ ,  $l = 4$ , are compared with the classical ones (dashed black line), showing a good agreement above  $\epsilon_{ne}^q$  and a deviation near  $\epsilon_{ne}$ . The times obtained from  $P_{max}/P_0$  (blue diamonds), through Eq.(3.20), are in good agreement with the quantum reversal times even in the energy region where they differ from the classical ones. In Fig.(b) the quantum reversal times (red circles) for  $B = 0$ ,  $J = 3$ ,  $N = 50$ ,  $l = 1$  are shown. Comparison with the classical reversal times (dashed black line), shows that in the hard quantum the reversal times are much faster than the classical ones. Finally note that the times determined from  $\tau = \pi\hbar/(2\delta_{max})$  (blue triangles) give a good evaluation of the numerical results.

on the energy, and approximatively we have:  $\tau \sim \hbar/\delta$ . This suggest how in the classical limit the classical behaviour is recovered. From Eq.(4.16) we have that  $\delta \rightarrow \infty$  as  $l \rightarrow \infty$ , for energies below  $\epsilon_{ne}$ . Note that this is consistent with the fact that the magnetization cannot reverse its sign below  $\epsilon_{ne}$  in the classical system.

We can thus conclude that in the semiclassical regime there is a crossover, even if smooth, in correspondence of the quantum non-ergodicity threshold, from power law to exponential dependence on the energy of the magnetic reversal times.

On the other side, in the hard quantum regime, and above the quantum non-ergodicity threshold there is an almost constant dependence on the energy. While below the quantum non-ergodicity threshold, the dynamics is mostly regular and strongly dependent on the initial state.

#### 4.5.4 Towards Macroscopic Quantum Coherence

We have shown that the phenomenon of Macroscopic Quantum Tunneling and Coherence can emerge, in a microscopic spin model. Let us say that these phenomena are well known in micromagnetism (7; 6), but in this case they arises from phenomenological Hamiltonian which describe only global feature the system, and no reference to the range of the interaction has been explicitly pointed out. Note that the phenomenon of Macroscopic Quantum Tunneling has also been revealed experimentally in micromagnetic systems (6; 10; 11). On the other side the phenomenon of Macroscopic Quantum Coherence is much harder to be revealed.

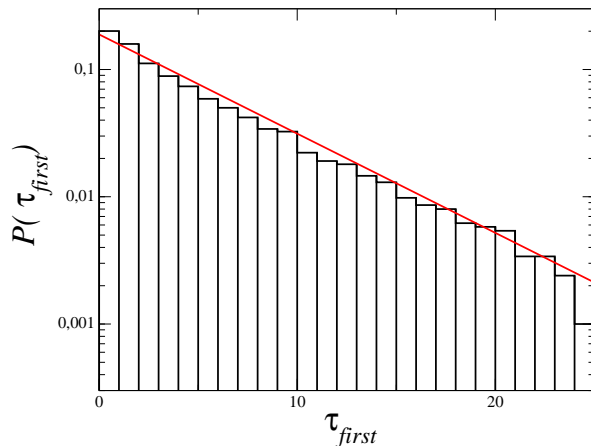


Figure 4.13: Distribution of first passage times  $\tau_{first}$ , for a system with  $N = 6$ ,  $l = 4$ ,  $J = 3$ ,  $B = 0$ ,  $e = -0.6$ . Note that the distribution is Poissonian like in the classical case. With a red line the best fit with an exponential law is shown.

In this section we will explain why the phenomenon of Macroscopic Quantum Coherence is relevant with respect to the foundation of Quantum Mechanics. This is a very complex subject and we will make only a brief and qualitative discussion.

At the basis of the Quantum Mechanical interpretation of Physical phenomena is the superposition principle: the state of a system must be described by a linear superposition of states which “represent” distinct properties of the system. Let us make an example: if we consider a spin 1/2 system, a generic state can be written as:  $|\psi\rangle = c_1|\uparrow\rangle + c_2|\downarrow\rangle$ , where  $|\uparrow\rangle$  and  $|\downarrow\rangle$  are eigenstates of the  $z$  spin component operator, and  $|c_1|^2 + |c_2|^2 = 1$ . This state is fundamentally different from a classical mixture in which we have an ensemble of spin up with probability  $|c_1|^2$  and an ensemble of spin down with probability  $|c_2|^2$ . This is easily shown if we consider the mean value of any operator which is not diagonal in the  $z$  basis, say  $S_x$ , for instance:

$$\langle\psi|S_x|\psi\rangle = 2\text{Re}[c_1^*c_2\langle\uparrow|S_x|\downarrow\rangle] = \hbar|c_1|\sqrt{1-|c_1|^2}\cos\phi$$

Here  $\phi$  is the relative phase between the states  $|\uparrow\rangle$  and  $|\downarrow\rangle$ . The term  $\langle\uparrow|S_x|\downarrow\rangle$  is called the interference term. The dependence on the relative phase of experimental results shows that quantum superposition are different from classical mixtures.

In the microscopic world the validity of the superposition principle has been never falsified. But there is no experimental evidence that a superposition of macroscopic distinct states (such as a dead and an alive cat) can be realized, even if amazing results have been obtained, such as interfering effects in macro-molecules (14).

What do we mean by superposition of macroscopic distinct states ?

A more detailed answer can be found in (7), here we will simply show an example. Let us consider an large ensemble of  $N$  1/2-spin, and the two wave functions:

$$|\psi\rangle = \prod_{i=1}^N |\uparrow\rangle + \prod_{i=1}^N |\downarrow\rangle \quad (4.22)$$

$$|\psi\rangle = \prod_{i=1}^N [|\uparrow\rangle + |\downarrow\rangle] \quad (4.23)$$

While (4.22) is a superposition of macroscopic distinct states, (4.23) is not, indeed it represents the kind of state we meet in Bose-Einstein Condensates or in superconducting devices, which

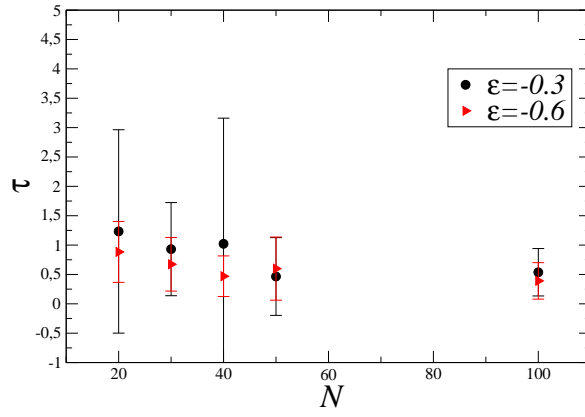


Figure 4.14: The average reversal time for  $l = 1$ ,  $B = 0$ ,  $J = 3$ , and different  $\epsilon$  is shown as a function of  $N$ . The specific energies considered are above  $\epsilon_{ne}^q$ , no exponential growth of reversal time is observed, contrary to the classical case, where they increases exponentially at fixed specific energy.

therefore cannot be considered superposition of macroscopic distinct states, even if they are example of quantum mechanical behaviour on a macroscopic scale.

How can we reveal interference effects between macroscopic distinct states?

We should at the very end, measure an operator which involves a product of all the  $N$  spins. Of course the experimental realization of such operator would be extremely hard. Anyway there is an operator which can connect the states in the superposition described in Eq.(4.22): the evolution operator. Suppose we have a double well potential and we call  $|+\rangle$  and  $|-\rangle$  the grond states of each well separately. If there is a possibility of tunneling the eigenstates of the total Hamiltonian will be different from the eigenstates of each well separately. If we call  $\delta/2$  the tunneling splitting we have:

$$\begin{aligned}
 |0\rangle &= \frac{1}{\sqrt{2}}|+\rangle + \frac{1}{\sqrt{2}}|-\rangle \\
 |1\rangle &= \frac{1}{\sqrt{2}}|+\rangle - \frac{1}{\sqrt{2}}|-\rangle
 \end{aligned} \tag{4.24}$$

where  $|0\rangle$  is the eigenstate of the system with eigenvalue  $E_0 - \delta/2$  and  $|1\rangle$  is the eigenstate of the system with eigenvalue  $E_0 + \delta/2$ . If we start from an initial state  $|\psi\rangle = c_0|0\rangle + c_1|1\rangle$  and we compute  $P_+ = |\langle +|\psi(t)\rangle|^2$  and  $P_- = |\langle -|\psi(t)\rangle|^2$  we have that:

$$P_+(t) - P_-(t) = 4|c_0||c_1|\cos(\delta t/\hbar + \gamma)$$

where  $\gamma$  is the relative phase between the states  $|0\rangle$  and  $|1\rangle$ . This phenomenon, which is called Macroscopic Quantum Coherence, would be a manifestation of quantum interference of macroscopically distinct states (QIMDS).

Revealing or not revealing this phenomen would be very important to understand if the validity of Quantum Mechanics can be extended in the macroscopic world too.

Leggett proposed a program around 1980 (7; 12), we report here the first point of its program:

- (0) Search experimentally and theoretically for a macroscopic system which is expected, provided that Quantum Mechanics remains valid, to show evidence of QIMDS under an appropriately controlled enviroment.

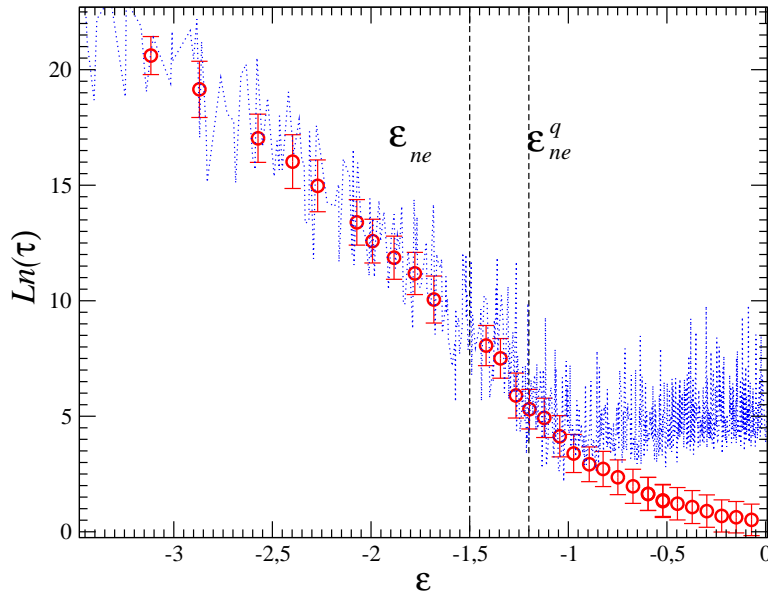


Figure 4.15: Quantum reversal times (red circles) are plotted versus  $\epsilon$  for the case:  $N = 6$ ,  $l = 4$ ,  $J = 3$ . Comparison with  $\tau \sim \pi\hbar/(2\delta)$  (dotted blue line) shows that this estimation is reasonably good. As black dashed lines  $\epsilon_{ne}$  and  $\epsilon_{ne}^q$  are also shown. Not surprisingly, the statical evaluation of  $\tau$  through  $\delta$  does not work above  $\epsilon_{ne}^q$ , where the doublet structure disappears.

In this dissertation we showed that, theoretically, the existence of the non-ergodicity threshold in an Heisenberg model can give rise on the quantum side to the phenomenon of Macroscopic Quantum Coherence. In order to make our model more realistic an appropriate environment should be added and the possibility to reveal Macroscopic Quantum Coherence re-discussed.

In (6) the problem to reveal Macroscopic Quantum Coherence has been briefly discussed. Indeed the perturbation induced by the environment should be smaller than  $\delta$  in order to leave Macroscopic Quantum Coherence. Nevertheless as  $N$  increases,  $\delta$  becomes exponentially small. This poses serious limitation on the possibility to reveal experimentally Macroscopic Quantum Coherence. On the other side we point out, see Sec.(4.3.1) that  $\delta \sim e^{-Nl\chi'}$  where  $\chi' = (\epsilon_{ne}^q - \epsilon)/(\epsilon_{ne}^q - \epsilon_{min})$ . Since  $\chi' = 0$  for  $\epsilon = \epsilon_{ne}^q$ , we have that  $\delta \sim 1$  in the neighbors of  $\epsilon_{ne}^q$ . This opens the possibility that even if  $N$  is large, at high energy, Macroscopic Quantum Coherence can be observed.

## 4.6 Conclusions

We have analysed a Quantum Heisenberg Model with infinite range of the interaction and anisotropic coupling, so that it was possible to identify an easy-axis of the magnetization (the  $y$  direction in our case). We showed that it is possible to address the problem of a quantum signature of the classical non-ergodicity threshold. First we showed this signature in the spectral properties of the system, then we showed its relevance respect to the time scale of the magnetic reversal. Let us summarize the main results of this chapter:

- i) Existence of a signature of the classical non-ergodicity threshold in the spectral properties of the system:*

We defined a quantum non-ergodicity threshold,  $\epsilon_{ne}^q$ , for which we found an approximate analytical expression. In the classical limit  $\epsilon_{ne}^q \rightarrow \epsilon_{ne}$ . Below  $\epsilon_{ne}^q$  the spectrum is charac-

terized by the presence of quasi degenerate doublets, whose energy difference  $\delta(\epsilon)$  depends exponentially on  $\epsilon$ .

ii) *Dependence of  $\delta$  on system parameters:*

In the semiclassical regime we derived an approximate scaling relation for  $\delta$  with respect to the parameters of the system. Both in the classical limit ( $l \rightarrow \infty$ ) and in the large  $N$  limit,  $\delta \rightarrow 0$ .

In the Quantum Hard regime we showed that the the system can be described by means of a Mean-Field Hamiltonian in the low energy region of the spectrum. We derived, through a high order perturbative approach,  $\delta(\epsilon)$ . We showed that the perturbative results give a good approximation of the splittings of the full Hamiltonian in the Hard Quantum regime ( $l = 1$ ). Moreover, the perturbative approach gives a good evaluation of the ground state/first excited state splitting for all the cases considered, in the semiclassical limit too. Note that it is interesting the fact that we determined an upper bound for the validity of the perturbative approach which coincides with  $\epsilon_{ne}^q$ .

iii) *Macroscopic Quantum Tunnelling:*

We analysed the dynamical properties of the system. We showed that contrary to the classical case the total magnetization can reverse its sign even below the non-ergodicity threshold. We explain this in terms of *Macroscopic Quantum Tunneling* of the total magnetic moment. We also showed the emergence, below  $\epsilon_{ne}$ , of the *Macroscopic Quantum Coherence* effect, which is due to the interference between macroscopically distinct states.

iv) *Dynamical signatures of the classical non-ergodicity threshold:*

We studied the quantum reversal times of the mean magnetization and we compared them with the classical ones above  $\epsilon_{ne}$ . Above the non ergodicity threshold the behaviour is very different depending on  $l$  values. In the semiclassical regime we showed that in correspondence of the quantum non-ergodicity threshold there is a crossover of the reversal times from a classical behaviour (for  $\epsilon > \epsilon_{ne}^q$ ), where they have a power law dependence on the specific energy, to a quantum behaviour (for  $\epsilon < \epsilon_{ne}^q$ ), where they show an exponential dependence on the specific energy.

On the other side, in the Hard quantum regime,  $\epsilon > \epsilon_{ne}^q$ , the reversal times are very small if compared with the correspondent classical system, moreover they do not show any sensible dependence on the number of particles, contrary to the classical case where the reversal times grow exponentially with the number of particles. While for  $\epsilon < \epsilon_{ne}^q$  there is a strong dependence on the initial conditions due the fact that  $\delta$  values can differ by many orders of magnitude in a small energy bin. Nevertheless we showed that  $\delta$  still have an overall exponential dependence on the energy.

## 4.7 Appendix A: Computing the Hamiltonian Matrix

The Hamiltonian(4.1) can be rewritten as:

$$H = \frac{J}{2} \sum_{i=1}^N \sum_{j \neq i}^N S_i^+ S_j^+ + \frac{J}{2} \sum_{i=1}^N S_i^- S_j^- \quad (4.25)$$

We chosed as basis state the states written in the second quantization formalism  $|K\rangle = |n_{-l}, n_{-l+1}, \dots, n_l\rangle$ , where  $n_k$  are the occupation numbers in the  $k$ -th single particle level (or  $k$ -th projection of the spin along the  $z$ -axis). In order to evaluate the Hamiltonian matrix we have

to evaluate the matrix elements  $\langle K' | \frac{J}{2} \sum_{i=1}^N \sum_{j \neq i} S_i^+ S_j^+ | K \rangle$ . This matrix element will be zero if the basis states  $|K\rangle$  and  $|K'\rangle$  differ by more than two occupation numbers,  $n_k$ . So let's say they they differ by the occupation number on the single particle states  $s$  and  $p$ . Let us set  $V = \frac{J}{2} \sum_{i=1}^N \sum_{j \neq i} S_i^+ S_j^+$ . The matrix element, is then given by:

$$\langle K' | V | K \rangle = \frac{J}{2} C_{sp} \frac{n_{sp} N_{op}}{\sqrt{N_{K'}} \sqrt{N_K}} \quad (4.26)$$

Where,

$$C_{sp} = \hbar^2 \sqrt{l(l+1) - s(s+1)} \sqrt{l(l+1) - p(p+1)}$$

and

$$N_{(K,K')} = \frac{N!}{\prod_{i=1}^l n_i!}, \quad N_{op} = \frac{N(N-1)}{2}$$

Note that with  $N_{(K,K')}$  we mean that the occupation numbers must be referred to the state  $|K\rangle$  or  $|K'\rangle$  respectively. Finally,

$$n_{sp} = \frac{(N-2)!}{\dots(n_s-1)! \dots (n_p-1)! \dots} \quad \text{for } s \neq p$$

$$n_{sp} = \frac{(N-2)!}{\dots(n_s-2)! \dots} \quad \text{for } s = p$$

A derivation of the formulas presented in this Appendix can be found in Ref.(13).

# Bibliography

- [1] L.Q. English et al., Phys. Rev. B ,**67**, 24403 (2003); M. Sato et al., Jour. of Appl. Phys., **91**, 8676 (2002).
- [2] M.Toda, R.Kubo, N.Saito, *Statistical Mechanics* Vol I, Springer-Verlag (1995).
- [3] Phys. Rev. Lett., **87**, 010601 (2001), Europhys. Lett., **59**, 340-346 (2001), Annals Phys. , **298**, 229-247 (2002).
- [4] Albert Messiah, *Quantum Mechanics*, Vol II, North-Holland Publishing Company, (1981).
- [5] J.J. Sakurai, *Modern Quantum Mechanics*, Addison-Wesley Publishing Company (1985).
- [6] E.M.Chudnovsky and J.Tejada, *Macroscopic Quantum Tunneling of the Magnetic Moment*, Cambridge University Press, (1998).
- [7] S.Takagi, *Macroscopic Quantum Tunneling*, Cambridge University Press, (1997).
- [8] M.Enz and R.Schilling, J.Phys. C, **19**, 1765-1770 (1986), M.Enz and R.Schilling, J.Phys. C, **19**, L711-L715 (1986), G.Scharf, W.F.Wreszinski and J.L.Hemmen, J.Phys. A, **20**, 4309-4319 (1987).
- [9] E.M.Chudnovsky and L. Gunther, Phys. Rev. Lett. **60**, 611 (1988).
- [10] W. Wernsdorfer and R. Sessoli, Science **284**, 133, (1999).
- [11] L. Thomas et all, Nature **383**, 145, (1996).
- [12] A.J.Leggett and A.Garg, Phys. Rev. Lett. **54**, 857 (1985), A.J.Leggett, J. Phys., **14**, R415-R451 (2002), A.J.Leggett, Rev. Mod. Phys. **59**, 1, (1987).
- [13] G.Luca Celardo, degree Thesis, Universita degli studi di Pavia (2001).
- [14] M. Arndt et all, Nature, **401**, 680 (1999).



## Chapter 5

# The non-ergodicity threshold: Conclusions and Perspectives

Lo duca ed io per quel cammino ascoso,  
intrammo a ritornar nel chiaro mondo;  
e senza cura aver d'alcun riposo,  
salimmo sú, el primo e io secondo,  
tanto ch'í vidi de le cose belle  
che porta 'l ciel, per un pertugio tondo.  
E quindi uscimmo a riveder le stelle.

—*La Divina Commedia, Inferno, Dante Alighieri*

We have shown a novel feature of long range interacting systems: the non-ergodicity threshold,  $\epsilon_{ne}$ . The existence of this threshold is interesting from the theoretical point of view, with respect to the problem of a dynamical foundation of the methods of statistical mechanics, but could have also an experimental counterpart since spin systems in which an infinite range coupling is present can be experimentally realized (1). Moreover the non-ergodicity threshold shows interesting features in itself.

For the Classical Heisenberg Model with infinite range of the interaction and anisotropic coupling, below  $\epsilon_{ne}$ , the phase space is disconnected into two components. We computed analytically this threshold for the infinite range case. We also proved that the ratio,  $r$ , between the disconnected portion of the spectrum and the whole spectrum remains finite as  $N \rightarrow \infty$ . We generalized our considerations to the case of an algebraic potential among particles which decays with the distance as  $R^{-\alpha}$ . We proved that, in a one-dimensional spin chain,  $r \rightarrow 0$  as  $N \rightarrow \infty$ , for  $\alpha > 1$ . According to the definition of long range interacting system, see Ch. (1), the interaction has a long range nature for  $\alpha < 1$  and a short range nature for  $\alpha > 1$ , in the unidimensional case. We expect that this same result can be extended in any dimension. We thus conjectured that  $r > 0$  for  $\alpha < d$  while  $r \rightarrow 0$  for  $\alpha > d$ , for  $N \rightarrow \infty$ .

We analyzed some interesting consequences of the non-ergodicity threshold:

- 1) From the point of view of Statistical Mechanics, its existence should be taken into account. Indeed  $\epsilon_{ne}$  does not disappear for  $N \rightarrow \infty$ , thus it is not a finite size effect. Below  $\epsilon_{ne}$ , the phase space is disconnected, therefore the system is rigorously non-ergodic on the whole energy surface. Thus, usual methods of Statistical Mechanics should be applied in the reduced phase space of each component. This is interesting because it indicates that for long range interacting systems ergodicity cannot be reached for any  $N$ , even if the system is chaotic.

- 2) The existence of this threshold has also important consequences with respect to phase transition from a ferromagnetic phase to a paramagnetic one. Since for energies below  $\epsilon_{ne}$  the phase space is disconnected into two components (each of which is characterized by a definite sign of the magnetization) the magnetization cannot reverse its sign below  $\epsilon_{ne}$ . Above  $\epsilon_{ne}$  and in a fully chaotic regime, the reversal time of the magnetization increases exponentially with  $N$  (for the non fully chaotic regime see discussion in Ch.(3)). Thus one could think that the non-ergodicity threshold has only a theoretical interest, because in a macroscopic system the reversal times should be so large the the existence of  $\epsilon_{ne}$  would be irrelevant. About this issue we make the following considerations: we have given numerical and theoretical evidence that, for any  $N$ , as the observational time grows to infinity, the effective transition tends to the non-ergodicity threshold and not to the threshold where Statistical Mechanics would predict a phase transition. Moreover, for any finite observational time, what determines whether the system is magnetized or not is the time scale of magnetic reversal. This time scale depends crucially on the value of the non-ergodicity threshold (magnetic reversal times diverge as a power law at the non-ergodicity threshold). Whether or not the non-ergodicity threshold have some relevance in physical experimental situations depends on the ratio of the observational time scale with respect to the reversal time scale. Indeed we have shown that the effective transition energy can be well below the statistical threshold also for systems of  $\sim 100$  spins. Last, but not least, the existence of the non-ergodicity threshold has even more interesting consequences on the quantum side, see below.
- 3) We have shown that we can address a quantum non-ergodicity threshold,  $\epsilon_{ne}^q$ , for which we gave an approximate analytical evaluation. The quantum non-ergodicity threshold tends to the classical non-ergodicity threshold in the classical limit. We showed the relevance of this threshold with respect to quantum magnetic reversal times. The most striking difference between the classical and the quantum behavior is that in the quantum case the magnetization can change its sign even below  $\epsilon_{ne}$ , through a Macroscopic Quantum Tunneling of the magnetization. The behavior of the system strongly depends on the value of the spin of each particle,  $l$ . In the semiclassical regime ( $l \gg 1$ ), we can distinguish two different regions in correspondence of the quantum non-ergodicity threshold: a “classical” region, for  $\epsilon > \epsilon_{ne}^q$ , in which the reversal times have an algebraic dependence on the energy and a quantum region, for  $\epsilon < \epsilon_{ne}^q$  in which the reversal times have an exponential dependence on energy. Thus we can regard  $\epsilon_{ne}^q$  as a threshold which distinguishes between a quasi-classical and a purely quantum regime.

In the hard quantum regime ( $l = 1$ ),  $\epsilon_{ne}^q$  also distinguishes two energy regions: for  $\epsilon > \epsilon_{ne}^q$ , reversal times are extremely fast if compared with the classical one, moreover they do not show any exponential dependence on  $N$ . Below  $\epsilon_{ne}^q$ , the system is very close to a Mean-Field Model, which is an integrable model, thus the reversal times are extremely dependent on the initial conditions. Even in such unlikely situation some general conclusion can be drawn. The modulus of the total angular momentum,  $m^2$ , is a quasi-constant of motion for  $\epsilon < \epsilon_{ne}^q$ , and for any  $m^2$  fixed value the dependence of the reversal times on energy is exponential. The fact that above  $\epsilon_{ne}^q$  the reversal times are very small and independent of  $N$ , while below  $\epsilon_{ne}^q$  they increase with  $N$ , suggest the possibility, for large enough  $N$ , to regard  $\epsilon_{ne}^q$  as the effective threshold which distinguishes between magnetized and unmagnetized states, in the hard quantum regime. Anyway in order to prove this statement, more research is still needed.

Moreover through a high order perturbative approach we have computed the splittings of the energy levels in the Mean-Field Model. We have shown that we can consider the

quantum non-ergodicity threshold as a perturbative threshold, namely we can regard  $\epsilon_{ne}^q$  as an upper bound for the validity of the perturbative approach.

Finally we have shown that below  $\epsilon_{ne}^q$ , the phenomena of Macroscopic Quantum Tunneling and Coherence can be found, see Ch. (4), Sect.(4.5.1, 4.5.4).

One of the first aims of our future research work is to compute analytically the non-ergodicity threshold for the case of  $R^{-\alpha}$  potential in 1 dimension. Then we will try to generalize the results to any dimension, and possibly to more general form of the potential. Indeed we showed that this threshold has a deep connection with the long range nature of the interaction, which should be independent from the particular kind of interaction.

A different promising line of research is in the field of Quantum Computation. As explained in Ch.(6), there are still many problems involved in the realization of Quantum Computers, not last the choice of the “right” model. The possibility to design quantum devices in which Macroscopic Quantum Tunneling is involved has been also recently proposed (2). Let us say that in these proposal the phenomenon of Macroscopic Quantum Tunneling of Magnetization arises from phenomenological Hamiltonian for micromagnetism, and no reference to the range of the interaction has been explicitly pointed out. So the object of this line of research is to investigate the role of the range of interactions in quantum computation.

Finally we would like to address another interesting direction of research: the possibility to reveal experimentally Macroscopic Quantum Coherence, which has been discussed in Ch.(4), Sect.(4.5.4).



# Bibliography

- [1] L.Q. English et al., Phys. Rev. B ,**67**, 24403 (2003); M. Sato et al., Jour. of Appl. Phys., **91**, 8676 (2002).
- [2] J. Tejada et all, Nanotechnology **12**, 181, (2001).



# Chapter 6

## Quantum Computation

Quantum Mechanics does not occur in a  
Hilbert Space.  
It occurs in a Laboratory.

—*Asher Peres*

### 6.1 Introduction

What is a Quantum Computer?

A Quantum Computer is a quantum system which is able to implement a sufficiently high number of logical operations, such that it can be considered a Computer.

The idea to use a quantum mechanical system as a computer is due to Feynman (1), but it was only after P. Shor's results (2) that this topic became one of the most appealing research field. P. Shor showed that a Quantum Computer could find the prime factors of an integer number exponentially faster than any known classical computer. The discovery of this algorithm showed the potentiality of a Quantum Computer, indeed the discovery of an efficient algorithm for the prime number factorization problem was one of the historically unsolved problems of classical computer science. Besides the development of other algorithms like the Grover's one (3), the experimental realization of simple Quantum Computers began. The experimental realization of a Quantum Computer is a great challenge, nevertheless unsuspected results have been obtained, such as the implementation of Shor's algorithm in a nuclear magnetic resonance Quantum Computer (4). Quantum Computation is not interesting only with respect to applications, indeed it is a formidable playground with respect to problems related with the foundations of Quantum Mechanics. An example of this is the phenomenon of teleportation of a quantum state between distant systems (5). This phenomenon has been also recently realized, (6).

Nevertheless building a "useful" Quantum Computer is still a great theoretical and experimental challenge. The problems involved here are different and are related with all the aspects of a Quantum Computer: preparation of an initial state, its evolution towards the desired final state, and finally the read-out of the final state, from which the result of the computation is obtained.

In these years our group analyzed a solid state model of Quantum Computation (7), made of a linear chain of spin  $1/2$ , with Heisenberg interaction and located in an external magnetic field which has a gradient along the spin chain. The evolution of the system is obtained through a sequence of resonant electromagnetic pulses which cause resonant transitions of initial states towards the desired final states. We mainly concentrated on the problem of reducing the errors

during the dynamical evolution of the system. Unfortunately there are many unwanted errors producing transitions to be washed. Few preliminar investigations (8), that we attached in Sec.(6.2), have indicated a way to reduce drastically the quasi-resonant transitions, and a general method, the “generalized  $2\pi k$  method”, was developed to suppress main causes of dynamical errors (9). Nevertheless the remaining dynamical errors, due to non-resonant transitions, can still be relevant as was shown in Ref. (10; 11).

Besides intrinsic dynamical errors, we also considered external errors, which have been taken into account through a random perturbation of the parametres of the system. We have done a detailed analysis of how Fidelity is affected by different kinds of error in the parameters. Fidelity is a measure of the errors we make during the computation, it is given by the square of the scalar product of the ideal final state with the real final state. We showed that in general the Fidelity decays as  $F = 1 - (dG/\Omega)^2 n^\alpha$  where  $dG$  is the absolute error on the parameter  $G$ ,  $\Omega$  is the Rabi frequency and  $n$  is the number of qubits. The system has shown a great sensitivity on gradient errors.

External errors have been also taken into account adding a random GUE perturbation on the evolution of the system:  $U_\delta(t) = e^{-i\delta V(t)}U(t)$ , where  $U_\delta(t)$  is the perturbed evolution,  $U(t)$  the unperturbed evolution and  $V$  is a perturbation obtained from the GUE ensemble. In order to analyze the sensitivity of the system to both intrinsic and extrinsic errors we used a procedure developed in Ref.(12), called “Correlation Function Approach” to Fidelity. In (12), on the basis of this procedure, an Improved Quantum Fourier Transform (IQFT) algorithm was proposed which is more stable with respect to random GUE perturbation.

In (11), that we attached in Sec.(6.2), we tested this Improved algorithm on our model of Quantum Computation, and we also tested the generalized  $2\pi k$  method. We briefly summarize here the main results :

- 1) We successfully tested the Generalized  $2\pi K$  method, on a complex algorithm, the Quantum Fourier Transform (QFT). With complex we mean that the number of pulses,  $P$ , needed to implement it is not linear on the number of qubits, indeed  $P \sim O(n^3)$ .
- 2) We applied the Correlation Function Approach on a realistic model of Quantum Computer, showing that it can be useful to analyze Fidelity dependence on the parameters of the system. Indeed we found that the intrinsic non-resonant errors grow very fast with the number of qubits,  $O(n^6)$ .
- 3) We tested the improved QFT protocol, on our model of Quantum Computer. We showed it is able to decrease static GUE perturbation. IQFT requires higher number of pulses, so higher dynamical errors. We showed that dynamical errors are worst then static external ones ( $O(n^6)$  vs  $O(n^{2/3})$ ). So IQFT cannot improve QFT asymptotically. Nevertheless using QFT and IQFT together we were able to improve Fidelity with respect to both kind of errors, in a wider range of parameters.

## 6.2 Dynamical fidelity of a solid-state quantum computation

### 6.2.1 Introduction

Many suggestions for an experimental realization of quantum computers are related to two-level systems (*qubits*). One of the serious problems in this field is a destructive influence of different kinds of errors that may be dangerous for the stability of quantum computation protocols. In the first line, one should refer to finite temperature effects and interaction of qubits with an environment (13). However, even in the case when these features can be neglected, errors can be generated by the dynamics itself. This “dynamical noise” can not be avoided since the interaction between qubits and with external fields are both necessary for the implementation of any quantum protocol. On the other hand, the inter-qubit interaction may cause the errors. Therefore, it is important to know to what extent the interaction effects may be dangerous for quantum computation.

As is known from the theory of interacting particles, a two-body interaction between particles may result in the onset of chaos and thermalization, even if the system under consideration consists of a relatively small number of particles (see, for example, the reviews (14; 15; 16) and references therein). In application to quantum computers, quantum chaos may play a destructive role since it increases the system sensitivity to external perturbations. Simple estimates obtained for systems of  $L$  interacting spins show that with an increase of  $L$  the chaos border decreases, and even a small interaction between spins may result in chaotic properties of eigenstates and spectrum statistics. On this ground, it was claimed (17) that quantum chaos for a large number of qubits can not be avoided, and the idea of a quantum computation meets serious problems.

On the other hand, recent studies (18) of a realistic 1/2-spin model of a quantum computer show that, in the presence of a magnetic field gradient, the chaos border is independent on  $L$ , and that quantum chaos arises in extreme situations only, which are not interesting from the practical viewpoint. One should stress that a non-zero gradient magnetic field is necessary in the model (18) for a selective excitation of different qubits under time-dependent electromagnetic pulses providing a specific quantum protocol.

Another point that should be mentioned in the context of quantum chaos is that typical statements about chaos refer to stationary eigenstates and spectrum statistics. However, quantum computation is essentially a time-dependent problem. Moreover, the time of computation is restricted by the length of a quantum protocol. Therefore, even if stationary Hamiltonians for single pulses reveal chaotic properties, it is still not clear to what extent stationary chaos influences the evolution of a system subjected to a finite number of pulses.

In contrast with our previous studies (18), in this paper we investigate the time evolution of a 1/2-spin quantum computer system subjected to a series of pulses. Specifically, we consider a quantum protocol that allows to create an entangled state for remote qubits. For this, we explore the model in the so-called *selective* regime, using both analytical and numerical approaches. Our analytical treatment shows that in this regime there is no fingerprint of quantum chaos. Moreover, we show that a kind of perturbative approach provides a complete description of the evolution of our system.

We concentrate our efforts on the introduced quantity (*dynamical fidelity*). This quantity characterizes the performance of quantum computation associated with the *dynamical* errors. Dynamical fidelity differs from the fidelity which is widely used nowadays in different applications to quantum computation and quantum chaos, see for instance (19), because we do not add any random variation in the Hamiltonian. Our study demonstrates an excellent agreement of analytical predictions with numerical data.

The structure of the paper is as follows. In Section II we discuss our model and specify the

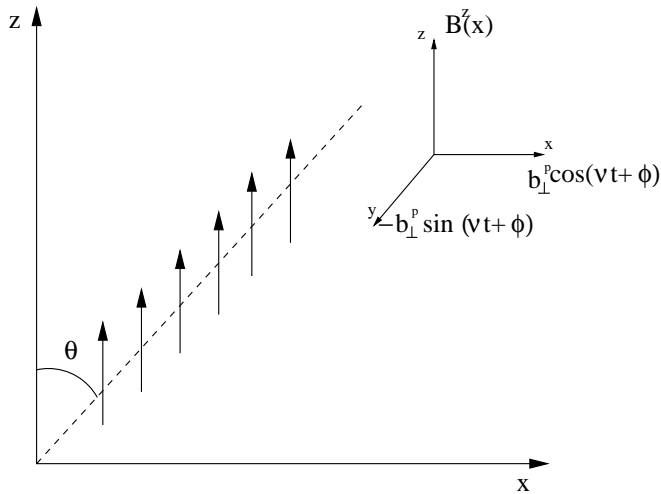


Figure 6.1: Spin model for quantum computation. Also indicated the direction of the magnetic field (6.1).

region of parameters for which our study is performed. In Section III we explore the possibility of quantum chaos in the selective regime, and analytically show that chaos can not occur in this case. We provide all details concerning the quantum protocol in Section IV, and demonstrate how perturbation theory can be applied to obtain an adequate description of the fidelity in dependence on the system parameters. Here, we also present numerical data and compare them with the predictions based on the perturbative approach. The last Section V summarizes our results.

## 6.2.2 Spin model of a quantum computer

Our model is represented by a one-dimensional chain of  $L$  identical  $1/2$ -spins placed in an external magnetic field, see Fig.6.1.

It was first proposed in (20) (see also (21; 22; 23)) as a simple model for solid-state quantum computation. Some physical constraints are necessary in order to let it operate in a quantum computation regime. To provide a selective resonant excitation of spins, we assume that the time independent part  $B^z = B^z(x)$  of the magnetic field is non-uniform along the spin chain. The non-zero gradient of the magnetic field provides different Larmor frequencies for different spins. The angle  $\theta$  between the direction of the chain and the  $z$ -axis satisfies the condition,  $\cos \theta = 1/\sqrt{3}$ . In this case the dipole-dipole interaction is suppressed, and the main interaction between nuclear spins is due to the Ising-like interaction mediated by the chemical bonds, as in a liquid state NMR quantum computation (13).

In order to realize quantum gates and implement operations, it is necessary to apply selective pulses to single spins. The latter can be distinguished, for instance, by imposing a constant-gradient magnetic field that results in the Larmor frequencies  $\omega_k = \gamma B^z(x_k) \equiv \omega_0 + ak$ , where  $\gamma$  is the spin gyromagnetic ratio and  $x_k$  is the position of the  $k$ -th spin. If the distance between the neighboring nuclear spins is  $\Delta x = 0.2$  nm, and the frequency difference between them is  $\Delta f = a/2\pi = 1$  kHz, then the corresponding gradient of the magnetic field can be estimated as follows,  $|dB^z/dx| = \Delta f/(\gamma/2\pi)\Delta x \approx 1.2 \times 10^4$  T/m. Here we used the gyromagnetic ratio for a proton,  $\gamma/2\pi \approx 4.3 \times 10^7$  Hz/T. Such a magnetic field gradient is experimentally achievable, see, for example, (24; 25).

In our model the spin chain is also subjected to a transversal circular polarized magnetic

field. Thus, the expression for the total magnetic field has the form (18; 22; 23),

$$\mathbf{B}(t) = [b_{\perp}^p \cos(\nu_p t + \varphi_p), -b_{\perp}^p \sin(\nu_p t + \varphi_p), B^z(x)]. \quad (6.1)$$

As mentioned above, here  $B^z(x)$  is the constant magnetic field oriented in the positive  $z$ -direction, with a positive  $x$ -gradient (therefore,  $a > 0$  in the expression for the Larmor frequencies). In the above expression,  $b_{\perp}^p$ ,  $\nu_p$ , and  $\varphi_p$  are the amplitudes, frequencies and phases of a circular polarized magnetic field, respectively. The latter is given by the sum of  $p = 1, \dots, P$  rectangular time-dependent pulses of length  $t_{p+1} - t_p$ , rotating in the  $(x, y)$ - plane and providing a quantum computer protocol.

Thus, the quantum Hamiltonian of our system has the form,

$$\begin{aligned} \mathcal{H} = & - \sum_{k=0}^{L-1} \left[ \omega_k I_k^z + 2 \sum_{n>k} J_{k,n} I_k^z I_n^z \right] - \\ & \frac{1}{2} \sum_{p=1}^P \Theta_p(t) \Omega_p \sum_{k=0}^{L-1} \left( e^{-i\nu_p t - i\varphi_p} I_k^- + e^{i\nu_p t + i\varphi_p} I_k^+ \right), \end{aligned} \quad (6.2)$$

where the ‘‘pulse function’’  $\Theta_p(t)$  equals 1 only during the  $p$ -th pulse, for  $t_p < t \leq t_{p+1}$ , otherwise it is zero. The quantities  $J_{k,n}$  stand for the Ising interaction between two qubits,  $\omega_k$  are the frequencies of spin precession in the  $B^z$ -magnetic field,  $\Omega_p$  is the Rabi frequency of the  $p$ -th pulse,  $I_k^{x,y,z} = (1/2)\sigma_k^{x,y,z}$  with  $\sigma_k^{x,y,z}$  as the Pauli matrices, and  $I_k^{\pm} = I_k^x \pm iI_k^y$ .

For a specific  $p$ -th pulse, it is convenient to represent the Hamiltonian (6.2) in the coordinate system that rotates with the frequency  $\nu_p$ . Therefore, for the time  $t_p < t \leq t_{p+1}$  of the  $p$ -th pulse our model can be reduced to the *stationary* Hamiltonian,

$$\mathcal{H}^{(p)} = - \sum_{k=0}^{L-1} (\xi_k I_k^z + \alpha I_k^x - \beta I_k^y) - 2 \sum_{n>k} J_{k,n} I_k^z I_n^z, \quad (6.3)$$

where  $\xi_k = (\omega_k - \nu_p)$ ,  $\alpha = \Omega_p \cos \varphi_p$ , and  $\beta = \Omega_p \sin \varphi_p$ .

We start our considerations with the simplified case of the Hamiltonian (3) for a single pulse, by choosing  $\varphi_p = 0$ . We also assume a constant interaction between nearest neighbors qubits only ( $J_{k,n} = J\delta_{k,k+1}$ ), and we put  $\Omega_p = \Omega$ . Then the Hamiltonian (3) takes the form,

$$\mathcal{H}^{(p)} = \sum_{k=0}^{L-1} \left[ -\xi_k I_k^z - 2J I_k^z I_{k+1}^z \right] - \Omega \sum_{k=0}^{L-1} I_k^x \equiv H_0 + V. \quad (6.4)$$

In  $z$ -representation the Hamiltonian matrix of size  $2^L$  is diagonal for  $\Omega = 0$ . For  $\Omega \neq 0$ , non-zero off-diagonal matrix elements are simply  $H_{kn} = H_{nk} = -\Omega/2$  with  $n \neq k$ . The matrix is very sparse, and it has a specific structure in the basis reordered according to an increase of the number  $s$ . The latter is written in the binary representation,  $s = i_{L-1}, i_{L-2}, \dots, i_0$  (with  $i_s = 0$  or 1, depending on whether the single-particle state of the  $i$ -th qubit is the ground state or the excited one). The parameter  $\Omega$  thus is responsible for a non-diagonal coupling, and we hereafter define it as a ‘‘perturbation’’.

In our previous studies (18) we have analyzed the so-called *non-selective* regime which is defined by the conditions,  $\Omega \gg \delta\omega_k \gg J$ . This inequality provides the simplest way to prepare a homogeneous superposition of  $2^L$  states needed for the implementation of both Shor and Grover algorithms. Our analytical and numerical treatment of the model (2) in this regime has shown that a constant gradient magnetic field (with non-zero value of  $a$ ) strongly reduces the effects of quantum chaos. Namely, the chaos border turns out to be independent on the number  $L$  of

qubits. As a result, for non-selective excitation quantum chaos can be practically neglected (see details in (18)).

Below we consider another important regime called *selective excitation*. In this regime each pulse acts selectively on a chosen qubit, resulting in a resonant transition. During the quantum protocol, many such resonant transitions take place for different  $p$  pulses, with different values of  $\nu_p = \omega_k$ . The region of parameters for the selective excitation is specified by the following conditions (22),

$$\Omega \ll J \ll a \ll \omega_k. \quad (6.5)$$

The meaning of these conditions will be discussed in next Sections.

### 6.2.3 Absence of quantum chaos in the selective excitation regime

Here, we consider the properties of the stationary Hamiltonian (6.4) in the regime of selective excitation. In order to estimate the critical value of the interaction  $J$ , above which one can expect random properties of eigenstates, one needs to compare the typical value of the off-diagonal matrix elements ( $\Omega/2$ ) with the mean energy spacing  $\delta_f$  for unperturbed many-body states that are directly coupled by these matrix elements. Therefore, the condition for the onset of chaos has the form,

$$\frac{\Omega}{2} > \delta_f \approx \frac{(\Delta E)_f}{M_f}. \quad (6.6)$$

Here  $(\Delta E)_f$  is the maximal difference between the energies  $E_0^{(2)}$  and  $E_0^{(1)}$  corresponding to a specific many-body state  $|1\rangle$ , and all other states  $|2\rangle$  of  $H_0$ , that have non-zero couplings  $\langle 1|V|2\rangle$ . Correspondingly,  $M_f$  is the number of many-body states  $|2\rangle$  coupled by  $V$  to the state  $|1\rangle$ . A further average over all states  $|1\rangle$  should be then performed.

In fact, such a comparison (6.6) is just the perturbation theory in the case of two-body interaction. Strictly speaking, the above condition in a strong sense ( $\Omega \gg \delta_f$ ) means that exact eigenstates consist of many unperturbed ( $V = 0$ ) states. Typically, the components of such compound states can be treated as uncorrelated entries, thus resulting in a random structure of excited many-body states. However, one should note that in specific cases when the total Hamiltonian is integrable (or quasi-integrable), the components of excited states have strong correlations and can not be considered as random, although the number of components with large amplitudes can be extremely large (see details in (18)).

It is relatively easy to estimate  $M_f$  in the regime of selective excitation. Let us consider an eigenstate of  $H_0$ ,  $|1, 0, 0, 0, 1, 0, \dots, 0, 0, 1, 0\rangle$ , as a collection of 0's and 1's that correspond to  $-1/2$  and  $1/2$ -spin values. Since the perturbation  $V$  is a sum of  $L$  terms, each of them flipping one single spin, one gets  $M_f = L$ .

In order to estimate  $(\Delta E)_f$ , let us first consider the action of  $V$  on the  $k$ -th spin, and for each spin compute the relative energy difference between the final and the initial energy. One can find that if the  $k$ -th spin has the value  $1/2$ , there are four possible configurations of neighbor spins coupled by the perturbation,

$$\begin{aligned} |\dots 0, 1, 0\dots\rangle &\rightarrow |\dots 0, 0, 0\dots\rangle, \\ |\dots 1, 1, 1\dots\rangle &\rightarrow |\dots 1, 0, 1\dots\rangle, \\ |\dots 1, 1, 0\dots\rangle &\rightarrow |\dots 1, 0, 0\dots\rangle, \\ |\dots 0, 1, 1\dots\rangle &\rightarrow |\dots 0, 0, 1\dots\rangle. \end{aligned} \quad (6.7)$$

If the  $k$ -th spin has the value  $-1/2$ , there are also four possible different arrangements,

$$\begin{aligned}
|\dots 0, 0, 0\dots\rangle &\rightarrow |\dots 0, 1, 0\dots\rangle, \\
|\dots 1, 0, 1\dots\rangle &\rightarrow |\dots 1, 1, 1\dots\rangle, \\
|\dots 1, 0, 0\dots\rangle &\rightarrow |\dots 1, 1, 0\dots\rangle, \\
|\dots 0, 0, 1\dots\rangle &\rightarrow |\dots 0, 1, 1\dots\rangle,
\end{aligned} \tag{6.8}$$

which are the inverse transitions of (6.7). Correspondingly, the energy changes are determined by the relation,

$$|E_0^{(f)} - E_0^{(i)}| = |\xi_k \pm 2J|, \quad k = 1, \dots, L - 2. \tag{6.9}$$

The analysis for the border spins can be performed in a similar way, and one gets four possible configurations, with the following energy changes,

$$|E_0^{(f)} - E_0^{(i)}| = |\xi_k \pm J|, \quad k = 0, L - 1. \tag{6.10}$$

Summarizing the above findings, and setting for instance  $\nu_p = \omega_0$ , one can conclude that  $(\Delta E)_f$  can be estimated as follows,

$$(\Delta E)_f = \text{Max}(|E_0^{(f)} - E_0^{(i)}|) = \omega_{L-1} - \omega_0 + J. \tag{6.11}$$

As a result, the condition for the onset of quantum chaos can be written in the form,

$$\frac{\Omega}{2} > \frac{(\Delta E)_f}{M_f} = \frac{\omega_{L-1} - \omega_0 + J}{L} = \frac{a(L-1) + J}{L}, \tag{6.12}$$

or

$$\Omega > \Omega_{cr} \simeq 2a + \frac{2J}{L}. \tag{6.13}$$

However, this critical value is outside the range of parameters required to be in the selective excitation regime  $\Omega < a$  (see inequality (6)). Thus, we can conclude that quantum chaos for stationary states can not appear in the selective excitation regime. Note that the analysis is done for a single pulse of a time-dependent perturbation.

#### 6.2.4 Fidelity of a quantum protocol

The analytical results obtained above, show that, during a single electromagnetic pulse, the system can be described by perturbation theory. Indeed, if the matrix elements of perturbation are smaller than the energy spacing between directly coupled many-body states, exact eigenstates can be obtained by perturbation theory. Thus, one can expect that for a series of time-dependent pulses the system evolution can also be treated making use of a perturbative approach.

In what follows, we study the system dynamics by applying a specific set of pulses (quantum protocol) in order to create an entangled state for remote qubits (with  $k = 0$  and  $k = L - 1$ ) starting from the ground state,  $|\psi_0\rangle = |0_{L-1}, \dots, 0_1, 0_0\rangle$  (we omit the subscripts below). Our main interest is in estimating the errors that appear due to unwanted excitations of qubits. We show that these errors can be well understood and estimated on the basis of the perturbation theory developed for our time-dependent Hamiltonian (6.2), in the parameter range where the protocol holds.

### 6.2.5 Selective excitation regime and perturbation theory

Any protocol is a sequence of unitary transformations applied to some initial state in order to obtain a final ideal state,  $|\psi^i\rangle$ . In this model of quantum computer the protocol is realized by applying a number of specific rf-pulses, so that we get a state  $|\psi^r\rangle$  which is, in principle, different from the ideal state  $|\psi^i\rangle$ . The difference between the real state  $|\psi^r\rangle$  and the ideal state  $|\psi^i\rangle$  can be characterized by a *dynamical fidelity*,

$$F = |\langle\psi^i|\psi^r\rangle|^2. \quad (6.14)$$

Note that, in our case, the dynamical fidelity  $F$  does not explicitly depend on a perturbation parameter added in the Hamiltonian (2) in order to get a distorted evolution, as is typically assumed in the study of quantum chaos. Indeed, the real final state is determined by the total Hamiltonian (2),

$$|\psi^r\rangle = \hat{U}(T)|\psi_0\rangle \equiv \prod_{p=1}^P \hat{T} e^{-i \int_{t_{p-1}}^{t_p} H(t) dt} |\psi_0\rangle, \quad (6.15)$$

where  $T = t_p$  is the total time to entangle spins,  $\hat{U}(T)$  is the unitary operator given by the sequence of pulses in the protocol, and  $\hat{T}$  is the usual time-ordered product. Therefore, it is not possible to identify a single perturbation parameter which is responsible for a “wrong” evolution of the system.

The selective excitation regime is characterized by the action of pulses that are resonant with a transition between two energy states which differ for the state (up or down) of one spin only. A close inspection of the time independent Hamiltonian (6.4), defines the region of parameters where the selective excitation of single spins can be performed.

Diagonal elements of Hamiltonian (6.4) are given by the eigenvalues  $E_0^{(i)}$  of  $H_0$ , while non-zero off-diagonal elements are constant and equal to  $-\Omega/2$ . In order to have a resonant transition between two energy states, their energy difference  $\Delta$  has to be zero. On the other side, for each state no more than one resonant transition should be allowed. So, we require the energy differences given by Eqs. (6.9,6.10) to be different from zero, apart from the wanted transition. This leads to the following set of equalities (“fake transitions”),

$$\begin{aligned} J &= a\frac{k}{4} & \text{when } k &= 1, \dots, L-3, \\ J &= a\frac{k}{2} & \text{when } k &= 1, \dots, L-3, \\ J &= ak & \text{when } k &= 1, \dots, L-2, \\ J &= a\frac{k}{3} & \text{when } k &= 1, \dots, L-2, \end{aligned} \quad (6.16)$$

From Eqs.(6.16) it is easy to see that the first “fake” transition appears for  $J_1 = a/4$ , the second for  $J_2 = a/2$  and so on up to the last one for  $J_f = a(L-2)$ . All these resonances can be avoided if we choose  $a \gg 4J$  (due to the resonance finite width the condition  $a > 4J$  is not sufficient).

Transitions can be defined according to their energy difference  $\Delta$ ,

- 1) *resonant transitions*,  $\Delta = 0$ ;
- 2) *near-resonant transitions*,  $\Delta \sim J$ ;
- 3) *non-resonant transitions*,  $\Delta \sim a$ .

For  $a \gg 4J$ , each state can undergo one resonant or near-resonant transition only, and many non-resonant ones. The latter can be neglected if we choose  $a \gg \Omega$ . Under these conditions

we can form couples of states, connected by resonant or near-resonant transitions, and we can rearrange the Hamiltonian matrix (6.4) by  $2 \times 2$  block matrices representing all resonant and near-resonant transitions. In this way the dynamical evolution of the system can be described as a two-state problem.

Using this procedure, the entire sequence of pulses can be evaluated. Note that special attention has to be paid to an additional phase shift that arises between any two pulses, due to the change of frame. We remind that the transformation between the rotating and the laboratory frame is given by the expression,

$$|\psi(t)\rangle_{Lab} = e^{i\nu_p t} \sum_k I_k^z |\psi(t)\rangle_{Rot} \quad (6.17)$$

Indeed, let us consider an initial basis state  $|m\rangle$  at time  $t = 0$ , and find the probability for a resonant ( $\Delta = 0$ ) or near-resonant ( $\Delta \sim J$ ) transition to the state  $|p\rangle$  with the energy difference  $E_p - E_m$ . Here  $E_p$  and  $E_m$  are the eigenenergies of the time-independent part of the Hamiltonian (6.2), written in the laboratory frame.

Setting,

$$\psi(t) = \sum_n c_n(t) |n\rangle, \quad (6.18)$$

and  $c_p(0) = 0$ , after the application of a pulse for a time  $\tau$  one gets, in the laboratory frame:

$$\begin{aligned} c_m(\tau) &= c_m(0) [\cos(\frac{\lambda\tau}{2}) + i \frac{\Delta}{\lambda} \sin(\frac{\lambda\tau}{2})] e^{-i\frac{\Delta\tau}{2} - iE_m\tau}, \\ c_p(\tau) &= c_m(0) [i \frac{\Omega}{\lambda} \sin(\frac{\lambda\tau}{2})] e^{i\frac{\Delta\tau}{2} - iE_p\tau}, \end{aligned} \quad (6.19)$$

where  $\lambda = \sqrt{\Omega^2 + \Delta^2}$ .

As we can see, the parameter  $\epsilon$  determined as

$$\epsilon = \frac{\Omega^2}{\Omega^2 + \Delta^2} \sin^2 \left( \frac{\tau}{2} \sqrt{\Omega^2 + \Delta^2} \right) \quad (6.20)$$

characterizes the probability of resonant and near-resonant transitions. In particular, the probability of unwanted near-resonant transitions goes like  $\epsilon$ , and it can be reduced by assuming  $J \gg \Omega$ . Combining all the above expression, we get the condition (6.5).

Correspondingly, the probability for a non-resonant transition (neglecting terms of the order  $1/L$ , and assuming  $a \gg \Omega$ ) is given by the parameter  $\eta$  (23),

$$\eta = \frac{\Omega^2}{4a^2}. \quad (6.21)$$

We would like to stress that even if the ideal state has been constructed taking into account resonant transitions only, our dynamical fidelity is a measure of dynamical errors that are due to near and non-resonant transitions.

Let us now briefly discuss the perturbative approach that is based on recent studies published in Ref.(23). The main idea is that for each  $p$ -th pulse the unperturbed basis can be rearranged in such a way that the Hamiltonian matrix is represented by  $2 \times 2$  block matrices, as described above. This is what we call *unperturbed* Hamiltonian for a specific  $p$ -th pulse. One should note that this *unperturbed* Hamiltonian is  $\Omega$ -dependent. Let us now define by  $\mathcal{V}$  the  $\Omega$ -dependent part which is responsible for non-resonant transition and not described by the  $2 \times 2$  block matrices. Then it is easy to obtain the unperturbed eigenstates,  $|\psi_q^0\rangle$ , and the unperturbed eigenvalues,  $\epsilon_q^0$ , by diagonalizing each of the  $2 \times 2$  blocks independently.

After this step, one can compute the *perturbed* eigenstates by taking into account first order terms only,

$$|\psi_q\rangle = |\psi_q^0\rangle + \sum_{q' \neq q} \frac{\langle \psi_q^0 | \mathcal{V} | \psi_{q'}^0 \rangle}{\epsilon_q^0 - \epsilon_{q'}^0} |\psi_{q'}^0\rangle. \quad (6.22)$$

Note that this perturbative approach is supposed to be valid when Eqs.(6.16) are not satisfied, and when the errors due to near-resonant transitions are much larger than the errors due to non-resonant ones,  $\epsilon \gg \eta$ .

### 6.2.6 Quantum protocol

Let us briefly sketch the algorithm and the particular protocol which was developed in Ref. (22). Starting from the ground state  $|\psi_0\rangle = |0\dots 0\rangle$  and applying a number of specific pulses, we would like to generate the following entangled state,

$$|\psi^i\rangle = \frac{1}{\sqrt{2}} (|0\dots 0\rangle + |10\dots 01\rangle). \quad (6.23)$$

This algorithm could serve, for instance, as the first step for a more general teleportation protocol, and for an implementation of conditional quantum logic operations.

The algorithm can be realized in the following way (for details see Ref. (22)),

$$\begin{aligned} |0, \dots, 0\rangle &\rightarrow (|0, \dots, 0\rangle + |1, 0, \dots, 0\rangle) \\ &\rightarrow (|0, \dots, 0\rangle + |1, 1, 0, \dots, 0\rangle) \\ &\rightarrow (|0, \dots, 0\rangle + |1, 1, 1, 0, \dots, 0\rangle) \\ &\rightarrow (|0, \dots, 0\rangle + |1, 0, 1, 0, \dots, 0\rangle) \\ &\rightarrow \dots \rightarrow (|0, \dots, 0\rangle + |1, 0, \dots, 1\rangle). \end{aligned} \quad (6.24)$$

Physically, the above algorithm can be done by applying suitable *rf*-pulses that are resonant to the desired transitions. The latter are originated from induced Rabi oscillations between the resonant states.

To flip the  $k$ -th spin we have to choose the frequency  $\nu$  of the *rf*-pulse according to the relation  $\nu_p = E_1 - E_2$ , where  $|1\rangle$ ,  $|2\rangle$  are the states involved in the transition and  $E_1$ ,  $E_2$  are the eigenenergies of the time-independent part of Hamiltonian (6.2). For instance, for the first pulse we put,  $\nu_1 = |E_{|1,0,\dots,0\rangle} - E_{|0,\dots,0\rangle}|$ , and we have to apply it for a time  $t_1 = \pi/2\Omega$  to get equal superposition of the states involved in the transition. For other pulses we require that the first state ( $|0, \dots, 0\rangle$ ) remains the same (apart from an additional phase), while the second state flips the  $k$ -th spin. In other words, the probability of unwanted states is due to non-resonant transitions of both states of the r.h.s of Eq.(6.24), and to near-resonant ones of the first state only. Specifically, the state  $|0, \dots, 0\rangle$  undergoes near-resonant transitions with  $\Delta = 2J$  for each pulse, except the first one which is resonant, and the forth for which  $\Delta = 4J$ . Also, at each pulse the state  $|0, \dots, 0\rangle$  get an additional phase, see eqs. (6.19). We took them into account in the definition of the ideal state, see details in Section (6.2.7).

Since in the selective excitation regime we have  $\epsilon \gg \eta$ , contributions from near-resonant transitions are much larger than the ones due to non-resonant transitions. Our algorithm consists of  $2L - 2$  separate pulses, therefore, some modifications are necessary in order to be able to control small unwanted probability. For the product of probabilities this implies  $2L\epsilon < 1$  and  $2L\eta < 1$ , or,

$$\frac{\Omega}{J} \ll \sqrt{\frac{2}{L}}, \quad \frac{\Omega}{a} \ll \sqrt{\frac{2}{L}} \quad (6.25)$$

for  $L \gg 1$ .

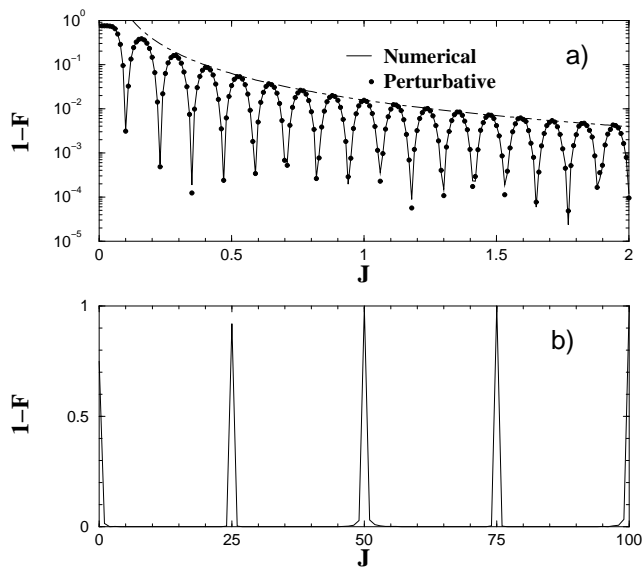


Figure 6.2: The dependence  $1 - F$  is shown as a function of the Ising coupling  $J$  for  $L = 6$  spins,  $\Omega = 0.118$  and  $a = 100$ . Full line represents the numerical data for the dynamical fidelity  $F$  defined by Eq.(6.14), and obtained from direct numerical computation of the system evolution. (a) Full circles stand for perturbative calculations, and full curve corresponds to numerical results. (b) The same numerical results as in (a), but for a larger range of  $J$ . The theoretical expression as given by Eq.(6.32) is also shown in (a).

Before discussing our numerical results we would like to stress that in contrast to what is mainly considered in the literature, the time for our dynamical fidelity is not an independent variable. Indeed, the length of the protocol is determined by the total number of qubits,  $L$ . Specifically,  $2L - 2$  pulses are necessary in order to create the entangled state, so that the protocol time  $T$  is proportional to the number of qubits.

### 6.2.7 Dynamical fidelity: theory and numerical data

Quite unexpectedly, the dynamical fidelity (14) increases with an increase of the Ising coupling  $J$ , as soon as  $J \ll a/4$ . Indeed, on one side the probability of unwanted near-resonant transitions is proportional to  $\epsilon \sim (\Omega/J)^2$  (see Eq.(6.20) where  $\Delta \sim J$  for near-resonant transitions). Therefore, the larger is  $J$ , the smaller is the probability of non-resonant transitions, and the larger is the dynamical fidelity  $F$ .

In Fig.6.2 we show how the dynamical fidelity (6.14) depends on the inter-qubit interaction  $J$ . For convenience, the function  $1 - F$  is shown here and below, instead of  $F$ . Numerical data have been obtained in two different ways. Full curve corresponds to exact computation of the time-dependent Hamiltonian (6.2). Data in Fig.6.2a are compared with those obtained from the perturbative approach explained above.

Apart from very strong peaks (see Fig.6.2b) for which the dynamical fidelity vanishes, one can say that the global tendency is an improvement of the dynamical fidelity for larger values of  $J$ . However, strong oscillations occur reflecting a resonant nature of the dynamics of our system. Perfect agreement between perturbative results and numerical data is found for very large variations of the interaction strength  $J$ .

High peaks for  $1 - F$ , clearly seen in Fig.6.2b, occur for those  $J$ -values given by Eqs.(6.16), where quantum algorithm fails. Thus, one should avoid these situations in a quantum compu-

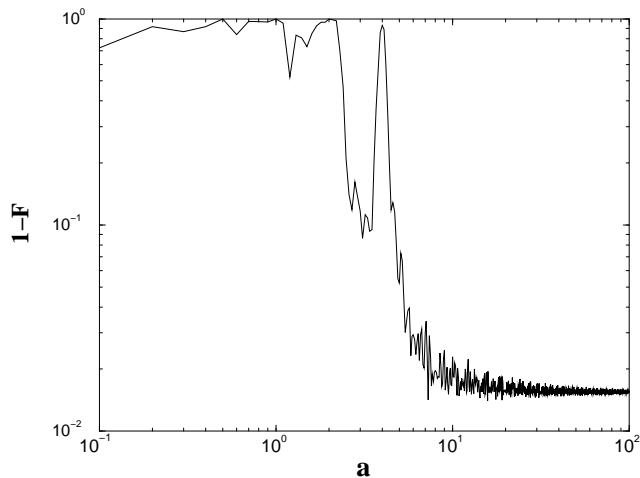


Figure 6.3: The dependence  $1 - F$  as a function of the gradient of a magnetic field is shown for  $L = 6$  spins,  $\Omega = 0.118$  and  $J = 1$ . As one can see, for  $a < 4J$  the fidelity is not as good as for  $a > 4J$ .

tation.

As for the minima in Fig.6.2a for which the dynamical fidelity is close to one, they occur when  $\epsilon = 0$ , or, when

$$J = \frac{\Omega}{2} \sqrt{4k^2 - 1},$$

where  $k$  is an integer number. This relation corresponds to the  $2\pi k$ -condition (22; 23; 26).

Let us now explore the dependence of the dynamical fidelity on the parameter  $a$  which is proportional to the gradient of the external magnetic field,  $a = \gamma \Delta x (dB^z(x)/dx)$ , where  $\Delta x$  is the distance between neighboring qubits (below, we shall refer to the parameter  $a$  as to the magnetic field gradient). Numerical data for the dependence of  $1 - F$  on  $a$  are presented in Fig.6.3. One can see that the dynamical fidelity is getting better for large enough values of  $a$ . We already mentioned that for  $a < 4J$  a problem may arise in the protocol due to “fake” transitions. On the other side, in the regime  $a \gg 4J$  the dynamical fidelity reaches an asymptotic value which depends on  $J$  and  $\Omega$  only, see Fig.6.3.

It is also important to understand the dependence of the dynamical fidelity on the Rabi frequency  $\Omega$ . The data manifest two specific properties demonstrated in Fig.6.4. The first one is a global decrease of the dynamical fidelity with an increase of  $\Omega$ . The second peculiarity is due to strong oscillations that occur for  $\epsilon = 0$ , namely for those  $\Omega$  values corresponding to the  $2\pi k$ -conditions,

$$\Omega_k = \frac{2J}{\sqrt{4k^2 - 1}}. \quad (6.26)$$

For  $\Omega$  values, near-resonant transitions vanish, and non-resonant transitions remain only. Thus, the dynamical fidelity has maxima which provides, in principle, the best condition for a quantum computation.

Nevertheless, let us consider the values of  $\Omega$  that correspond to maxima in Fig.(6.4). This we do in order to make an estimate in the worst possible condition for quantum computation. A brief analysis of the fidelity for the specific values  $\Omega = \Omega_k$  will be sketched in the last subsection. As one can see, for values of  $\Omega$  different from  $\Omega_k$ , the “average” dynamical fidelity increases when the Rabi frequency decreases. This is due to the fact that the probability to generate unwanted states (due to both non-resonant and near-resonant transitions), is proportional to

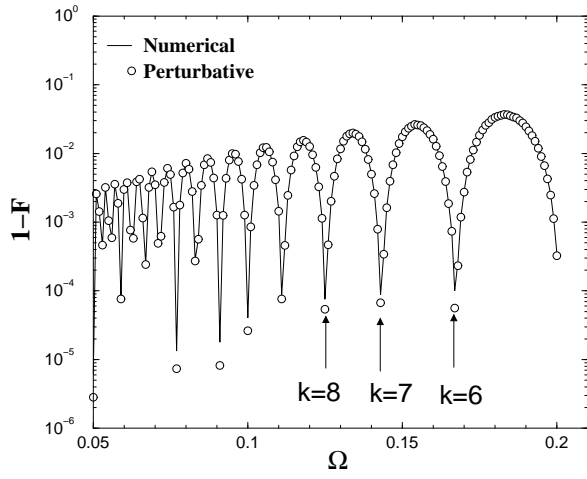


Figure 6.4: The difference  $1 - F$  as a function of the Rabi frequency  $\Omega$  for  $L = 6$  spins,  $J = 1$  and  $a = 100$ . Full curve is the result of direct numerical simulation, circles are obtained from the perturbative approach described in the text. Arrows show few resonant values of  $\Omega$  given by Eq.(6.26).

$(\Omega/\Delta)^2$ . Therefore, the smaller is  $\Omega$  the more reliable the algorithm is. Note that the agreement with the perturbative approach is excellent.

On the other hand, we cannot choose an extremely small value of  $\Omega$  since it implies a large time duration of the pulse ( $\tau \sim \pi/\Omega$ ). Note that the total time for a quantum protocol should be kept well below the decoherence time (the latter can be quite large for nuclear spins (27)). Taking that into account, an optimal choice is to choose the largest possible value,  $\Omega = \Omega_2 = 2J/\sqrt{15} < J$ , and large enough value of  $a$  (in order to significantly suppress the non-resonant transitions).

### 6.2.8 Fidelity: dependence on the number of qubits

Finally, we studied the dependence of the dynamical fidelity on the number  $L$  of spins in the chain. As was noted before, for a chosen protocol its length is proportional to  $L$ . Numerical data clearly manifest a linear decrease of the dynamical fidelity with the number of qubits, see Fig. (6.5).

Let us give now a brief analytical derivation of the dependence of fidelity on the number of qubits.

Given the real and the ideal final state:

$$|\psi^r\rangle = \sum_k c_k^r |\psi_k\rangle, \quad |\psi^i\rangle = c_0^i |0\dots 0\rangle + c_1^i |10\dots 01\rangle$$

and using Eq.(6.14), we have :

$$F = |c_0^{i*} c_0^r + c_1^{i*} c_1^r|^2 \quad (6.27)$$

In Eq.(6.27) the ideal coefficients are given by

$$\begin{aligned} c_0^i &= \frac{1}{\sqrt{2}} e^{i\theta_0^i} = \frac{1}{\sqrt{2}} e^{-iE_0 T} \\ c_1^i &= \frac{1}{\sqrt{2}} e^{i\theta_1^i} = \frac{1}{\sqrt{2}} i^P e^{-i \sum_{p=1}^P E_p (t_{p+1} - t_p)} \end{aligned} \quad (6.28)$$

where  $T$  is the total protocol time and  $P = 2L - 2$  is the number of pulses,  $E_0$  and  $E_p$  are the eigenenergies of the time-independent part of Hamiltonian (6.2). Specifically  $E_p$  are the eigenenergies of the intermediate states, as given by (6.24), and  $t_{p+1} - t_p$  is the duration of the  $p$ -pulse ( $t_{p+1} - t_p = \pi/(2\Omega)$  if  $p = 1$  and  $t_{p+1} - t_p = \pi/\Omega$  if  $p \neq 1$ ).

In the same way we define,

$$c_0^r = \rho_0 e^{i\theta_0^r}, \quad c_1^r = \rho_1 e^{i\theta_1^r}.$$

with the above definitions the fidelity becomes,

$$F = \frac{1}{2}[\rho_0^2 + \rho_1^2 + 2\rho_0\rho_1 \cos(\Delta\theta_0 - \Delta\theta_1)] \quad (6.29)$$

where  $\Delta\theta_0 = \theta_0^r - \theta_0^i$ , and  $\Delta\theta_1 = \theta_1^r - \theta_1^i$ .

The ideal state is defined by resonant transitions only, as explained in section 6.2.5, and Eqs.(6.28) are easily obtained from Eqs.(6.19).

On the other side the real state differs from the ideal one because of the errors due to non-resonant and near-resonant transitions. In particular the coefficient  $c_1^r$  differs from the coefficient  $c_1^i$  because of errors due to non-resonant transitions only, while  $c_0^r$  differs from  $c_0^i$  because of errors due to both non-resonant and near-resonant transitions.

Since we neglect non-resonant transitions ( $\eta \ll 1$ ) we can put  $c_1^r = c_1^i$ .

Differently, near-resonant transitions will act on  $c_0^r$  only, giving a change in both its modulus and phase.

The change of phase  $\alpha$ , in one pulse, for a near-resonant transition, can be obtained from Eqs.(6.19):

$$\alpha = \arctan \left[ \frac{\Delta}{\lambda} \tan\left(\frac{\lambda\tau}{2}\right) \right] - \frac{\Delta\tau}{2};$$

therefore, for  $2L - 3$  pulses (since during the first pulse no near-resonant transitions occur), we have

$$\Delta\theta_0 = (2L - 3)\alpha. \quad (6.30)$$

Accordingly, we can define in a different way the ideal state, changing the phase of  $c_0^i \rightarrow c_0^i \exp[i(2L - 3)\alpha]$ , in order to have  $\Delta\theta_0 = 0$ .

Let us notice that any phase shift between the states  $|0\dots 0\rangle$  and  $|10\dots 01\rangle$  we can be eliminated applying two additional pulses.

From Eqs.(6.19) we can also evaluate the error on the modulus of the coefficient  $c_0^r$ . The probability for the state  $|0\dots 0\rangle$  to make a transition to an unwanted state is determined by the parameter  $\epsilon$ , see Eq.(6.20). In this way, at the end of the protocol, we have  $|c_0^r|^2 = \frac{1}{2}(1 - \epsilon)^{(2L-3)}$ .

Assuming  $(2L - 3)\epsilon \ll 1$ , we can write:

$$\rho_0 \sim \frac{1}{\sqrt{2}} \left[ 1 - (2L - 3)\frac{\epsilon}{2} \right]$$

In this way Eq.(6.29) becomes:

$$F \sim 1 - (2L - 3)\frac{\epsilon}{2}. \quad (6.31)$$

Since  $\epsilon \sim \Omega^2/4J^2$ , we get:

$$F \sim \left( 1 + \frac{3\Omega^2}{8J^2} \right), - \left( \frac{\Omega^2}{4J^2} \right) L \quad (6.32)$$

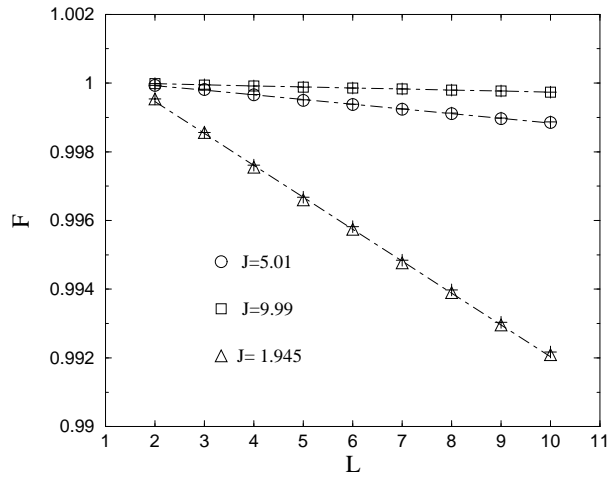


Figure 6.5: The dynamical fidelity as a function of the number  $L$  of spins, for different  $J$  values and  $\Omega = 0.118$ ,  $a = 100$ . Numerical data (triangles for  $J = 1.945$ , circles for  $J = 5.01$  and squares for  $J = 9.99$ ) are compared with the results from the perturbation theory (crosses). Also shown are the best linear fits (dot-dashed lines).

which implies a linear decrease of the dynamical fidelity with an increase of the number of qubits,  $L$ . The slope is given by the parameter:

$$m_{th} = -\frac{\Omega^2}{4J^2}. \quad (6.33)$$

Of course, the above derivation is valid far from the “fake” transitions, Eq.(6.16), and under the conditions Eqs.(6.5, 6.25).

Slopes in Fig. 6.5 have been obtained by a standard linear fit and then compared with the theoretical ones  $m_{th}$ , see Fig. 6.6.

As one can see, the agreement is very good except for small values of the Ising interaction,  $J \simeq \Omega$ , where the probability of near-resonant transitions becomes large, and the condition  $P\epsilon \ll 1$  is not valid anymore.

Finally let us stress that the phase correction is far from being trivial. Indeed a different behavior of fidelity on the number of qubits is found without such phase correction.

Also note that, even under the  $2\pi k$ -conditions given by Eq.(6.26), for which  $\epsilon = 0$ , (so that there are no errors in modulus caused by near-resonant transitions), a phase-error persists, so that, in order to improve fidelity, the same phase correction is necessary.

### 6.2.9 Optimal algorithm

Choosing  $\Omega$  values as given by Eq.(6.26), one gets that the probability for near-resonant transition is zero,  $\epsilon = 0$ . So, only non-resonant transitions lead to unwanted states. In Fig.(6.7) we show the fidelity as a function of the number of spins  $L$  for  $\Omega_k = 0.1216$ . These data should be compared with the analogous ones indicated by triangles in Fig.(6.5).

As one can see, despite the closeness of these two  $\Omega$  values (less than 3% of difference), the fidelity increases in two order of magnitude (see different scales on the  $y$ -axis). It is clear that such preferred  $\Omega$  values should be chosen in any practical implementation of the algorithm. However, due to the high instability of such resonant values, see Fig.(6.4), a detailed analysis can

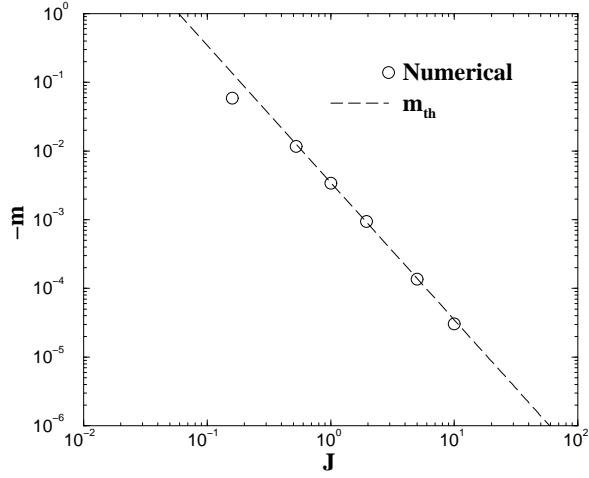


Figure 6.6: Comparison between theoretical and numerical linear slopes for the fidelity, as a function of the interaction  $J$ , obtained for  $\Omega = 0.118$  and  $a = 100$ .

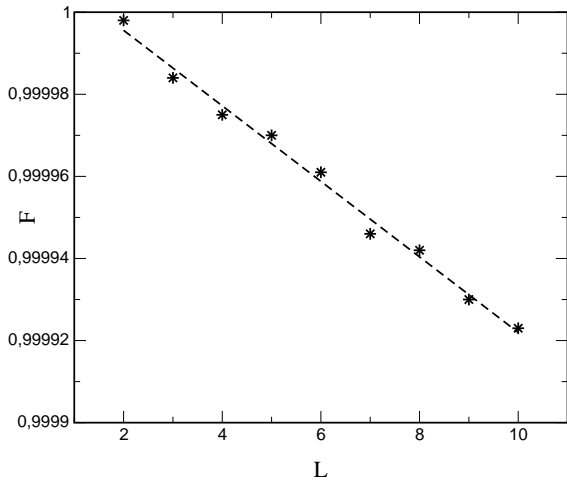


Figure 6.7: The dynamical fidelity as a function of the number  $L$  of spins, for  $J = 1.945$  and  $\Omega_k = 0.1216$ ,  $a = 100$ . Also shown is the best linear fit with the slope  $9.2 \pm 0.3 \times 10^{-6}$ .

only be done within a more general study under the presence of small variations in parameters such as  $\Omega, J, a$ . This study is currently in progress.

### 6.2.10 Conclusions

We have studied the model of a quantum computer consisting of a one-dimensional chain of 1/2-spins (qubits), placed in a time-dependent electromagnetic field. The latter is given by a sequence of  $rf$ -pulses, corresponding to a chosen quantum protocol that allows to generate an entangled state for remote qubits from the initial ground state. Main attention is paid to the analysis of the dynamical fidelity, defined as the overlap of the actual finite state, with the ideal one determined by the quantum protocol.

We considered the region of the selective excitation where the resonant excitations of specific qubits can be implemented by time-dependent pulses. Analytical treatment of the stationary Hamiltonian which describes the evolution of the system during a single pulse, has revealed that in the selective regime the quantum chaos can not appear. Moreover, in this regime a perturbation theory can be applied to all quantities of interest.

Our detailed study of the dynamical fidelity manifests excellent agreement between numerical data and the predictions obtained in the perturbative approach. In particular, we have found how to choose the parameters in order to get the best dynamical fidelity for the creation of the remote entangled state. Specific attention has been paid to the dependence of the dynamical fidelity on the number  $L$  of qubits. We show, both analytically and numerically, that the dynamical fidelity decreases linearly with an increase of  $L$ , and we give an analytical estimate for the slope of this dependence.

## 6.3 Stability of the quantum Fourier transformation on the Ising quantum computer

### 6.3.1 Introduction

Quantum information theory (28) is a rapidly evolving field. It uses quantum systems to process information thereby achieving things not possible with classical resources only. Quantum secure communication for instance is already commercially available. Quantum computation on the other hand is still far from being useful. Two serious obstacles to overcome in building a large quantum computer are: (i) one must be able to control the evolution in order to precisely implement quantum gates, (ii) one must suppress external influences. Errors in both cases are caused by the perturbation of an ideal quantum computer, either by internal imperfections or by coupling to the “environment”. In the present paper we study both kind of errors, in particular their scaling with the number of qubits, in order to envisage the obstacles and demands of building a large quantum computer. We also suggest possible ways to minimize these errors.

We choose a concrete model of a quantum computer and a concrete algorithm. As one of the main things we want to study is the scaling of errors with the size of the computer, we do not limit ourselves to any of the existing experimentally realizable models because their success for large number of qubits is far from guaranteed. We rather choose a simple abstract Ising quantum computer model (IQC) (29), having all the essential properties of some future quantum computer: (i) it is a universal quantum computer, (ii) it is scalable with the number of qubits and (iii) it is one of the simplest models having the first two properties. Multi-qubit gates are possible through the inter-qubit coupling, in fact we choose the simplest possible one, namely nearest-neighbor coupling. The pulses by which we perform quantum gates are not ideal, thereby causing off-resonant transitions. Such unwanted transitions are expected to be a

generic feature of any experimental implementation of a quantum computer. In addition, we also study the influence of external perturbations on the algorithm stability. All these we feel, will be the necessary ingredients of any large quantum computer and we believe our results have relevance beyond the specifics of the IQC model.

For the quantum algorithm we choose to discuss the quantum Fourier transformation (QFT). The first reason to choose the QFT is that it is one of the most useful quantum algorithms, giving an exponential speedup over the best classical procedure known. Furthermore, it is also one of the ingredients of some other important algorithms, e.g. Shor’s factoring algorithm (2). The second reason is that the QFT is a complex algorithm, where by complex we mean it has more than  $\mathcal{O}(n)$  number of quantum gates as opposed to previously studied more simple algorithms where the number of gates scales only linearly with the size of the computer (e.g. entanglement protocol (30)). It is easy to imagine that in most useful quantum algorithms the size of the program will grow faster than linearly with the number of qubits  $n$  and therefore it is important to see how errors accumulate in such algorithms. This importance is confirmed by our results showing that errors due to unwanted transitions for the QFT grow with the *square* of the number of pulses and not *linearly* as in algorithms with linear  $\mathcal{O}(n)$  number of gates, for a typical initial state.

For the QFT algorithm running on the IQC we analyze errors due to spurious transitions caused by pulses, these we call *intrinsic errors*, and errors due to the coupling with an external “environment”, called *external errors*, modelled by a random hermitian matrix from a gaussian unitary ensemble (GUE) (33). We minimize intrinsic errors by applying some additional pulses to correct most probable errors (32) and by doing this, we are able to suppress intrinsic errors by several orders of magnitude. To suppress external errors due to a GUE perturbation we use a previously proposed improved quantum Fourier transformation (IQFT) (34) which is more stable against GUE perturbations in a certain range of parameters. We analyze in detail the dependence of errors on all relevant parameters. By this analysis we can set the limits between which parameters of the IQC should lay in order to preserve the stability of computation and how this demands change with the size of the quantum computer. In our approach to decrease errors we do not use error correcting codes for the following reasons: we want to remove as many errors as we can on the lowest possible level and second, the intrinsic and particularly multi-qubit external errors are not easily handled by the error correcting codes (see Ref. (36) and references therein).

The outline of the paper is as follows. In section II we repeat the definition of the IQC and in section III we summarize the linear response formalism which is the main theoretical tool for studying fidelity. In section IV we study intrinsic and external errors, first separately and then simultaneously. In the appendix we present the pulse sequences used to implement the QFT and the IQFT algorithms.

### 6.3.2 The Ising quantum computer

The IQC consists of a 1-dimensional chain of  $n$  equally spaced identical spin 1/2 particles coupled by a nearest neighbor Ising interaction of strength  $J$ , such that parallel spins are favored over anti-parallel ones by an energy difference of  $J$  (we set  $\hbar = 1$  throughout the paper). The quantum computer is operated via an external magnetic field having two components. The first one is a permanent magnetic field oriented in the  $z$  direction with a constant gradient which allows the selective excitation of individual spins, while the second one is a sequence of  $T$  circular polarized fields in the  $x$ - $y$  plane (which are called pulses), with different frequencies  $\nu^{(m)}$ , amplitudes (proportional to the Rabi frequencies  $\Omega^{(m)}$ ), phases  $\varphi^{(m)}$  and durations  $\tau^{(m)}$  for the  $m$ th pulse, in which is encoded the protocol. A particular orientation of the register allows to suppress the dipole-dipole interaction between spins (37; 38).

The Hamiltonian of the system is

$$H = -\frac{1}{2} \sum_{l=0}^{n-1} \omega_l \sigma_l^z - \frac{J}{2} \sum_{l=0}^{n-2} \sigma_l^z \sigma_{l+1}^z - \sum_{m=1}^T V^{(m)}(t) \Theta^{(m)}(t) \quad (6.34)$$

with

$$V^{(m)}(t) = \frac{\Omega^{(m)}}{4} \sum_{l=0}^{n-1} (\sigma_l^- \exp\{-i(\nu^{(m)}t + \varphi^{(m)})\} + h.c.), \quad (6.35)$$

where  $\Theta^{(m)}(t)$  is equal to one during the  $m$ th pulse and zero otherwise,  $\sigma_l^{x,y,z}$  are the usual Pauli operators for  $l$ -th spin and  $\sigma_l^\pm = \sigma_l^x \pm i\sigma_l^y$ . Due to the constant gradient of the permanent magnetic field, the Larmor frequencies depend linearly on  $l$ ,  $\omega_l = (l+1)a$ . By appropriately choosing the energy units we fix  $J = 1$  so the only relevant energy scales are  $\Omega^{(m)}$  and  $a$ . The basis states are chosen such that  $\sigma_l^z |0\rangle_l = |0\rangle_l$ .

We shall introduce the following notation. Let  $P_i^{ac}$  indicate a pulse with frequency  $\nu_i^{ac}$  resonant with the  $i$ -th spin when its neighbors are in states “ $a$ ” and “ $c$ ”. This will induce the resonant transition  $|\dots a_{i+1} b_i c_{i-1} \dots\rangle \rightarrow |\dots a_{i+1} \bar{b}_i \bar{c}_{i-1} \dots\rangle$ , named  $T_i^{ac}$ , if the pulse is a  $\pi$  pulse ( $a, b, c \in \{0, 1\}$ ). Note that for edge qubits, i.e.  $i \in \{0, n-1\}$ , only one superscript is needed.

Operating the IQC in the *selective excitation regime*, i. e.  $\Omega^{(m)} \ll J \ll a$ , allows one to separate transitions induced by pulses into three sets: *resonant*, *near-resonant* and *non-resonant* according to the detuning  $\Delta$  of the transition which is the difference between the frequency of the pulse and the energy difference of the states involved in the transition. If  $\Delta$  is exactly equal to zero, the transition is called resonant ( $T_i^{ac}$  induced by the pulse  $P_i^{ac}$ ), if  $\Delta$  is of the order of  $J$  it is called near-resonant ( $T_i^{a'c'}$  induced by the pulse  $P_i^{ac}$  with  $\{a', c'\} \neq \{a, c\}$ ), and if  $\Delta$  is of the order of  $a$  it is called non-resonant transition ( $T_i^{a'c'}$  induced by the pulse  $P_i^{ac}$  with  $i' \neq i$ ). In the implementation of a protocol resonant transitions are the ones wanted, while near-resonant and non-resonant transitions are a source of error.

In the two level approximation (37), a given unwanted transition with detuning  $\Delta$  is induced with probability

$$p = \frac{\Omega^2}{\Omega^2 + \Delta^2} \sin^2 \left( \rho \frac{\pi}{2} \sqrt{1 + \frac{\Delta^2}{\Omega^2}} \right), \quad (6.36)$$

where  $\rho$  is the dimensionless duration of the pulse (e. g. for a  $\pi$  pulse  $\rho = 1$  and for  $\pi/2$  pulse it is  $1/2$ ). The most probable unwanted transitions are the near-resonant ones and these can be suppressed by a generalized  $2\pi k$  method as briefly described in the next paragraph.

For  $P_i^{10}(= P_i^{01})$  pulses all near-resonant transitions have the same detuning  $\Delta$  and the transition probability  $p$  will be zero, provided we set the Rabi frequency to

$$\Omega = \frac{\Delta}{\sqrt{4k^2 - 1}}, \quad (6.37)$$

with  $k$  an integer. Since for near-resonant transitions  $\Delta = \mathcal{O}(J)$ , the Rabi frequency is for all pulses of the order of  $\Omega \approx J/k$ . On the other hand, for  $P_i^{00}$  and  $P_i^{11}$  pulses the near-resonant transitions have two different detunings. Therefore it is impossible to suppress both transitions with a single pulse. This problem can be overcome adding an additional correcting  $P_i^{10}$  pulse. The combination of these pulses in order to suppress all near-resonant transitions is called a  $Q$ -pulse denoted by  $Q_{i\rho}^{ac}$  when doing a  $\rho\pi$  rotation of the  $i$ th qubit if neighbors are in states “ $a$ ” and “ $c$ ”. This method to eliminate all near-resonant transitions is called the generalized  $2\pi k$  method and is the best known procedure to induce transitions on the IQC. We refer the interested reader to Ref. (32) for further details. Previous study of Shor’s algorithm on the

IQC (31) did not use this method.  $Q$ -pulses are the basic building blocks of gates, which in turn are the building blocks of algorithms such as the QFT and the IQFT.

The QFT for  $n = 4$  qubits can be written as

$$U_{QFT} = T A_0 B_{01} B_{02} B_{03} A_1 B_{12} B_{13} A_2 B_{23} A_3. \quad (6.38)$$

There are in total  $n$  Hadamard gates ( $A_j$ ),  $n(n-1)/2$  two-qubit  $B$  gates,  $B_{jk} = \text{diag}\{1, 1, 1, \exp(i\theta_{jk})\}$  with  $\theta_{jk} = \pi/2^{k-j}$ , and one transposition gate  $T$  which reverses the order of qubits (e.g.  $T|001\rangle = |100\rangle$ ). In total there are  $n(n+1)/2 + 1$  gates. The IQFT algorithm (34), which is more stable in the presence of GUE perturbations, for  $n = 4$  qubits is

$$U_{IQFT} = T A_0 R_{01} R_{02} R_{03} G_{01} G_{02} G_{03} \\ \times A_1 R_{12} R_{13} G_{12} G_{13} A_2 R_{23} G_{23} A_3, \quad (6.39)$$

where  $G_{ij} := R_{ij}^\dagger B_{ij}$ . The  $R$  gate is defined by  $R_{ij}|\dots a_i \dots b_j \dots\rangle := (-1)^{b_j} |\dots a_i \dots (\bar{a}_i \oplus b_j) \dots\rangle$ . In total there are  $n^2 + 1$  gates in the IQFT, i.e. roughly two times as many as for the QFT.

Each gate for the QFT or the IQFT (Eqs. (6.38) and (6.39)) must in turn be implemented by several pulses (see appendix). The number of pulses for the QFT grows as  $\sim 18n^3$  whereas it grows as  $\sim 54n^3$  for the IQFT. This number can become very large, e.g. for the IQFT and  $n = 10$  one has 44541 pulses.

Note that the implementation of quantum gates on the IQC is easier in the interaction picture since one can ignore large phases arising from the free evolution. Here interaction picture is defined by the transformation  $\psi_{\text{int}} = \exp(-iH_0 t)\psi_{\text{sch}}$  where  $H_0$  is time-independent part of the Hamiltonian  $H$  (6.34) and  $\psi_{\text{sch}}$  is the usual solution of time-dependent Schrödinger equation with the full Hamiltonian  $H$ , i.e. the Schrödinger picture \*. Therefore, pulse sequences used in the paper implement the intended gates in the interaction picture,

Throughout the paper our basic unit of time will be either a gate (as written for instance in Eqs. (6.38) and (6.39)) or a pulse. A single exception will be the paragraph discussing correlation function of intrinsic errors, where the basic unit is a  $Q$ -pulse, which is composed of one or two pulses. The reason is that  $Q$ -pulses are the smallest unit of time, for which near-resonant transitions can be completely suppressed.

### 6.3.3 Linear Response theory

As a criterion for stability we shall use the fidelity  $F(t)$ , defined as an overlap between a state  $\psi(t)$  obtained by the evolution with an ideal algorithm and  $\psi_\delta(t)$  obtained by the perturbed evolution:

$$F(t) = |\langle \psi_\delta(t) | \psi(t) \rangle|^2, \quad (6.40)$$

where  $|\psi(t)\rangle = U(t)|\psi(0)\rangle$  and  $|\psi_\delta(t)\rangle = U^\delta(t)|\psi(0)\rangle$ . To simplify matters we shall assume time  $t$  to be a discrete integer variable, denoting some basic time unit of an algorithm. The quantity measuring the success of the whole algorithm is the fidelity  $F(t)$  at  $t = T$  where  $T$  denotes the total time. One of the most useful approaches to studying fidelity is using the linear response formalism in terms of the correlation function of the perturbation, for a review see Ref. (39). This approach has several advantages. First it rewrites the complicated quantity fidelity in terms of a simpler one, namely the correlation function, simplifying the understanding of the fidelity. Second, the scaling of errors with the perturbation strength, Planck's constant and with the number of qubits is easily deduced. Furthermore, as in practice one is usually interested in the regime of high fidelity, linear response is typically enough.

---

\*Even when we add an external perturbation, we will refer to the interaction picture as the one defined here.

First we shall shortly repeat linear response formulas as they will be useful for our discussion later. Let us write an ideal algorithm up to time  $t$  as  $U(t)$

$$U(t) = U_t U_{t-1} \dots U_1, \quad (6.41)$$

where  $U_i$  is the  $i$ -th gate (pulse). If  $t = T$  we have a decomposition of the whole algorithm.

The perturbed algorithm can be similarly decomposed into gates

$$U^\delta(t) = U_t^\delta U_{t-1}^\delta \dots U_1^\delta. \quad (6.42)$$

Each perturbed gate  $U_j^\delta$  is now written as

$$U_j^\delta = \exp(-i\delta V_j) U_j, \quad (6.43)$$

where  $V_j$  is the perturbation of  $j$ -th gate and  $\delta$  is a dimensionless perturbation strength. For any perturbed gate one can find a perturbation generator  $V$ , such that relation (6.43) holds. Observe that the distinction between the perturbation strength  $\delta$  and the perturbation generator  $V$  in Eq. (6.43) is arbitrary. If one is given an ideal gate  $U$  and a perturbed one  $U^\delta$ , one is able to calculate only the product  $\delta V$ . This arbitrariness can always be fixed by demanding for instance that the second moment of the perturbation  $V$  in a given state is equal to one.

To lowest order in  $\delta$ , fidelity can be written as (35)

$$F(t) = 1 - \delta^2 \sum_{t_1, t_2=1}^t C(t_1, t_2), \quad (6.44)$$

where the correlation function of the perturbation is

$$C(t_1, t_2) = \langle V_{t_1}(t_1) V_{t_2}(t_2) \rangle - \langle V_{t_1}(t_1) \rangle \langle V_{t_2}(t_2) \rangle \quad (6.45)$$

with  $V_j(t) = U^\dagger(t) V_j U(t)$  being the perturbation of  $j$ -th gate propagated by an ideal algorithm up to time  $t$ . The brackets  $\langle \cdot \rangle$  denote the expectation value in the initial state. Throughout the paper we average over an ensemble of random gaussian initial states to reduce statistical fluctuations. Note that the time dependence of the correlation function (6.45) is due to two reasons: one is time dependence due to the propagation with the unperturbed Hamiltonian (time index in brackets) and the second one is due to the time dependence of the perturbation itself (time index as a subscript) since one can have different perturbations at different times. Expression (6.44) is the main result of the linear response theory of fidelity. From this one can see that decreasing the correlation sum (or even making it zero, see Ref. (40)) will increase the fidelity. In Ref. (34) stability of the QFT algorithm was considered with respect to static GUE perturbation. Analyzing the correlation function the authors were able to design an improved QFT algorithm (IQFT) which increases fidelity.

We are mainly interested in the fidelity  $F(T)$  at the end of an algorithm. The final time  $T$  in efficient quantum algorithms depends on the number of qubits in a polynomial way, say as  $T \propto n^p$ . The power  $p$  depends on the algorithm considered and of course also on our decomposition of the algorithm into gates (pulses). For the QFT and the IQFT algorithms with decomposition into gates, Eqs. (6.38) and (6.39), one has  $p = 2$ . On the other hand, for the implementation of the QFT on the IQC one needs  $T \propto n^3$  ( $p = 3$ ) basic electromagnetic pulses, as one is not able to directly perform  $B_{jk}$  gates on distant qubits but has to instead use a number of pulses proportional to the distance between the qubits  $|j - k|$ . If the correlation function decays sufficiently fast, the fidelity will decay like  $1 - F \propto \delta^2 n^p$  whereas in the case of slow correlation decay the fidelity will decay as  $1 - F \propto \delta^2 n^{2p}$ . In the extreme case of perturbations

at different times being statistically uncorrelated (very fast decay of correlations)  $\langle V_j V_k \rangle \propto \delta_{jk}$ , one can go beyond the perturbation theory and obtains the exact formula  $F = \exp(-\delta^2 T)$  (34). Therefore, in the limit of a large quantum computer (large  $n$ ) strongly correlated static errors (implying slow decay of correlations) will be dominant. When discussing errors caused by the coupling to the environment we shall focus on static perturbations, meaning the same perturbation on all gates,  $V_k = V_j = V$ , as this component will dominate the large  $n$  behavior.

### 6.3.4 Errors in the quantum Fourier transformation

Errors in an experimental implementation of the QFT algorithm on the IQC can be of three kinds: (i) due to unwanted transitions caused by electromagnetic pulses (ii) due to the coupling with external degrees of freedom and (iii) due to the variation of system parameters in the course of algorithm execution. In the present paper we shall discuss only the first two errors. Errors due to electromagnetic pulses are inherent to all algorithms on the IQC as we are presently unable to design pulse sequences for quantum gates without generating unwanted transitions albeit with small probabilities. This errors can be in principle decreased by going sufficiently deep into the selective excitation regime, but one must keep in mind the limitations of real experiments <sup>†</sup>. Coupling with the “environmental” degrees of freedom is endemic in all implementations of quantum computers. As the environment will usually have many degrees of freedom we shall model its influence on the quantum computer by some effective perturbation  $V_{eff}$  given by a random matrix from a Gaussian unitary ensemble (GUE) (33). Note that the coupling with the environment will generally cause non-unitary evolution of the central system. We expect quantum computation to be stable only on a time scale where the evolution of the quantum computer is approximately unitary, i.e. for times smaller than the non-unitarity time scale. Therefore we limit ourselves to *unitary* external perturbations. The third kind of errors due to the variation of system parameters, e.g. variation of Larmor frequencies due to changes of the magnetic field are not considered in this paper. This does not mean they are not important. Let us consider a systematic error in the gradient of the magnetic field throughout the protocol ( $a \rightarrow a + \delta a$ ). Demanding that the error in the largest eigenphase at the end of the algorithm is much smaller than 1, one gets the condition  $a/\delta a \approx an^{p+2}/\Omega$ . If one is in the selective excitation regime, this ratio can become very large and this puts stringent demands on experiment.

To ease understanding we shall first discuss intrinsic errors only, then external ones and finally both combined.

### 6.3.5 Intrinsic Errors

For near-resonant and non-resonant transitions we have  $\Delta \gg \Omega$  and the probability given by perturbation theory is  $p \propto (\Omega/\Delta)^2$ . In the  $2\pi k$  method the Rabi frequency  $\Omega$  is approximately  $J/k$  (see Eq. 6.37) so the probabilities for near-resonant ( $\Delta \sim J$ ) and non-resonant ( $\Delta \sim a$ ) transitions are

$$\begin{aligned} p^{near} &\propto \left(\frac{1}{k}\right)^2 \\ p_{jl}^{non} &\propto \left(\frac{J}{ka(j-l)}\right)^2, \end{aligned} \tag{6.46}$$

respectively.  $p_{jl}^{non}$  denotes the probability of a non-resonant transition with  $\Delta \approx a|j-l|$  involving the  $j$ -th spin (resonant with the transition) and the  $l$ -th spin (erroneously flipped due to the

---

<sup>†</sup>A new method for dealing with intrinsic errors has been proposed recently in Ref. (41)

unwanted transition). The dependence of near and non-resonant errors on system parameters is therefore different.

In pulse sequences implementing the QFT or the IQFT we always use the generalized  $2\pi k$  method by which one can get rid of all near-resonant transitions. Therefore the only errors that remain are non-resonant ones. We first checked numerically that this is indeed the case by studying dependence of errors on system parameters by which one is able to distinguish near and non-resonant errors, Eq. (6.46).

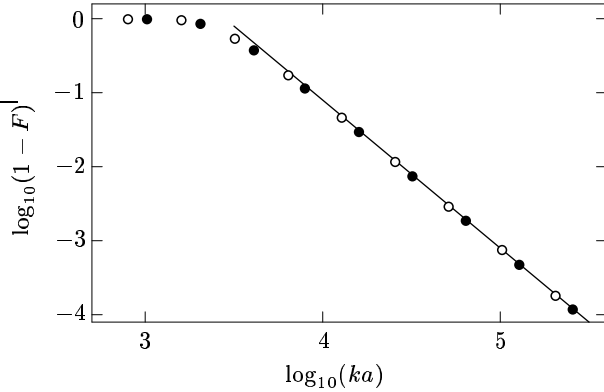


Figure 6.8: Dependence of fidelity for the QFT on physical parameters of the system. Empty points indicate variation of  $k$  with  $a = 100$  and filled points indicate variation of  $a$  with  $k = 128$ , both for  $n = 6$ . Full line is the theoretical dependence of  $p^{non}$  on system parameters given by Eq. (6.46). The agreement with the theoretical dependence confirms that the only errors left are non-resonant ones.

One can observe from Fig. 6.8 that agreement with the theoretical  $p^{non}$  (Eq. (6.46)) is excellent thereby confirming that the only errors left are the non-resonant ones. By using the generalized  $2\pi k$  method we therefore decreased intrinsic errors by a factor of  $(a/J)^2$  as compared to ordinary  $2\pi k$  method where there are still some near-resonant errors present. In order to have a complete understanding of fidelity decay due to intrinsic errors we have to understand scaling of these with the number of qubits. As we already discussed in section 6.3.3 this depends on two things: how strong the errors are correlated, giving possible scalings from  $n^p$  to  $n^{2p}$  and on the dependence of the perturbation strength with the number of qubits. Let us first discuss the later.

Under the assumption that the average transition probability (i.e. perturbation strength) for a non-resonant transition is the sum of all possible non-resonant transitions averaged over all possible resonant qubits, we can estimate

$$\delta^2 \propto \frac{1}{n} \sum_{j \neq l=0}^{n-1} p_{jl}^{non} \quad n \rightarrow \infty \quad \left[ \frac{J}{ka} \right]^2 \left( \frac{\pi^2}{3} - \alpha \frac{\log n}{n} \right), \quad (6.47)$$

with  $\alpha$  some  $n$  independent constant. We can see that the perturbation strength approaches a fixed value as  $n$  grows, but the convergence to its limit is logarithmically slow. For small  $n$  the perturbation strength therefore will grow with  $n$  whereas it will saturate for large  $n$ .

The second contribution to the  $n$ -dependence of fidelity comes from the dynamical correlations between errors given by the correlation function (6.45) of the perturbation generator for non-resonant errors. We numerically calculated this correlation function in order to understand how the correlation sum and therefore fidelity behave as a function of  $n$ .

In Fig. 6.9 we show  $C(t_1, t_2)$  averaged over all Hilbert space. One can see that there are large 2-dimensional regions of high correlations in all parts of the picture. Thus there are strong

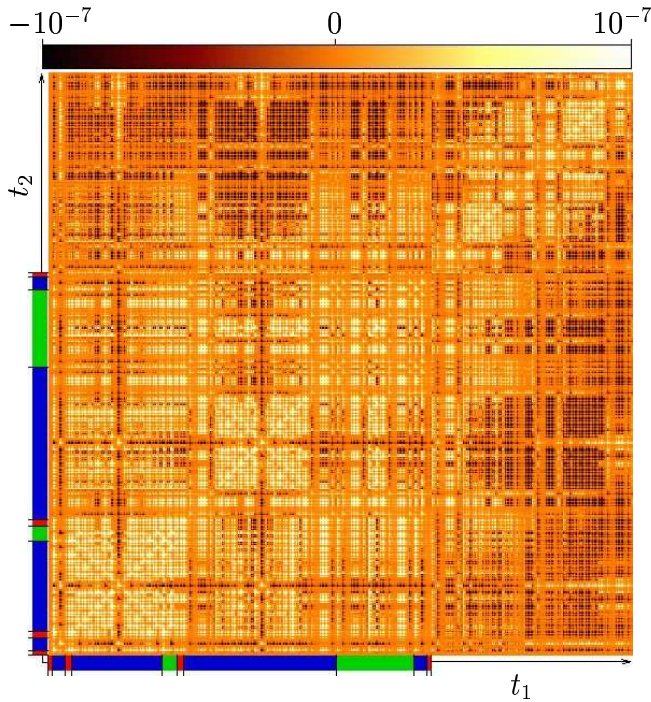


Figure 6.9: (Color online) Correlation function for intrinsic errors in the QFT for  $k = 128$ ,  $a = 100$  and  $n = 4$ . The shading on the time axes denotes the duration of different gates, Eq. (6.38), and the time going from 1 to 543 runs over all  $Q$ -pulses. The light/dark areas give a positive/negative contribution to the fidelity.

correlations between errors at different pulses and therefore the correlation sum will grow as  $\sim n^6$  as the number of pulses scales as  $n^3$  for our implementation of the QFT. Similar results are obtained also for the IQFT as can be inferred from Fig. 6.11. Note that during the application of the transposition gate at the end of the protocol the correlation sum starts to decrease, nicely seen in Fig. 6.10 and also visible in the correlation picture in Fig. 6.9 as there are more negative than positive areas towards the end of the algorithm. This very interesting phenomenon means that applying the transposition gate is advantageous as it will increase fidelity. Note that this would not occur if we would do the transposition operation digitally after the readout. We checked that this principle can not be exploited further by repeating the transposition many times and by this decreasing correlation sum even more. Still, this surprising behavior suggests that it might be possible to decrease non-resonant errors in a systematic way.

To further confirm the predicted  $\sim n^6$  growth of the correlation sum, we calculated the dependence of intrinsic errors on  $n$ . This can be seen in Fig. 6.11, where we plot  $1 - F(T)$  as a function of  $n$  for the QFT and the IQFT, for two different sets of parameters, one for  $k = 128$ ,  $a = 100$  giving large errors and one for  $k = 1024$ ,  $a = 1000$ . One can see that asymptotically for large  $n$  the dependence is indeed  $n^6$  but one needs of the order of  $n = 7$  or more qubits for convergence. This slow convergence we believe is due to the logarithmic convergence of the perturbation strength (Eq. (6.47)). To get exact coefficients in front of  $n^6$  dependence we fitted dependences of errors in Fig. 6.11 with a polynomial in  $n$  using at most two nonzero terms. Defining polynomials in the linear response regime as  $s^{in} = (1 - F)(ka/J)^2$  one gets for the QFT and the IQFT

$$\begin{aligned}
 s_{QFT}^{in}(n) &= 280n^6 - 660n^5 \\
 s_{IQFT}^{in}(n) &= 1300n^6 - 2100n^5.
 \end{aligned}
 \tag{6.48}$$

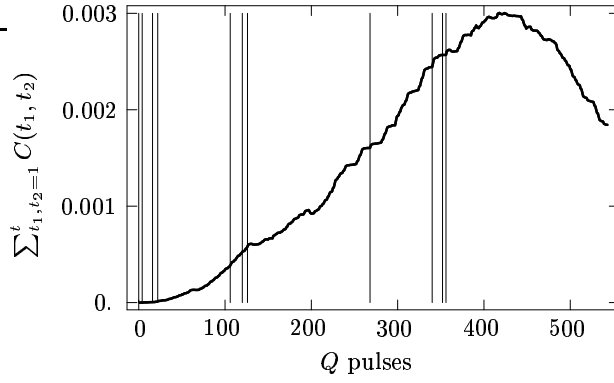


Figure 6.10: The correlation sum of the same data as in Fig. 6.9. Note the decrease of the sum when the transposition gate is applied. The fidelity is in this linear response regime simply given by Eq. (6.44). Vertical lines indicate the beginning of each gate (Eq. (6.38)).

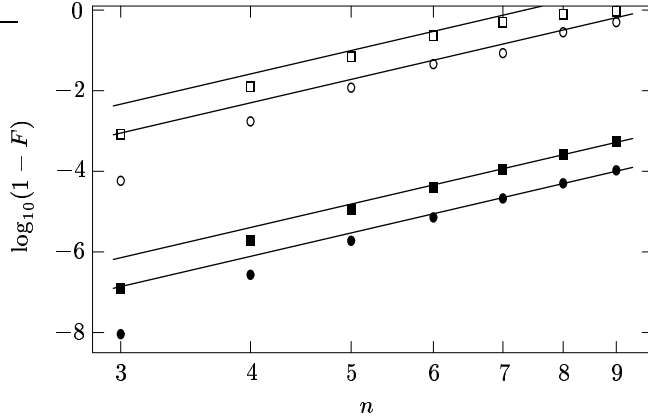


Figure 6.11: Dependence of fidelity on the number of qubits. Empty symbols indicate data for  $k = 128$  and  $a = 100$  while filled symbols are for  $k = 1024$  and  $a = 1000$ . Circles indicate the QFT and squares the IQFT. In the presence of intrinsic errors *only*, the IQFT does not improve fidelity. Full lines show the asymptotic  $n^6$  dependence.

Both expressions are good for  $n \geq 5$  and superscript “*in*” denotes intrinsic errors. Beyond the linear response the exponential dependence is frequently justified (35) and one has

$$F = \exp \left( - \left[ \frac{J}{ka} \right]^2 s^{in}(n) \right). \quad (6.49)$$

The large coefficients of the polynomials in Eqs. (6.48) are due to the large number of pulses. The maximum possible dependence in the case of no decay of the correlation function (see discussion at the end of section 6.3.3) could be  $T^2$  and therefore the leading terms in the polynomials (6.48) expressed in terms of the total number of pulses are  $s_{QFT}^{in} \sim 0.8T_{QFT}^2$  and  $s_{IQFT}^{in} \sim 0.5T_{IQFT}^2$ . Therefore relative to the number of pulses the IQFT slightly decreases non-resonant errors but in the absolute sense the QFT is better simply because it has only one third as many pulses as the IQFT and the coefficient in front of  $n^6$  (Eq. (6.48)) is thereby smaller. If only intrinsic errors in the generalized  $2\pi k$  method are concerned the QFT is always more stable than the IQFT. Note that the intrinsic errors due to non-resonant transitions for the QFT grow as  $\sim T^2$  ( $\sim n^6$ ) whereas in previously studied “simple” algorithms, for instance

the entanglement protocol (30), they grow only as the first power of the number of gates  $\sim T$ . This means that the QFT is much more sensitive to intrinsic errors.

### 6.3.6 External Errors

In order to study external errors only we set throughout this section  $k = 1024$  and  $a = 1000$ , for which the intrinsic errors are much smaller than external ones in the range of qubits and perturbation strength considered.

External errors will be modeled with the perturbation  $V$  (Eq. (6.43)) chosen to be a random hermitian matrix from a GUE ensemble. To facilitate comparison with previous results on the IQFT (34) we shall apply the perturbation after each quantum gate, except for the last transposition gate  $T$  after which we do not apply the perturbation. So for the QFT we apply  $n(n+1)/2$  perturbations, while for the IQFT we apply  $n^2$  perturbations. Other possible choice would be to apply the perturbations after each pulse. We shall discuss this possibility at the end of this section. For now let us just say that qualitatively the results are the same as if doing the perturbation after each gate, one just has to rescale the perturbation strength like  $\delta_{gate} \propto n\delta_{pulse}$  as there are effectively  $\mathcal{O}(n)$  perturbations (pulses) per gate.

From the linear response expression for fidelity we argued that the static perturbations are the worst ones. Thereby, we will consider only static perturbations, i.e. the same perturbation for all gates. As the QFT is implemented in the interaction picture one expects that the worst perturbation has to be static in the interaction picture and not in the Schrödinger. Remember that the transformation between the interaction and the Schrödinger picture is given by a unitary transformation  $W(t) = \exp(-iH_0t)$  generated by the time independent part of the whole Hamiltonian  $H$  in Eq. (6.34),  $\psi_{int}(t) = W(t)\psi_{sch}(t)$ . To verify this we compared the error growth for a static perturbation applied in the interaction picture (i.e. the wave function after one application of error is  $\psi_{int}^\delta = \exp(-i\delta V)\psi_{int}$ ) with the errors for a static perturbation in the Schrödinger picture ( $\psi_{sch}^\delta = \exp(-i\delta V)\psi_{sch}$ ). Let us first consider the later.

If we apply a static perturbation in the Schrödinger picture, we can transform it to the interaction picture by  $W(t)$ . This transformation

$$\exp(-i\delta V_{int}(t)) := W^\dagger(t) \exp(-i\delta V_{sch}) W(t), \quad (6.50)$$

will result in the perturbation in the interaction picture  $V_{int}(t)$  being time dependent. As this transformation involves large phases in the selective excitation regime, perturbations at different gates will tend to be uncorrelated due to averaging of widely oscillating factors in the correlation function (6.45). Therefore, to first approximation one can assume  $C(t_1, t_2) = \delta_{t_1, t_2}$  so the fidelity will decay as  $F(T) = \exp(-\delta^2 T)$  (34). On the other hand, if we select the perturbation to be static in the interaction picture the correlation function will not be a Kronecker delta in time, so the fidelity will decay faster.

To numerically confirm these arguments, we show in Fig. 6.12 the dependence of fidelity on the number of qubits  $n$  for the two cases discussed: static perturbation in the interaction picture and static perturbation in the Schrödinger picture. Polynomial fitting of the  $n$  dependence for the QFT gives

$$\begin{aligned} s_{sch}^{gue}(n) &= 0.47n^2 + 1.41n - 2.42 \\ s_{int}^{gue}(n) &= 0.45n^3 - 0.42n^2 + 0.58n. \end{aligned} \quad (6.51)$$

The fidelity due to external GUE errors is then given as

$$F = \exp(-\delta^2 s^{gue}(n)), \quad (6.52)$$

with the appropriate  $s^{gue}(n)$  from Eq. (6.51). Note that  $s_{int}^{gue}(n)$  grows faster than  $s_{sch}^{gue}(n)$ , thereby confirming our expectations. Observe also that for static perturbations in the Schrödinger picture, using the assumption of completely uncorrelated errors in the interaction picture we predicted  $s_{sch}^{gue} \approx T \approx n^2/2$  for the QFT, which is remarkably close to the numerically observed value  $0.47n^2$  in Eq. (6.51). For the IQFT and the application of GUE perturbation in the Schrödinger picture one gets a similar result with the leading term  $s_{sch}^{gue}(n) \sim 1.12n^2$ . One can write an arbitrary time dependent perturbation in the interaction picture as a Fourier series and for large  $n$  the static component will always prevail. Therefore, from now on we shall exclusively discuss only static perturbations in the interaction picture.

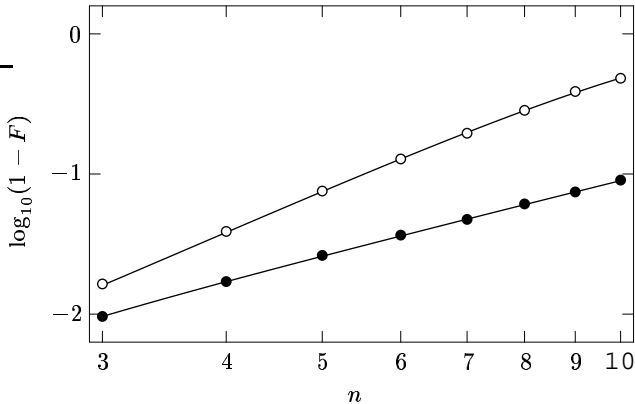


Figure 6.12: Dependence of  $1 - F$  in the QFT algorithm on the number of qubits for static perturbation in the interaction picture (empty points) and in the Schrödinger picture (full points), with  $\delta = 0.04$ . Lines are the best fitting polynomials (see Eq. (6.51)). We can see that static perturbations in the interaction picture are more damaging than static perturbations in the Schrödinger picture.

The dependence of errors due to GUE perturbations in the case of the QFT and the IQFT has already been derived <sup>‡</sup>. For the IQFT numerical fitting in our case gives dependence

$$s_{IQFT}^{gue}(n) = 1.31n^2 + 0.86n - 3.73. \quad (6.53)$$

Dependence of fidelity in both cases can be seen in Fig. 6.13, together with the theoretical prediction (Eq. (6.52)) using the polynomials (6.51) and (6.53).

Observe that the IQFT for  $n > n_{crit} = 3$  is better than the QFT despite having more gates and therefore applying perturbation on it more times (for  $n = 3$  the QFT is slightly better). What is important is that the dependence of errors on  $n$  is also different:  $\sim n^3$  for the QFT, but only  $\sim n^2$  for the IQFT. This means that asymptotically the IQFT is much more stable against GUE perturbations than the ordinary QFT.

Finally, let us discuss what happens if we apply static GUE perturbations after *each pulse*, instead of after each gate as done so far.

Let  $U_j$  denote a single pulse,  $(U_r \dots U_1)$  the whole gate and  $V(j) = (U_j \dots U_1)^\dagger V(U_j \dots U_1)$ . To the lowest order in  $\delta$ , we can rewrite the perturbed gate as

$$\begin{aligned} \exp(-i\delta V)U_r \dots \exp(-i\delta V)U_1 \approx \\ U_r \dots U_1 \exp(-i\delta[V(1) + \dots + V(r)]), \end{aligned} \quad (6.54)$$

<sup>‡</sup>Taking into account the definition of fidelity in Ref. (34), polynomials are almost the same with the slight difference due to the different number of applied perturbations.

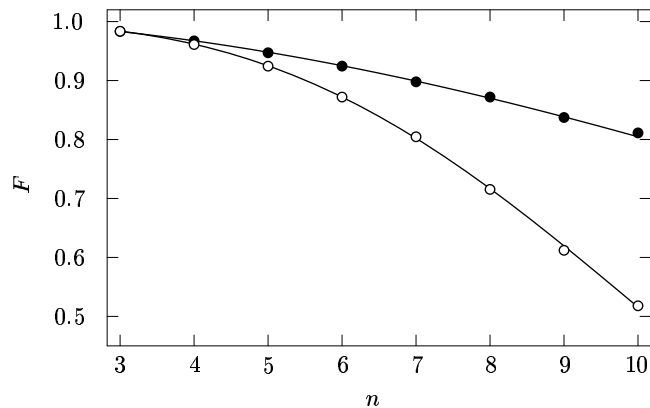


Figure 6.13: Dependence of the fidelity on the number of qubits for the QFT (empty symbols) and the IQFT (filled symbols) algorithms ( $\delta = 0.04$ ). Curves indicate the theoretical prediction Eq. (6.52) using the polynomials from Eqs. (6.53) and (6.51).

where we moved all the perturbations to the beginning of the gate. This means that the application of the perturbation after each pulse is to the lowest order in  $\delta$  *equivalent* to the application of the effective perturbation  $\delta \sum_j^r V(j)$  after the gate. Of course now the perturbation is explicitly time dependent. But individual pulses will do transformations on an exponentially small subspace of the GUE matrix (i.e. on one qubit) and therefore one might expect that effectively  $\sum_j^r V(j) \approx r V_{eff}$ , where  $V_{eff}$  is some effective random matrix independent of the gate and very similar to  $V$ . As in our case of the QFT on the IQC we have on average  $\propto n$  pulses per gate we can predict that applying a perturbation with strength  $\delta_{pulse}$  after each pulse is approximately equal as applying a perturbation of strength  $\delta_{gate} \approx n \delta_{pulse}$  after each gate. In order to confirm these expectations we did numerical experiments with the results shown in Fig. 6.14. Fitting

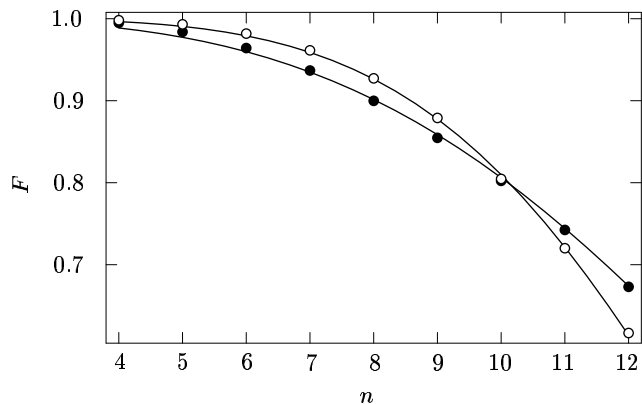


Figure 6.14: Dependence of  $F$  on the number of qubits for the static GUE perturbation after each pulse with  $\delta = 5 \cdot 10^{-4}$ . Empty symbols are for the QFT and filled symbols are for the IQFT. For large  $n$ , the IQFT is again better than the QFT. Curves are the theoretical prediction Eq. (6.52) using the best fitting polynomials given by Eq. (6.55).

polynomial in the dependence of fidelity, Eq. (6.52), for the QFT and the IQFT gives in this case

$$\begin{aligned}
 s_{QFT}^{gue}(n) &= 4.86n^5 + 35.8n^4 \\
 s_{IQFT}^{gue}(n) &= 25.6n^4 + 606n^3.
 \end{aligned}
 \tag{6.55}$$

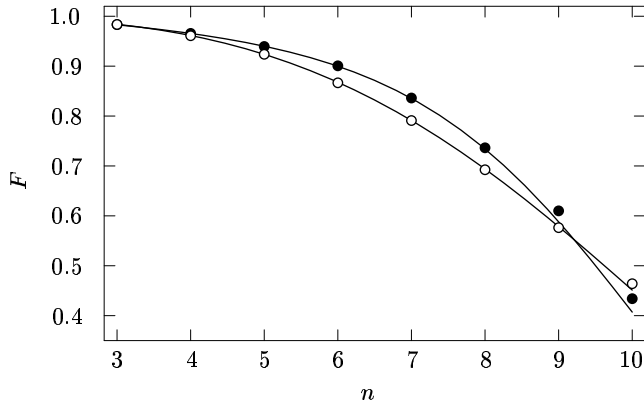


Figure 6.15: Fidelity for the QFT (empty symbols) and the IQFT (filled symbols) algorithm with GUE perturbation after each gate. System parameters are  $k = a = 200$  and  $\delta = 0.04$  (intrinsic and external errors are comparable in size). Full curves are theoretical predictions for  $F$  given by Eq. (6.56). With both errors present, the QFT is always better than the IQFT for large enough  $n$ .

The leading dependence of  $n^5$  for the QFT and  $n^4$  for the IQFT nicely agrees with our rescaling prediction  $\delta_{gate} \approx n\delta_{pulse}$ . The IQFT is asymptotically again better than the QFT as the errors grow slower with the number of qubits. The crossing point between the two in this case happens at  $n_{crit} = 10$ , whereas in the case of perturbation after each gate we had  $n_{crit} = 3$ . This confirms that doing GUE perturbation after each pulse is qualitatively the same as doing it after each gate, only the crossing point between the QFT and the IQFT is shifted. The dependence of errors on  $n$  changes simply due to the different number of applied perturbations. If the perturbation strength  $\delta$  is properly rescaled, the  $n$  dependence is the same in both cases.

Up to now we discussed intrinsic errors and external errors separately. The next question is of course, what happens if both errors are present at the same time and are of similar strength?

### 6.3.7 Intrinsic and External Errors combined

If both kinds of errors are present, a first naive guess would be that they just add,

$$F^{both} = F^{in} F^{gue} = \exp\left(-\left[\frac{J}{ka}\right]^2 s^{in}(n) - \delta^2 s^{gue}(n)\right), \quad (6.56)$$

with the appropriate polynomials  $s^{in}(n)$  and  $s^{gue}(n)$  given in Eqs. (6.48), (6.51) and (6.53). In the linear response regime this formula means that both errors are uncorrelated, i.e. their cross-correlations are zero. This is easy to prove using properties of GUE matrices. Let us calculate the cross-correlation function between intrinsic perturbation,  $V^{in}(t_1)$ , and external perturbation,  $V^{gue}(t_2)$ , averaged over the GUE ensemble. Written explicitly one has to average products of the form  $V_{ij}^{in} V_{jk}^{gue}$ . As this expression is linear in  $V^{gue}$  it averages to zero,  $\langle V_{ij}^{in} V_{jk}^{gue} \rangle_{gue} = 0$ , thereby explicitly confirming a simple addition of both errors. Of course in real experiments we are not averaging over a GUE ensemble but we are taking one definite representative member of it. For large Hilbert space the expectation value of a typical random state and one particular GUE matrix is “self-averaging” and will be equal to the ensemble average.

Let us check the theoretical prediction for fidelity Eq. (6.56) with a numerical experiment. The results together with the theoretical prediction Eq. (6.56) are in Fig. 6.15. The agreement between theory and experiment is good even beyond the linear response regime. Please note

that we deliberately choose parameters such that both the QFT and the IQFT give similar fidelity in order to also see the crossing of the two curves within the shown range of  $n$ . Given a fixed  $\delta$  and  $ka$ , the QFT is always better for large  $n$  because intrinsic errors will prevail over external ones, due to their fast  $n^6$  growth. But still, for intermediate  $n$ 's the IQFT can be better than the QFT as seen in Fig. 6.15.

Equipped with the understanding of errors in the QFT and the IQFT due to external GUE perturbations and intrinsic errors, we can make some predictions regarding ranges of experimental parameters  $ka$ ,  $\delta$ ,  $n$  for which the fidelity will be high enough. An interesting question is, when is the IQFT better than the QFT? Setting  $F_{QFT} = F_{IQFT}$  with  $F$ 's given by Eq. (6.56) results in the condition

$$\delta_{crit} = \frac{J}{ka} \sqrt{\frac{s_{QFT}^{in} - s_{IQFT}^{in}}{s_{QFT}^{gue} - s_{IQFT}^{gue}}}. \quad (6.57)$$

For  $\delta > \delta_{crit}$  the IQFT is better than the QFT. In Fig. 6.16 we show curves of constant fidelity

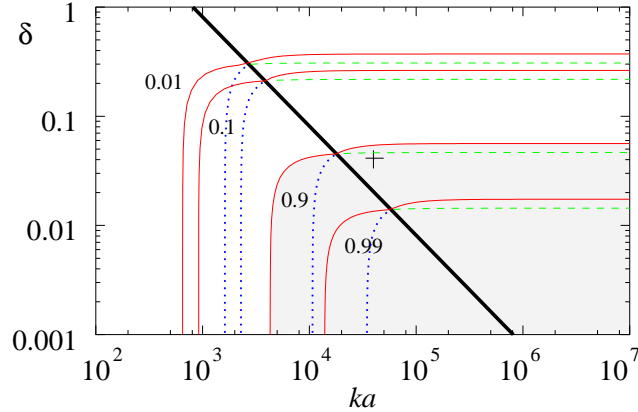


Figure 6.16: (Color online) The dependence of fidelity on system parameter  $ka$  and GUE perturbation strength  $\delta$  for  $n = 5$ . Full curves of constant fidelity are composed of two parts corresponding to the QFT or the IQFT. To the right of the thick line for  $\delta_{crit}$ , the IQFT is better and below the QFT is better. Dotted curves of constant fidelity below this line are for the IQFT and dashed lines above are for the QFT. The shaded region corresponds to the region of fidelity larger than 0.9. The plus symbol shows the position of parameters for Fig. 6.15.

for  $n = 5$ . They are composed of two parts. To the right of the line for  $\delta_{crit}$ , the IQFT is better than the QFT, and vice versa. Two characteristic features are also vertical and horizontal asymptotes of curves of constant fidelity. Vertical asymptotes mean that for a fixed  $n$ , even if  $\delta = 0$ , we must have  $ka$  larger than some critical value determined just by intrinsic errors, in order to have a given fidelity. Horizontal asymptotes for high  $ka$  mean that if  $\delta$  is larger than some critical value, increasing  $ka$  will not help to improve fidelity. In Figs. 6.17 and 6.18 we show similar plots, only now one of the axes gives the dependence on  $n$ . For instance, from Fig. 6.17 one can see that fixing  $ka = 10^5$ , the maximum number of qubits is  $n \approx 12$  if we want to have fidelity larger than 0.9 (even if  $\delta = 0$ ). This unfavorable growth of required  $ka \propto n^3$  in order to have a fixed fidelity is due to  $\sim n^6$  growth of intrinsic errors. It would therefore be advantageous to find a way to suppress errors due to non-resonant transitions (42).

### 6.3.8 Conclusions

We analyzed two possible errors in the implementation of an algorithm on a quantum computer. In particular we discuss the implementation of the QFT on the IQC. We consider: (i) intrinsic

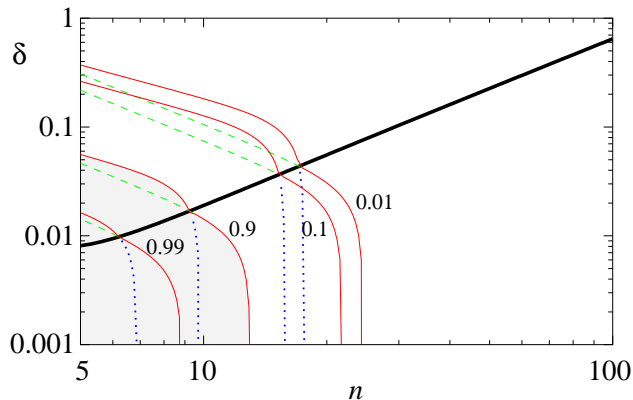


Figure 6.17: (Color online) Fidelity dependence on  $\delta$  and number of qubits  $n$  for  $ka = 10^5$ . IQFT is better above the thick line. For the explanation of the curves see the caption of Fig. 6.16.

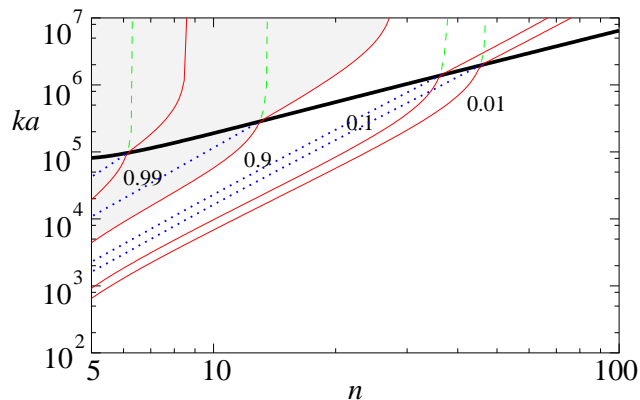


Figure 6.18: (Color online) Fidelity dependence on  $ka$  and  $n$  for  $\delta = 0.01$ . IQFT is better above the thick line. For the explanation of the curves see the caption of Fig. 6.16.

errors due to unwanted transitions caused by pulses, (ii) external errors due to the coupling with the external degrees of freedom. We carefully analyze their dependence on system parameters, particularly on the number of qubits. To diminish intrinsic errors we use the generalized  $2\pi k$  method by which we are able to suppress all near-resonant transitions, with only much smaller non-resonant transitions remaining. We then study these non-resonant errors in the QFT algorithm and by using correlation function formalism explain their growth with time as  $\sim T^2$ , in contrast to so far studied “simple” algorithms (having  $\mathcal{O}(n)$  gates), where the growth is linear in time. This very fast growth with  $n$  is a consequence of strong correlations between non-resonant errors at different pulses. In view of this it would certainly be desirable to find a way to suppress non-resonant errors, e.g. to uncorrelate or anti-correlate them.

Two interesting questions are immediately imposing themselves: Is this behavior general also for other models of quantum computers where the pulses (gates) are not perfect and whether this fast growth of errors is general for all algorithms having more than  $\mathcal{O}(n)$  gates? This is very important as the  $\sim T^2$  growth would mean that the problem of actually building a large quantum computer executing a complex algorithm is much harder than previously thought, since the correlations of errors at different time steps can significantly influence the stability.

We also consider perturbations due to the coupling with the external degrees of freedom modelled by a random GUE matrix. To suppress this kind of errors we show that it is advantageous to use an improved QFT algorithm, even in the presence of intrinsic errors. For the IQFT

these external errors grow only as  $\sim n^2$ , whereas they grow as  $\sim n^3$  for an ordinary QFT. The improvement of quantum Fourier transformation by using an IQFT algorithm is independent of the specific model used for the quantum computer as it depends only on the sequence of gates (algorithm) and on the external perturbation being a random GUE matrix. This result is particularly appealing as some argue that the external influences will be the main limiting factor in the construction of quantum computers and therefore using the IQFT can significantly improve performance in the limit of large number of qubits.

### 6.3.9 Apperndix A: QFT and IQFT implementation on the Ising Quantum Computer

To implement the protocol with high fidelity we use  $Q_{i\rho}^{ab}$  pulses derived in Ref. (32), which completely suppress all near-resonant errors. Phases of  $Q$ -pulses composing a gate must be chosen such that the gate works on an arbitrary state. The protocols implementing  $CN_{ij}$  (control not gate) and  $N_j$  (not gate) can be found in sections 7.1-7.3 of Ref. (32).

In order to complete the QFT and the IQFT we still need to implement the  $R^\dagger$ ,  $R$ ,  $A$ ,  $B$  and  $T$  gates. We can decompose  $R$ ,  $R^\dagger$  and  $T$  gates into simpler pieces:

$$R_{ij} = N_i CN_{ij} N_i Z_j, \quad (6.58)$$

$$R_{ij}^\dagger = N_i Z_j CN_{ij} N_i, \text{ and} \quad (6.59)$$

$$T = \prod_{i=1}^q \prod_{j=1}^{q-i} S_{q-j, q-j-1} \quad (6.60)$$

with  $S_{ij} = CN_{ij} CN_{ji} CN_{ij}$  the swap gate,  $Z = \text{diag}\{1, -1\}$  the  $\sigma_z$  gate and each term in the product in Eq. (6.60) is placed at the left of the sub-product (e.g.  $\prod_{i=0}^2 D_i = D_2 D_1 D_0$ ). Therefore, the only gates left to design are  $A$ ,  $B$  and  $Z$ .

The phases of  $Q$ -pulses can be expressed in terms of angles  $\theta_\rho$ ,  $\alpha_\rho$ ,  $\Theta_\rho$ ,  $\beta_\rho$  and  $\gamma_\rho$  (32) which are given by

$$\theta_\rho = \pi \sqrt{k_\rho^2 - \rho^2/4}, \quad (6.61)$$

$$\alpha_\rho = \frac{\pi}{2} \sqrt{k_\rho^2 + 3\rho^2/4}, \quad (6.62)$$

$$\tan \Theta_\rho = -\frac{\theta_\rho}{2\alpha_\rho} \tan \alpha_\rho, \quad (6.63)$$

$$\tan \beta_\rho = -\frac{\pi}{2\alpha_\rho} \tan \alpha_\rho \cos \Theta_\rho, \quad (6.64)$$

$$\gamma_\rho = \sqrt{(\pi k_\rho)^2 - (\pi + \beta_\rho)^2}. \quad (6.65)$$

We use notation of angles without subscripts denoting angles for  $\pi$  pulses i.e.  $\theta \equiv \theta_1$  and set  $k_{1/2} = 2k$ .

The Hadamard gate can now be expressed as

$$A_j = Q_j^{00}(\varphi_1) Q_j^{10}(\varphi_2) Q_j^{11}(\varphi_3) Q_{j\frac{1}{2}}^{00}(\varphi_4) Q_{j\frac{1}{2}}^{10}(\varphi_5) Q_{j\frac{1}{2}}^{11}(\pi/2), \quad (6.66)$$

for intermediate qubits and

$$A_j = Q_j^0(\varphi_6) Q_j^1(\varphi_7) Q_{j\frac{1}{2}}^0(\varphi_8) Q_{j\frac{1}{2}}^1(\pi/2), \quad (6.67)$$

for edge qubits, with

$$\begin{aligned}
\varphi_1 &= -2\left(\theta + \gamma_{\frac{1}{2}} + \theta_{\frac{1}{2}}\right), & \varphi_2 &= -\theta - 2\Theta, \\
\varphi_3 &= -2\left(\theta + \gamma - \gamma_{\frac{1}{2}} - \theta_{\frac{1}{2}}\right), & \varphi_4 &= \pi/2 - 2\gamma - 4\theta_{\frac{1}{2}}, \\
\varphi_5 &= \pi/2 - \theta_{\frac{1}{2}} - 2\Theta_{\frac{1}{2}}, & \varphi_6 &= -\theta - \theta_{\frac{1}{2}}, \\
\varphi_7 &= -\theta + \theta_{\frac{1}{2}}, & \varphi_8 &= \pi/2 - 2\theta_{\frac{1}{2}}.
\end{aligned} \tag{6.68}$$

For neighboring qubits ( $|i - j| = 1$ ) the  $B$  gate can be written as,

$$\begin{aligned}
B_{ij} &= Q_i^{11}(0)Q_i^{10}(0)Q_i^{00}(0)Q_j^{10}(0)Q_j^{10}(\varphi_1)Q_j^{00}(0) \\
&Q_j^{00}(\varphi_2)Q_i^{11}(\varphi_3)Q_i^{10}(\varphi_3)Q_i^{00}(\varphi_3)Q_j^{10}(0) \\
&Q_j^{10}(\varphi_4)Q_j^{11}(0)Q_j^{11}(\varphi_5),
\end{aligned} \tag{6.69}$$

for intermediate qubits and for edge qubits ( $i$  or  $j \in \{0, n - 1\}$ ) it is

$$\begin{aligned}
B_{ij} &= Q_i^1(0)Q_i^0(0)Q_j^{10}(0)Q_j^{10}(0)Q_j^{00}(0) \\
&Q_j^{00}(\varphi_6)Q_i^1(\varphi_7)Q_i^0(\varphi_8)Q_j^{10}(0) \\
&Q_j^{10}(\varphi_9)Q_j^{11}(0)Q_j^{11}(\varphi_{10}).
\end{aligned} \tag{6.70}$$

Angles for  $B$  gates are

$$\begin{aligned}
\varphi_1 &= -2\gamma - 3\theta + 2\Theta, & \varphi_2 &= \phi/2 - 2\gamma - 6\theta, \\
\varphi_3 &= \phi/4 - \pi/2, & \varphi_4 &= -\varphi_1, \\
\varphi_5 &= \phi/2 + 2\gamma + 6\theta, & \varphi_6 &= \phi/2 - 6\gamma - 12\theta + 4\Theta, \\
\varphi_7 &= \varphi_3 - \varphi_1, & \varphi_8 &= \varphi_3 + \varphi_1, \\
\varphi_9 &= -2\varphi_1, & \varphi_{10} &= \phi/2 - 2\gamma + 4\Theta,
\end{aligned} \tag{6.71}$$

and  $\phi = \pi/2$ . For distant qubits ( $|i - j| > 1$ ) it is necessary to use swap gates to bring  $i$ -th and  $j$ -th qubits to neighboring positions, then apply  $B$  protocol for neighbor qubits and finally take them back to their original positions using swap gates. The angle  $\phi$  in Eq. (6.71) is in this case  $\phi = \pi/2^{|j-i|}$ . Finally the  $Z$  gate is expressed as

$$Z_j = Q_j^{11}(0)Q_j^{10}(0)Q_j^{00}(0)Q_j^{11}(\pi/2)Q_j^{10}(\pi/2)Q_j^{00}(\pi/2) \tag{6.72}$$

for intermediate qubits and

$$Z_j = Q_j^1(0)Q_j^0(0)Q_j^1(\pi/2)Q_j^0(\pi/2) \tag{6.73}$$

for edge qubits. Counting the number of all pulses for QFT and IQFT one gets

$$T_{QFT} = 18n^3 - 16n^2 - 49n + 57 \tag{6.74}$$

$$T_{IQFT} = 54n^3 - 86n^2 - 105n + 191. \tag{6.75}$$



# Bibliography

- [1] R.P.Feynman, Found. Phys. 16, 507 (1986).
- [2] P.W.Shor, Proc. 35th Annual Symposium Foundations of Computer Science (ed. Goldwasser, S.) 124, (IEEE Computer Society, Los Alamitos, CA, 1994)
- [3] L.K.Grover, Phys. Rev. Letter, **79**, 325 (1997).
- [4] L. M. K. Vandersypen, M. Steffen, G. Breyta, C. S. Yannoni, M. Sherwood, and I. L. Chuang. Experimental realization of Shor's quantum factoring algorithm using nuclear magnetic resonance. Nature, 414 pp. 883, 2001.
- [5] Charles H. Bennett, Gilles Brassard, Claude Crpeau, Richard Jozsa, Asher Peres, and William K. Wootters, Phys. Rev. Lett. 70, 1895, (1993).
- [6] Jian-Wei Pan, Matthew Daniell, Sara Gasparoni, Gregor Weihs, and Anton Zeilinger Experimental Demonstration of Four-Photon Entanglement and High-Fidelity Teleportation Phys. Rev. Lett. 86, 4435 (2001)
- [7] G. P. Berman, G. D. Doolen, G. D. Holm and V. I. Tsifrinovich, Phys. Lett. A**193**, 444 (1994)
- [8] G. P. Berman, F.Borgonovi, G.Celardo, F.M.Izrailev and D.I.Kamenev "Dynamical fidelity of a solid-state quantum computer" Phys. Rev. E 66, 056206 (2002);
- [9] G.P.Berman, D.I.Kamenev, R.B.Kassman, C.Pineda and V.I.Tsifrinovich, "Method for implementation of universal quantum logi gates in a scalable Ising spin quantum computer, Int.J. of Quant. Inf. (1), 51 (2003)
- [10] G.P.Berman, D.I.Kamenev and V.I.Tsifrinovich, "Minimization of non-resonant effects in a scalable Ising spin quantum computer" quant-ph/0310049
- [11] G.L. Celardo, C.Pineda, M. Znidaric, quant-ph/0310163
- [12] T.Prosen and M.Znidaric, J. Phys. A: Math. Gen. (34), L681 (2001)
- [13] I.L. Chuang, R. Laflamme, P.W. Shor, and W.H. Zurek, Science, **270**, 1633 (1995).
- [14] V. Zelevinsky, B.A. Brown, N. Frazier, and M. Horoi, Phys. Rep., **276**, 85 (1996).
- [15] T. Guhr, A. Müller-Groeling, and H.A. Weidenmüller, Phys. Rep., **299**, 189 (1999).
- [16] V.K.B. Kota, Phys. Rep., **347**, 223 (2001).
- [17] B. Georgeot and D.L. Shepelyansky, Phys. Rev. E., **62**, 3504 (2000); ibid, 6366.

- [18] G.P. Berman, F. Borgonovi, F.M. Izrailev, and V.I. Tsifrinovich, Phys. Rev. E., **64** 056226 (2001); Phys. Rev. E., **65**, 015204 (2001).
- [19] A.Peres, Phys. Rev. A **30**, 1610 (1984); R.A. Jalabert and H.M. Pastawski, Phys. Rev. Lett. **86**, 2490 (2001); Ph. Jacquod, P.G. Silvestrov and C. W. J. Beenakker, Phys. Rev. E **64**, 055203 (2001); N.R. Cerruti and S.Tomsovic, Phys. Rev. Lett. **88**, 054103 (2002); T.Prosen, Phys. Rev. E **65**, 036208 (2002); F.M. Cucchietti, C.H.Lewenkopf, E.R.Mucciolo, H.M. Pastawski and R.O. Vallejos, Phys. Rev. E **65**, 046209 (2002) ; G.Benenti and G.Casati, quant-ph/0112132; T.Prosen and T.H.Seligman, nlin.CD/0201038; T.Prosen and M.Znidaric, J.Phys. **A 34**, L681 (2001).
- [20] G.P. Berman, G.D. Doolen, G.D. Holm, V.I. Tsifrinovich, Phys. Lett. A , **193**, (1994) 444.
- [21] G.P. Berman, G.D. Doolen, R. Mainieri, and V.I. Tsifrinovich, *Introduction to Quantum Computers*, World Scientific Publishing Company, 1998.
- [22] G.P. Berman, G.D. Doolen, G.V. López, and V.I. Tsifrinovich, Phys. Rev. A, **6106**, 2305 (2000).
- [23] G.P. Berman, G.D. Doolen, D.I. Kamenev, and V.I. Tsifrinovich, Phys. Rev. A, **6501**, 2321 (2002).
- [24] K.J. Bruland, W.M. Dougherty, J.L. Garbini, J.A. Sidles, S.H. Chao, Appl. Phys. Lett., **73**, 3159 (1998).
- [25] D. Suter and K. Lim, Phys. Rev. A, **65**, 052309 (2002).
- [26] G.P. Berman, D.K. Campbell, V.I. Tsifrinovich, Phys. Rev. B, **55**, 5929 (1997).
- [27] B.E. Kane, Nature, **393**, 133 (1998).
- [28] C. H. Bennett and D. P. DiVincenzo, Nature **404**, 247 (2000).
- [29] G. P. Berman, G. D. Doolen, G. D. Holm and V. I. Tsifrinovich, Phys. Lett. A**193**, 444 (1994). *The Foundation of Computer Science* (IEEE Computer Society Press, New York 1994), p. 124.
- [30] G. P. Berman, F. Borgonovi, G. Celardo, F. M. Izrailev and D. I. Kamenev, Phys. Rev. E **66**, 056206 (2002).
- [31] G. P. Berman, G. D. Doolen, G. V. Lopez and V. I. Tsifrinovich, Phys. Rev. A **61**, 042307 (2000).
- [32] G. P. Berman, D. I. Kamenev, R. B. Kassman, C. Pineda and V. I. Tsifrinovich, Int. J. Quant. Inf. **1**, 51 (2003).
- [33] T. Guhr, A. Müller-Groeling and H. A. Weidenmüller, Phys. Rep. **299**, 190 (1998).
- [34] T. Prosen and M. Žnidarič, J. Phys. A: Math. Gen. **34**, L681 (2001).
- [35] T. Prosen and M. Žnidarič, J. Phys. A: Math. Gen. **35**, 1455 (2002); T. Prosen, Phys. Rev. E **65**, 036208 (2002).
- [36] A. M. Steane, in *Decoherence and its implications in quantum computation and information transfer* (eds. Gonis and Turchi) (IOS Press, Amsterdam, 2001), p.284, also preprint quant-ph/0304016.

- [37] G. P. Berman, G. D. Doolen, G. V. Lopez and V. I. Tsifrinovich, *Phys. Rev. A* **61**, 062305 (2000).
- [38] D. G. Cory et al., *Fortschritte der Physik* **48**, 875 (2000).
- [39] T. Prosen, T. H. Seligman and M. Žnidarič, *Prog. Theo. Phys. Supp.* **150**, 200 (2003).
- [40] T. Prosen and M. Žnidarič, *New Journal of Physics* **5**, 109 (2003).
- [41] L.-A. Wu and D. A. Lidar, *Phys. Rev. Lett.* **91**, 097904 (2003).
- [42] G. P. Berman, D. I. Kamenev and V. I. Tsifrinovich, preprint [quant-ph/0310049](https://arxiv.org/abs/quant-ph/0310049).